THE UNIVERSITY OF READING

Department of Meteorology

Behaviour of the monsoon-ENSO system in current and future climates of a general circulation model

Andrew George Turner

A thesis submitted for the degree of Doctor of Philosophy

December 2005

Declaration

I confirm that this is my own work and the use of all material from other sources has been properly and fully acknowledged.

Andrew Turner

Abstract

Seasonal prediction of the Asian Summer monsoon is a key goal of weather and climate forecasters, the phenomenon being of great importance to agrarian societies. Before general circulation models (GCMs) can be used to make predictions of the monsoon response to climate change, systematic errors in current simulations must be addressed.

This thesis examines the impact of sea-surface temperature (SST) errors in the Indo-Pacific regions on the coupled simulation of the Asian summer monsoon in HadCM3. Limited-area ocean surface heat flux adjustments are used in the tropical band to reduce these biases. The result is a better teleconnection between the monsoon and ENSO, especially in lag-lead relationships which are stronger and better timed. The improvement is related to better evolution of El Niño during its developing phase. Some form of flux correction may thus be beneficial, for seasonal prediction at least, where systematic model errors compromise monsoon simulation.

Climate change presents new challenges for monsoon prediction, and is also likely to alter ENSO, and subsequently its teleconnection to the monsoon. Indeed ENSO may be given different priority in future monsoon prediction, especially relevant given recent weakening of the observed relationship. The same flux adjustments are used in a doubled carbon dioxide scenario, and compared to an uncorrected integration. Overall monsoon strengthening is observed irrespective of flux adjustment, although changes to the mean Indo-Pacific climate and its interannual variation are further amplified when biases are removed.

The tropospheric biennial oscillation (TBO) mechanism is found to be a useful descriptor of a biennial regime found in the monsoon-ENSO system of a flux-corrected future climate. Both greenhouse gas increases and flux adjustment are found to contribute to the biennial tendency in the more energetic system, and implications for monsoon predictability are assessed.

Acknowledgements

I would first like to thank my supervisors, Julia Slingo and Pete Inness, for their constructive criticism and timely encouragement during my studies. I have also been involved in useful discussions with the CGAM Tropical group who have offered good ideas for further study.

For computing support I would like to thank Andy Heaps both for helpful advice and always keeping me supplied with disk space! Lois Steenman-Clark has offered clear instruction on how to use the high performance resources at CSAR and HPCx.

I would also like to thank Franco Molteni and Fred Kucharski at ICTP, Trieste, Italy for support during short periods of study there. Credit is also due to Anthony Illingworth and David Grimes who, in Thesis Committee meetings, have sought rigorous explanations of my work.

Contents

List of Figures

List of Tables

Chapter 1

Introduction

The movement of the sun relative to the Earth gives rise to seasonal shifts in wind regimes or *monsoons*, often associated with corresponding shifts in precipitation extremes as the Inter Tropical Convergence Zone (ITCZ) follows the solar maximum. One such monsoon is the Asian Summer Monsoon, where south-westerly winds prevail over the Indian region during the boreal summer, together with a marked increase in precipitation.

1.1 Motivation

The Asian summer monsoon affects the lives of more than 2 billion people in India, China, and the rest of Southeast Asia through the agrarian basis of their society. The production of food crops ranges from large scale agribusiness for export to subsistence farming for individual families in more remote regions. It is not only agriculture, however, which relies on the monsoon. The burgeoning economies of Southeast Asia increasingly need water for wider economic development, through the expansion of industry which itself requires increasing electrical power, often provided through hydroelectric generation. Hence the correct forecasting of the onset, duration, and intensity of the monsoon are of vital importance to the farmers and industrial planners of the region. Seasonal forecasting in advance of the monsoon summer also allows contingency plans to be put in place should the need arise, for example to stockpile water and food supplies in the event of a summer drought, or vaccines to counter the effect of water-borne disease should flooding occur.

Traditionally, organisations such as the Indian Meteorological Department (IMD) based in Pune have used statistical models to form their seasonal prediction (Krishna Kumar *et al.*, 1995). This relies on the input of recent weather means and tendencies, including wind patterns, snow cover, land surface temperatures, sea-surface temperatures (SST) and sea level pressures (SLP). Almost a third of the 16 predictors formerly used in the power regression model of the IMD involve behaviour over the Pacific Ocean (Krishna Kumar *et al.*, 1995), describing various aspects of the El Niño-Southern Oscillation (ENSO). The importance of this Pacific influence can be seen in Fig. 1.1, an instantaneous spatial correlation between summer All-India Rainfall (Parthasarathy *et al.*, 1994) and SST (HadISST, Rayner *et al.*, 2003). This shows that over the last century, temperatures in the central to east equatorial Pacific are strongly negatively correlated with seasonal monsoon rainfall over India, helping support the choice of predictors used. Further, strong positive correlations exist in a horseshoe pattern towards the west Pacific. Low negative correlations with Indian monsoon rainfall are found in the Indian Ocean. Indeed Charney and Shukla (1981) found that the correct prediction of lower boundary forcing, varying at low frequencies, was vital for correct monsoon simulation.

Strong interannual variations of the All-India Rainfall are shown in Fig. 1.2, and these variations can cause significant problems for the monsoon-affected societies of Southeast Asia for the reasons outlined at the beginning of this section. Also indicated is the strong connection between seasonal behaviour and events in the equatorial Pacific. Most (but not all) seasons with excessive rainfall occur during La Niña years. Similarly, the majority of droughts occur during El Niño years. Importantly some excess or drought years do not fit this relationship, and sometimes it is even reversed, further complicating seasonal prediction.

Seasonal forecasts based on empirical data are not always successful. The summer of 2002 saw an unexpected drought, as shown in Fig. 1.3. The figure indicates the climatological mean daily rainfall during the Indian summer monsoon (June to Septem-

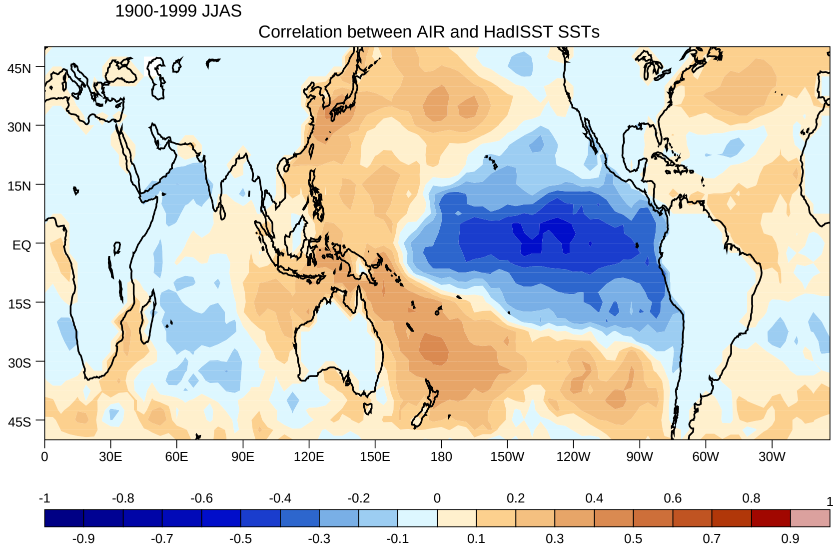

Figure 1.1: Instantaneous summer (JJAS) correlation between All-India Rainfall gauge dataset and HadISST SSTs over the period 1900-1999. Correlations outside ± 0.2 are significant above the 95% level using a student t-test.

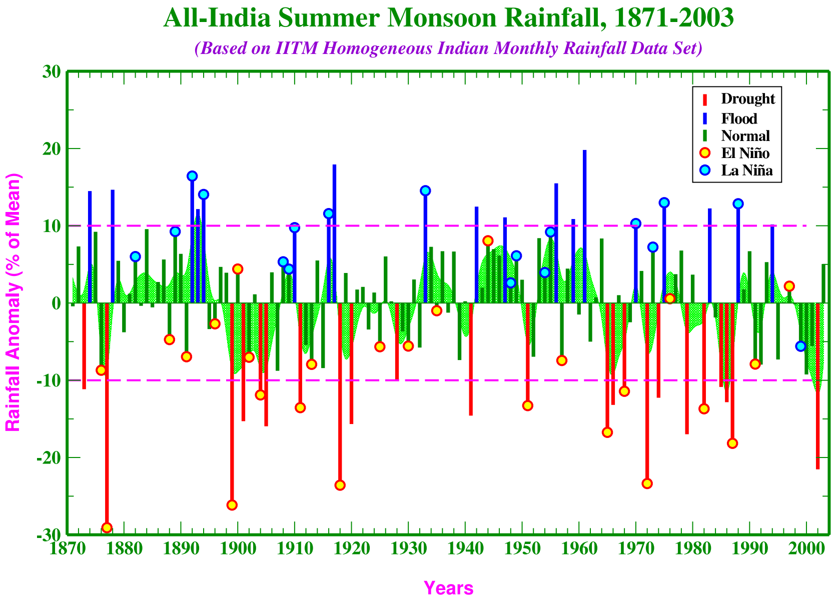

© Rupa Kumar Kolli, IITM, Pune, India (April 23, 2004)

Figure 1.2: Interannual variability in the observed record of the Indian summer monsoon, supplied by the Indian Institute of Tropical Meteorology (`http://www.tropmet.res.in/~kolli/MOL`). Associations with El Niño or La Niña conditions in the east Pacific are also indicated.

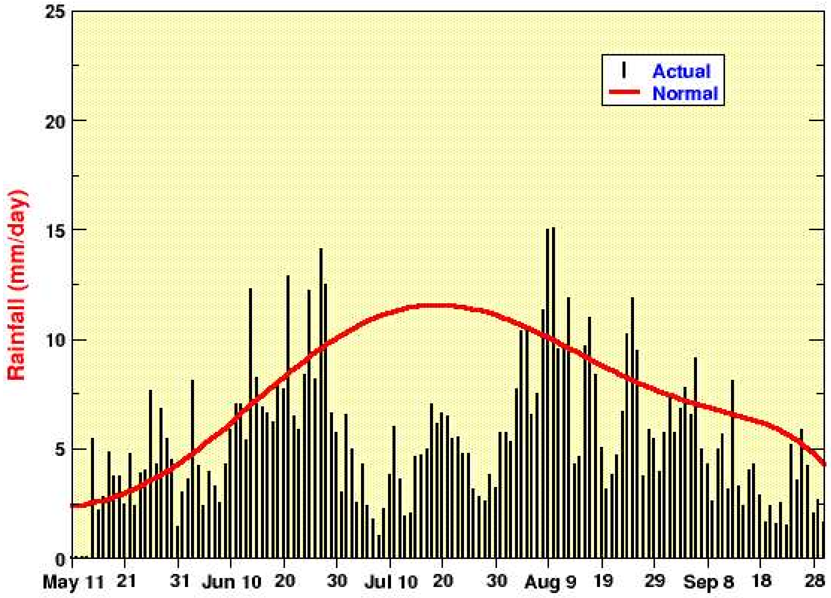

Figure 1.3: Daily rainfall totals for the 2002 Indian summer monsoon season, from the All-India Rainfall gauge network. The climatological mean daily totals are also indicated. Figure obtained from `http://www.tropmet.res.in/∼kolli/MOL`

ber), along with daily totals during the 2002 season. Given that a normal monsoon was forecast, the massive deficit in July rainfall (less than 50% of the mean climatological total) caused tremendous problems for the supply of food and economic growth, that contingency plans were not in place to deal with. One way to improve these forecasts is to check the validity of the statistical predictors used, which may vary over time, and better define them accordingly. The IMD forecast was recently verified in this way (Rajeevan *et al.*, 2004). Increasingly however, coupled general circulation models (GCMs) are being used for seasonal prediction purposes. These dynamical models are not without their faults, lacking the resolution needed to adequately resolve ocean wave dynamics, important for the correct representation of El Niño development. The model physics are incomplete, many processes and feedbacks on the coupled system being left out. Systematic biases present in GCMs may also impinge on their ability to correctly simulate both the mean monsoon and its variations. In a study of several atmosphere-only GCMs, Sperber and Palmer (1996) found that the models with the best realisation of the teleconnection between Indian monsoon rainfall and ENSO in the Pacific featured the best simulation of the mean climate. This link between model climatology and interannual variability serves as an important motivation for this thesis. In coupled ocean-atmosphere GCMs, the sea-surface is not prescribed but evolves naturally, instead taking into consideration fluxes of heat and moisture between its atmospheric and oceanic components. These models also feature systematic biases in their mean climate, particularly in the SST field which isn't held by the same constraints as in AGCMs.

Sperber *et al.* (2000) found that model improvements which both reduced the systematic errors in the mean simulation, whilst correcting their response to the low-frequency boundary forcing, may improve seasonal prediction. A study using the Met Office Unified Model (HadCM3, Gordon *et al.*, 2000; Pope *et al.*, 2000) has shown that a more realistic representation of the mean climate in the tropical oceans can improve the intraseasonal behaviour in those regions (Inness *et al.*, 2003). This thesis will assess the impact of such errors on the mean monsoon climate and its variability.

Dynamical modellers must also concern themselves with future changes to the global climate, which will likely impact on the monsoon system and its external predictors. We have noted earlier in this section that statistical relations are varying in the current climate. The simulation of projected changes to the climate is uncertain and challenging, in addition to the uncertainty introduced by transient relationships between the monsoon and its outside influences. This forms the basis of much current study, and is another key motivator for this thesis.

The Unified Model (HadCM3), a fully coupled atmosphere-ocean model, will be used throughout this thesis.

1.2 Aims of the thesis

There are several broad aims to this thesis, each of which yields several more detailed questions. The first is a study of systematic biases present in coupled model simulations.

1 What is the effect of systematic errors in a coupled model on representation of

the monsoon system and its predictability?

- What effect do systematic errors have on the mean monsoon climate of a GCM?
- How is interannual variability of the monsoon season influenced by these errors?
- Is the predictability of the monsoon unduly affected by errors in the mean state and consequent misrepresentation of the variability? Can it therefore be improved upon?

The second main focus of the thesis will be to consider climate change and its possible effect on the monsoon system.

2 What is the effect of climate change on the monsoon system?

- What will be the effect of climate change on the mean monsoon? Will there be more or less precipitation on average?
- Does interannual variability change? Will there be greater extremes of flood and drought, and will they be more frequent?
- Will behaviour in the Pacific Ocean still exert the same influence on the monsoon system?

Clearly any future climate simulation using a coupled GCM will feature biases in the mean climate.

3 Can we make an assessment of the impact of systematic errors on future monsoon climate?

- What effect do assumed systematic biases have on the prediction of future climate?
- Are the errors in monsoon variability and prediction caused by these biases of similar magnitude to the climate change response?

1.3 Thesis outline

An extension of the concepts discussed in this chapter, and other scientific background to this thesis are presented in chapter 2.

An assessment of monsoon simulation and that of the wider tropical climate in the GCM against observational or reanalysis datasets is made in chapter 3. This continues with an attempt to correct some of the systematic errors in the tropical Indo-Pacific region, and chapter 3 further considers the impact of these errors on monsoon predictability. Chapter 3 has previously been published (Turner *et al.*, 2005), and minor adjustments have been made before its inclusion here.

The response of the monsoon-ENSO system to a climate change scenario is considered in chapter 4, both in terms of changes to the mean climate and monsoon extremes. The influence of basic state errors on future climate prediction is also considered in this chapter.

Next, in chapter 5, some assessment is made of interdecadal changes to the monsoon-ENSO system within GCM integrations of the future climate, and their important impact on monsoon predictability.

Conclusions to the thesis and suggestions for future experiments are given in chapter 6.

Chapter 2

Scientific background

This chapter will cover some of the scientific background necessary to understand the experiments performed during the course of this thesis. The annual cycle and monsoon development will be covered in §2.1, whilst interannual variability of the Asian summer monsoon will be described in §2.2. The links between interannual variations in the Asian monsoon and ENSO or Indian Ocean SSTs will be detailed in §2.3 and §2.4 respectively. Biennial variability of the monsoon-ENSO system will be covered separately in §2.5, and decadal timescale variations and climate change will be discussed in §2.6.

2.1 The annual cycle

The Asian Summer Monsoon forms part of a wider annual cycle occurring in the entire tropical band, and will be described after a brief introduction to the seasonal variation of the wider region.

2.1.1 The tropics

The annual cycle in the tropics is driven by the motion of the sun and associated changes in surface and atmospheric heating caused by the degree of solar insolation. Maximum heating moves from the northern hemisphere in boreal summer to the southern hemi-

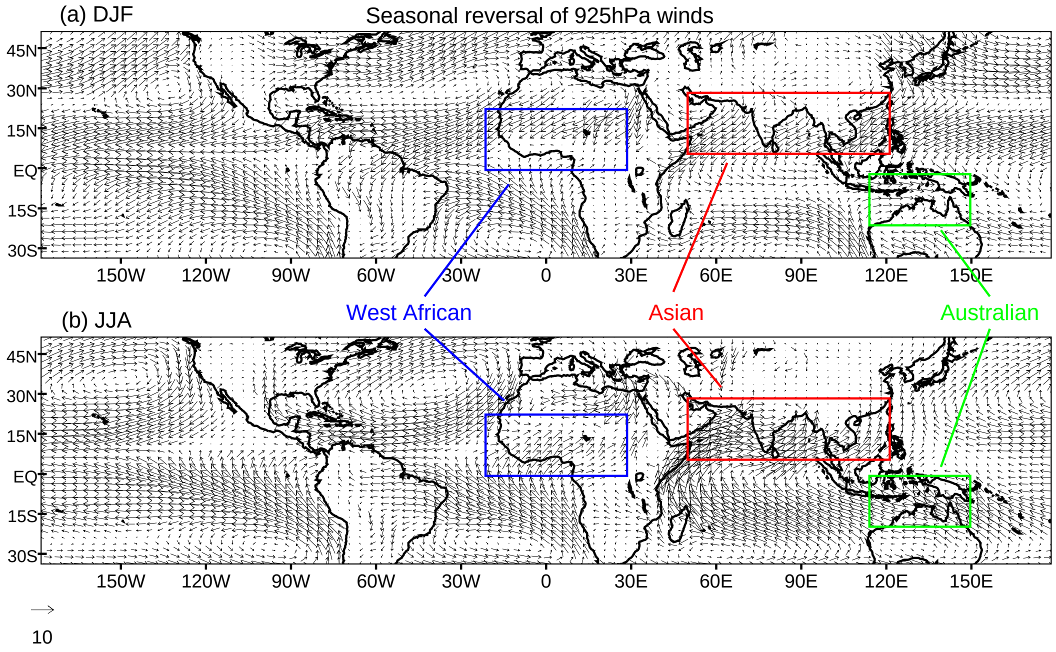

Figure 2.1: Seasonal reversal of low-level ($925\mathrm{hPa}$) winds, shown for the boreal winter (DJF) and summer (JJA) seasons in the ERA-40 reanalysis dataset (1958–1997). Regions affected by the Asian, Australian, and West African monsoons are illustrated. Unit wind vector is $10\mathrm{ms}^{-1}$.

sphere in winter. The large heat capacity of water means that normally, SST maxima lag the solar cycle by around two months, and this differential heating over land and ocean leads to temperature gradients and associated flow patterns throughout the tropics. Regular seasonal changes in the prevailing wind speed and direction are known as monsoons, which in West Africa, Southeast Asia and Australia, are accompanied by changes in the rainfall regime, from very dry to very wet periods. These wind regime changes and associated precipitation movements are shown for the three main monsoon regions in Figs. 2.1 and 2.2 respectively. To a lesser extent, seasonal precipitation changes over Central America are also associated with wind regime changes.

In their review of the whole monsoon system, Webster *et al.* (1998) studied the upper tropospheric flow around the tropics and found it to reveal thermal contrasts between the oceans and continents. In summer, a warm ridge is located over North America whilst deep temperature troughs span from the American west coast out over the central Pacific and similarly over the Atlantic. Over Asia however, summer temperature increases are greatest over the Tibetan Plateau, where a planetary-scale warm

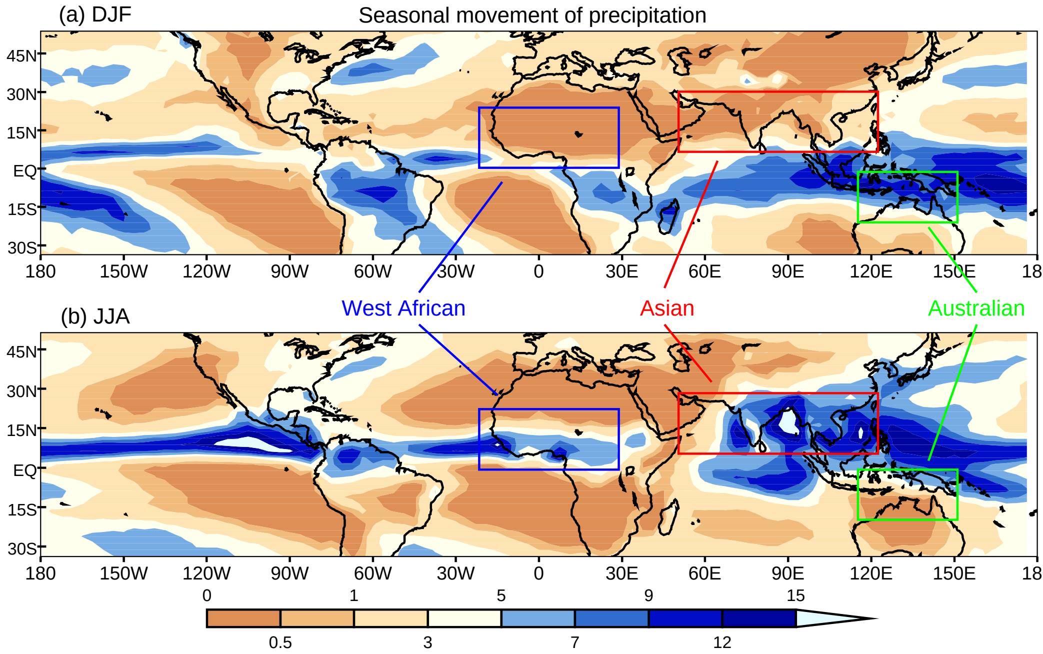

Figure 2.2: Seasonal motion of maximum precipitation, shown for the boreal winter (DJF) and summer (JJA) seasons in the CMAP dataset (1979–1997). Regions affected by the Asian, Australian, and West African monsoons are illustrated. Units are $\mathrm{mm.day}^{-1}$.

airmass is situated. Strong temperature gradients exist both meridionally and zonally around this region, as seen in Fig. 2.3 using ECMWF[1] ERA-40 data (Uppala *et al.*, 2005). At $30°\mathrm{N}$ over the plateau region, 200–$500\mathrm{hPa}$ layer temperature anomalies reverse their sign from negative to positive in April, reaching $9°\mathrm{C}$. In winter, warm ridges lie over South America and Australia, although no temperature gradients as significant as those in the northern hemisphere are found. Consequently upper-level temperature gradients in the southern hemisphere never reverse.

Webster *et al.* (1998) identified the major convective regions in the tropics, consisting of South Asia and equatorial North Africa during the summer, and a band from the Indian Ocean to northern Australia in winter, as seen in Fig. 2.2 using CMAP[2] data. As Fig. 2.2 shows, Asian convection is stronger and more poleward than its southern hemisphere (Australian) counterpart, the reasons for which will be explained later.

Three principle circulations of the monsoon systems are summarized by Webster

---

[1] European Centre for Medium Range Weather Forecasts

[2] Climate Prediction Center Merged Analysis of Precipitation

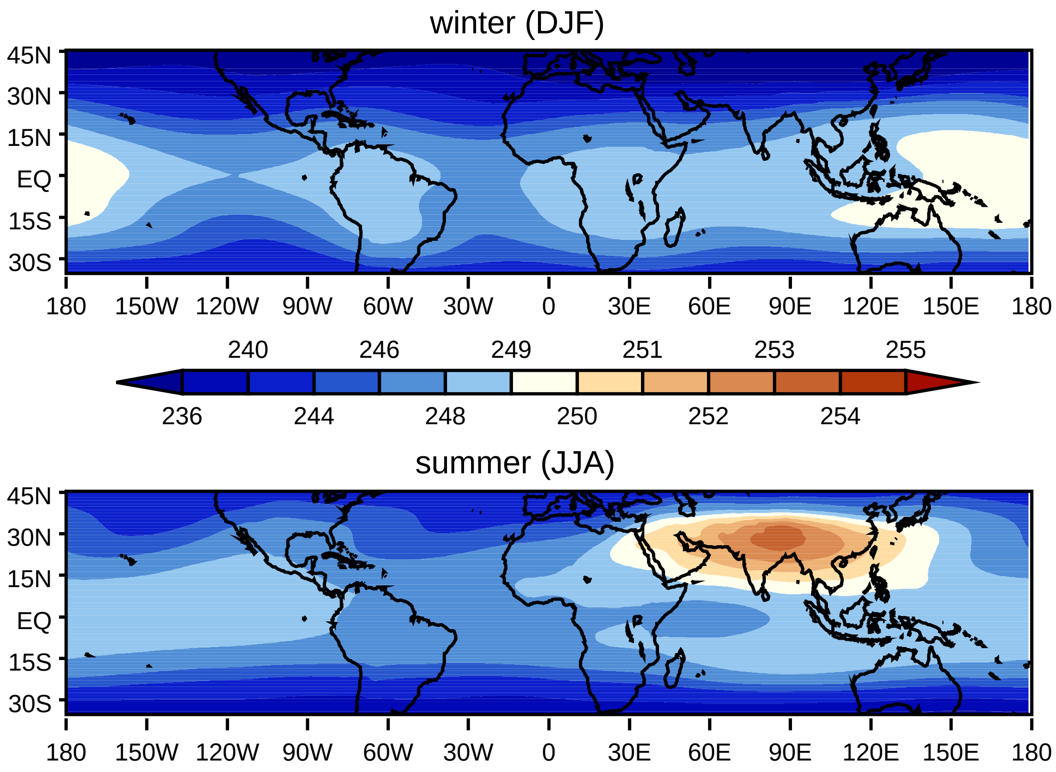

Figure 2.3: Summer and winter mid-troposphere (200–500hPa) layer temperatures in the ERA-40 re-analysis dataset. Units are K.

et al. (1998) and reproduced in Fig. 2.4.

- The *lateral* circulation is a cross equatorial component, most emphasised during the Asian summer monsoon.
- The strong *transverse* flow is driven by longitudinal heating gradients contrasting the arid regions of North Africa and the Middle East with the intense latent heating over South Asia. The arid regions also undergo extensive radiative cooling.
- The *Walker* circulation is also transverse in character, extending out across the Pacific. In terms of mass flux, this circulation is half as large as either of the monsoon components. The sea-level pressure (SLP) over the Indian and Pacific Oceans sways as part of the Walker circulation in its annual cycle. At the spring equinox the zonal equatorial pressure gradient weakens or even reverses, an important point which will be returned to later.

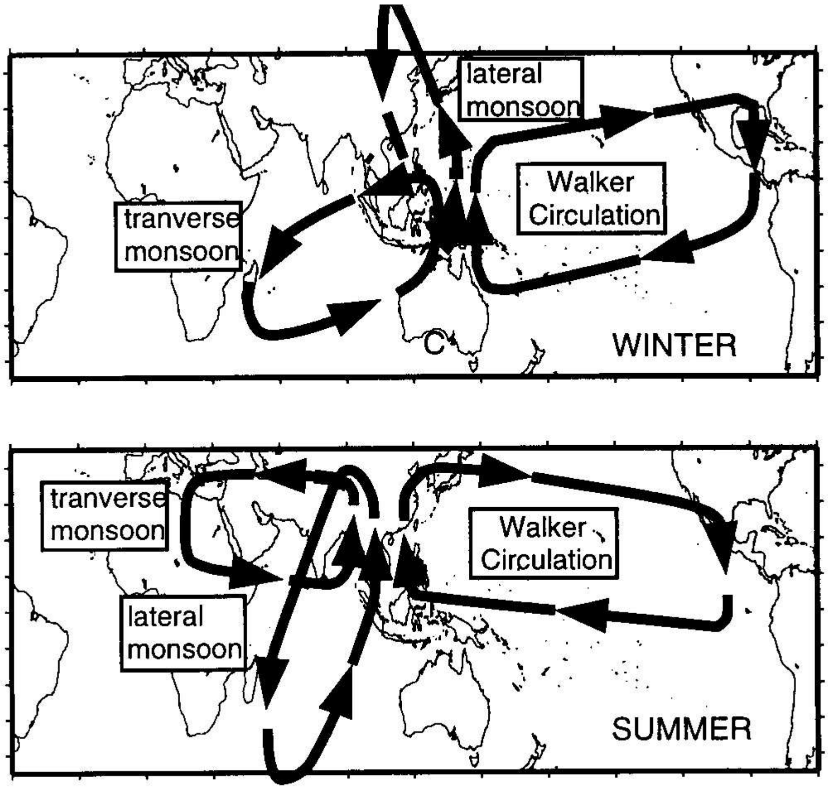

Figure 2.4: The component circulations of the boreal summer and winter seasons, taken from Webster *et al.* (1998).

The ascending regions of these three circulations are coincident in summer over Southeast Asia and the Maritime Continent. In winter the same major circulations are oriented such that ascent regions coincide over the southern Indian Ocean, northern Australia, and the west Pacific. Hence this centre of action of low-level convergence helps define the Asian and Australian monsoon regions.

The annual cycle in the tropics is summarized by Webster and Yang (1992) in terms of satellite-derived outgoing long-wave radiation data (OLR). Their 1974–1987 means were used as proxies for convection; minimum values indicating broad-scale precipitation and tropospheric heating. The majority of atmospheric heating lies across the equator and South Asia. Further, splitting the OLR fields into symmetric and asymmetric components, Webster and Yang (1992) sought to identify the near-equatorial and monsoonal heating parts. These are linked to the zonal and meridional circulations respectively, both of which have strong annual cycles. The asymmetric monsoonal component features rapid growth in spring and early summer, maximising at around $90°\mathrm{E}$ (around the Bay of Bengal), and maintaining a strong gradient towards the equator. This dominates over the equatorial zonal gradient, which weakens as summer arrives. The intense meridional gradient is maintained past the autumnal equinox before gradually declining, in contrast to the rapid change in spring. This therefore imposes an asymmetric signal on the annual cycle. By December, the meridional heating gradient has decreased by 80%, bringing the major heating regions much closer to the equator where they dominate the winter OLR fields of the Indo-Pacific region. The Walker circulations are maximised at this time too, and thus this symmetric circulation is six months out of phase with the monsoon. Reduced convergence and convection occurs over the Maritime Continent in winter, illustrated by the shifted circulations in Fig. 2.4.

The differences between the Asian and Australian monsoon systems and their component circulations can be attributed to orographic features. The Indian Ocean is bounded to the west and north by the East African Highlands and the Himalaya/Tibetan Plateau respectively, which both play an important role in development during the Asian summer. The East African highlands were found to help concentrate the south-westerly monsoon flow (Rodwell and Hoskins, 1995), seen in the western Indian Ocean of Fig. 2.1b. Further north, the air above the Tibetan Plateau is always warmer than adjacent columns at the same latitude and level, as found by Webster *et al.* (1998). The authors also noted that in winter and early spring, flow descends strongly to the south of the Tibetan Plateau, while later in spring there is weak upward motion. The ascent gets stronger, extending across 5–$45°\mathrm{N}$. Until June, regions east of the plateau are dominated by strong subsidence, but afterwards the ascent becomes more general, expanding east and west of the mountains. The African monsoon is relatively weak in comparison, with two distinct rainy seasons due to its proximity to the equator, and a lack of elevated heating as large or extensive as the Himalaya. Australia also lacks substantial elevated regions, and is largely flat.

2.1.2 The Asian summer monsoon

The Asian summer monsoon (ASM) forms the most significant part of the annual cycle in the tropics and, together with its global teleconnections which aid prediction, forms the focus of this thesis. The development of the ASM is thus explained in more detail here. Ju and Slingo (1995) characterized the ASM in terms of its onset, established and retreat phases, and further, Webster *et al.* (1998) recognised the monsoon onset as being of utmost importance, its correct prediction, critical for the planting and ploughing of the various crops grown in the agrarian societies of Southeast Asia. Li and Yanai (1996) found that the onset of the Asian Summer monsoon occurs with the reversal of the meridional temperature gradient in the upper troposphere south of the Tibetan Plateau, near to 90–$100°\mathrm{E}$, whilst Rodwell and Hoskins (1995) found that the very existence of the cross-equatorial flow which becomes the monsoon jet is dependent on the contrast in surface friction across the land/sea boundaries of the Indian Ocean.

The temperature reversal is a result of solar insolation causing sensible heating over the Tibetan Plateau. No such large increases occur over the Indian Ocean, over which latent heating occurs, and rising temperatures are restricted by adiabatic cooling, note Li and Yanai (1996). In spring, the Tibetan Plateau heat source is separate from the more intense heat source associated with the rain belt in the equatorial Indian Ocean. Variability of the ASM can be clearly associated with variations in the thermal contrast between Eurasia and the Indian Ocean, emphasising the importance of land-atmosphere interaction. The heating gradient idea implies that a delay to the normal land-warming would cause a delayed and weakened monsoon circulation.

At low levels, Ju and Slingo (1995) noted an anticyclonic circulation appearing over the Arabian Sea in April, with a north-westerly flow into India. In May the cross-equatorial Somali Jet develops in the equatorial western Indian Ocean, leading to the establishment of a south-westerly flow associated with the monsoon over Southeast Asia, and a trough to the east of the Indian subcontinent. Using NCEP/NCAR[3] reanalyses, Sperber *et al.* (2000) confirmed that development of the Somali Jet was in response to

---

[3] National Centers for Environmental Prediction/National Center for Atmospheric Research.

the reversal of the land-sea temperature gradient. The dramatic nature of this shift in winds was noted by Webster *et al.* (1998), as the rapid acceleration of southerly winds in the western Indian Ocean in early June, transferring from weak northerlies to strong southerlies ($> 9\mathrm{ms}^{-1}$) within about a week. The northern Indian Ocean features an equally rapid zonal acceleration, so that by early June strong westerlies are established across 45–$100°\mathrm{E}$.

Ju and Slingo (1995) also picked out the evolution of upper tropospheric characteristics in their work. They noted two transition phases of the ASM in early summer, characterized by abrupt movements of the south Asian anticyclone, poleward migration of the subtropical westerly jet and easterlies over the northern and equatorial Indian Ocean. In mid-May the anticyclone moves north from 10–$20°\mathrm{N}$, preparing for monsoon establishment. The anticyclone then remains over southern China until mid-June, when it moves rapidly over western parts of the Tibetan Plateau, accompanied by the monsoon onset over the Indian peninsula, eastern China (termed the Mai-yu winds), and Japan (the Bai-u winds).

Webster and Yang (1992) measured the daily upper and lower tropospheric wind kinetic energies over $5 - 15°\mathrm{N}$ and $40 - 110°\mathrm{E}$. In spring, they found the monsoon circulation to undergo explosive growth, with equatorial zonal pressure gradients across the Pacific declining sharply. Ju and Slingo (1995) looked only at $850\mathrm{hPa}$ data and found the kinetic energy to increase at the beginning of May, reaching a maximum by the end of June.

The meridional temperature gradient exceeds $6°\mathrm{C}$ in July, and strong low-level flow into India is maintained through July and August. Once the monsoon has developed, Sperber *et al.* (2000) noted, convective latent heating helps maintain and evolve it, the warm Indian Ocean and Arabian Sea providing moisture. Ju and Slingo (1995) found the south-westerly monsoon flow into China waning during August and September, followed by the rapid retreat of the monsoon from Asia. A gradual deceleration and equatorward movement of the westerly flow into India occurs in September. By October the steadily decreasing westerlies become easterly, but a number of westerly surges can continue into November. The meridional temperature gradient goes neg-

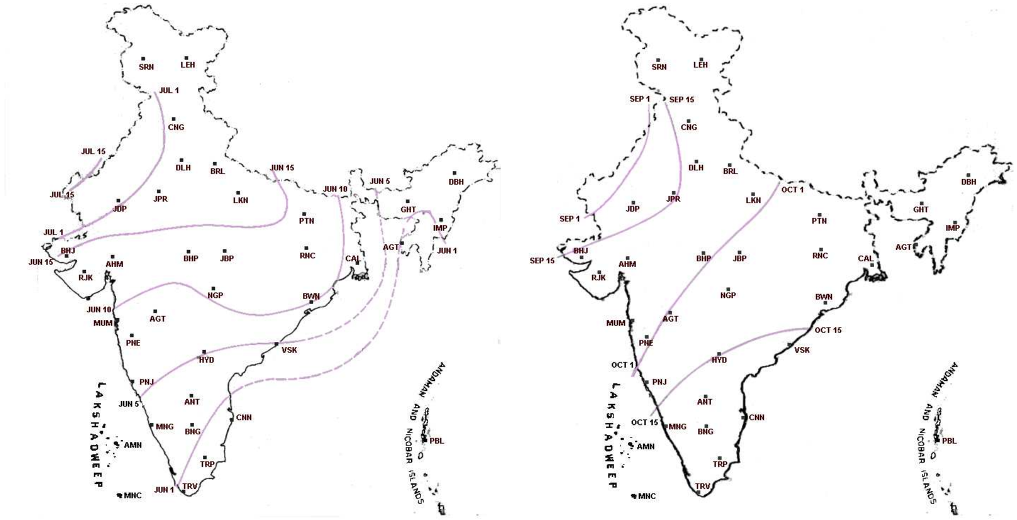

(a) Onset dates (b) Withdrawal dates

Figure 2.5: Climatological monsoon (a) onset and (b) withdrawal dates, as defined by the Indian Meteorological Department (IMD). Taken from `http://www.imd.gov.in`

ative between September and October, and Ju and Slingo (1995) noticed the upper-tropospheric anticyclone moving south-east, the equatorial easterlies weakening and the subtropical westerly jet moving equatorward as characteristics of the monsoon retreat. Both Webster and Yang (1992) and Ju and Slingo (1995) highlight the gradual decrease in monsoon kinetic energy, in contrast with the more explosive onset, reaching its original level by the end of September.

The monsoon onset has many definitions, ranging from a gradual increase in humidity and the commencement of rains, to the build up of a monsoon vortex in the northern Indian Ocean, as suggested by Webster *et al.* (1998). However, onset of the monsoon rainfall and it subsequent duration is of most interest to the regional population, particularly to farmers who need to sow their crops just before the start of the rains. This onset occurs over Burma or Thailand in mid May, before moving over the Bay of Bengal later in the month and reaching India around the first of June.

Krishnamurthy and Shukla (2000) reviewed a detailed study of 1901–1984 rainfall data, and found the climatological onset date to be June 2 over Kerala in south-west India. In the mean evolution, precipitation gradually advances over India, intensifying by June 15 and extending over a larger area including the central regions. By July 1 almost all India receives rainfall, which is now heavy over the Western Ghats and the eastern high ground. Withdrawal becomes apparent by about September 20 with much of India getting lighter rainfall, and is almost complete by September 28. Climatological onset and withdrawal dates as defined by the IMD are shown in Fig. 2.5a,b. During this period there are large scale intraseasonal variations of high amplitude, and whilst these *active* and *break* cycles are of fundamental importance to those dependent on water (see, $e.g.$, the large break during July 2002 shown in Fig. 1.3) their representation in current GCMs is limited and so they are not discussed here.

The annual cycle of the ASM, noted Webster *et al.* (1998), has the largest amplitude of any subtropical or tropical climate feature, and also large interannual, biennial and interdecadal variations to the pattern. The next sections will consider monsoon variability on interannual to decadal timescales and the implications for seasonal prediction.

2.2 Interannual variability

As explained in chapter 1, the interannual variability of the Asian summer monsoon and its successful prediction are vital for the economy and public health of countries in South Asia such as India. Here some interannual characteristics are studied along with measures to determine monsoon strength at these timescales. One of the main remote influences on interannual variability, the El Niño-Southern Oscillation (ENSO) is described later in this section.

Webster *et al.* (1998) noted that the ASM, and coupled ocean-atmosphere system of the Pacific Ocean, feature interannual changes on a 3–7 year timescale, as well as oscillating between strong and weak monsoon summers. Much study has been done on this apparent biennial nature of the Asian-Australian monsoon and this is reviewed separately in §2.5. Sperber *et al.* (2000) found that interannual variability of the ASM was dominated by a several modes of variability, some of which were systematically perturbed during anomalous monsoons. They rule out changes in weather regimes as the cause for monsoon interannual variability, it instead being pre-disposed to certain states by low frequency boundary forcing, as suggested by Charney and Shukla (1981).

The two popular routes of studying monsoon interannual variability and defining the extreme monsoon year are the large-scale circulation statistics, and precipitation, often on a more localized basis.

The interannual variation in precipitation is clearly of most importance to the local population in monsoon affected regions, impacting on food supply, propagation of disease, hydroelectric generation and overall economic growth. Figure 1.2 showed interannual variation of the All-India Rainfall dataset (Parthasarathy *et al.*, 1994). This long-period dataset based on information from 306 raingauges, was analysed by Monsoon On-Line (2005), yielding a seasonal average (June to September) rainfall of $853\mathrm{mm}$, representing approximately 80% of India's annual rainfall. With a standard deviation of $85\mathrm{mm}$ (10%), variation can clearly impact on monsoon regions. Krishnamurthy and Shukla (2000) recognised that the All-India Rainfall timeseries has become a proxy for the interannual variation of the ASM as a whole, precipitation varying on a region larger than the Indian subcontinent. Monsoon-wide precipitation data would be a better indicator of the circumstances in a given season, yet the data is rather inhomogeneous over the whole South Asia region. A study of interannual variations in monsoon onset was carried out by Ju and Slingo (1995), who found peak variation of 22 days, with a standard deviation of 9 days. In their study, Krishnamurthy and Shukla (2000) found a similar standard deviation (8 days). Webster *et al.* (1998) noted that drought years of the Indian monsoon are characterized by persistent negative monthly rainfall anomalies during the entire season (although 2002 in Fig. 1.3, seems contrary to this), whilst in heavy rainfall years there is slightly greater variability from one month to the next. Major Indian drought anomalies were also found to extend over most of the subcontinent. Sperber *et al.* (2000) used the All-India Rainfall (AIR) to show that variations in seasonal rainfall were associated with characteristic winds. Enhanced rain over India was found to be consistent with cyclonic anomalies over the subcontinent, whereas below normal rainfall to the south and west of the Indian region coexists with anticyclonic anomalies. In the Himalayan foothills, reduced rainfall is again noted along with anticyclonic circulation. In composites of strong minus weak rainfall, Sperber *et al.*

(2000) noticed a north-south dipole of rainfall anomalies, with enhanced rain over the continental ASM regions accompanied by reduced rain near $5°\mathrm{N}$, all associated with greater monsoon flow. There was also an east-west dipole with below normal rainfall in the west Pacific, and a strong signal over Africa.

As an alternative to precipitation, many studies use indices based on wind strength to illustrate year-to-year variations. This reflects the poor availability of homogeneous rainfall data over the whole shadow of the Asian summer monsoon, and given the coarse horizontal resolution of GCMs and reanalysis datasets, it is wise to consider dynamics over a broad region. Webster and Yang (1992) devised a dynamical monsoon index (DMI) based on the anomalous zonal windshear over South Asia, to measure the broad-scale heating in the atmospheric column. The region used is 5–$20°\mathrm{N}$, 40–$110°\mathrm{E}$, and the index is calculated as in Eq. (2.1).

$$\mathrm{DMI} = \overbrace{(U_{850} - \bar{U}_{850}) - (U_{200} - \bar{U}_{200})} \tag{2.1}$$

The brace indicates area averaging, and all velocities are meaned over the summer (JJAS) season. The index is shown here in Fig. 2.6 using the ERA-40 dataset. The study of Webster and Yang (1992) is one of several which finds considerable phase and amplitude variations between years, and very different circulation strengths in the two regions of the Asian-Australian monsoon. The most energetic monsoons were found to develop the earliest. Reduced monsoon circulation was confirmed after a delayed onset, and monsoon flows were yet to be established in May over the Arabian Sea and Indian subcontinent in late monsoon years. Sperber *et al.* (2000) noticed a decadal trend of decreasing wind-shear of the DMI in the 1958–1997 dataset of NCEP/NCAR reanalyses, which they put down to a reduction in the land-sea temperature contrast. This trend is also apparent in the ERA-40 data of Fig. 2.6, which also shows short periods of sustained strong or weak monsoons, and monsoons which flip from strong to weak and vice-versa. These characteristics, and their relationship with outside influences, will be discussed in more detail in later chapters. Webster *et al.* (1998) generated monsoon intensity composites from the NCEP/NCAR reanalyses period 1979–1996 using the DMI. Globally coherent patterns were found for dynamically weak and strong years.

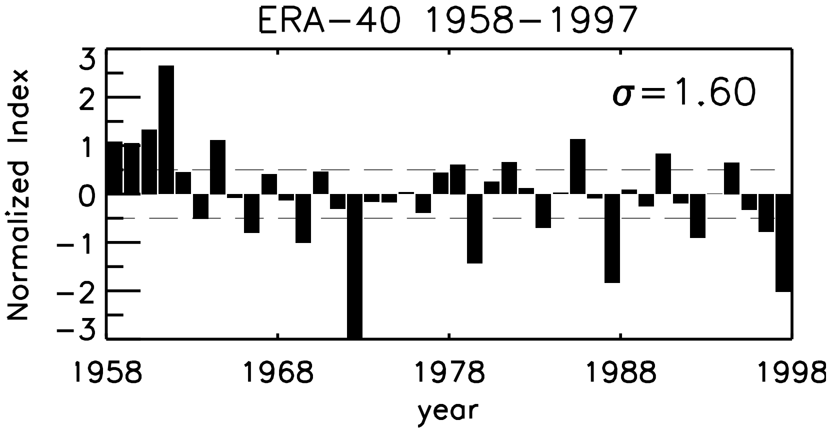

Figure 2.6: The DMI applied to summer (JJAS) data from 1958–1997 in the ERA-40 reanalysis. Also shown is the standard deviation by which the index is normalized, and $\pm 0.5\sigma$ lines.

In weak years, positive OLR anomalies were found over South Asia, Indonesia and the east Pacific, together with negative anomalies over the central Pacific, characteristic of an El Niño response (see later). Non-El Niño weak years also displayed similar signals. The upper-tropospheric (U_{200}) zonal wind anomalies were westerly over the Indian Ocean in weak years, consistent with a weakened jet stream and reduced heating over South Asia. Weak westerlies exist over the Pacific, with perturbations radiating poleward from the central region, most noticeably in the winter hemisphere. U_{850} anomalies mirror those of U_{200} in the monsoon regions, showing a weakened monsoon flow. This antisymmetric wind behaviour is less evident elsewhere. Weakened Pacific trade winds are also noticed. In their DMI-generated weak years during May, Ju and Slingo (1995) noticed a persistent anticyclone over the Arabian Sea bringing dry air into India from the north-west. In China and Southeast Asia, equatorial easterlies push farther west. The monsoon trough from northeast India to the Bay of Bengal is not as well defined.

The strong composites illustrated by Webster *et al.* (1998) show a positive tongue of OLR anomalies over the central and west equatorial Pacific. Negative anomalies over India, the Pacific Ocean and Asia, with minima over Southeast Asia and Indonesia, indicate enhanced convection there. These are consistent (but not uniquely) with a La Niña pattern. U_{200} anomalies are easterly in the eastern hemisphere and westerly in the equatorial Pacific where they radiate poleward. U_{850} shows a stronger monsoon flow, and enhanced easterly Pacific trade winds, which are also confirmed by Ju and Slingo (1995) with their ECMWF reanalyses. The anomalous signal of upper easterlies during strong years is found by Webster *et al.* (1998) as far back as the previous winter, but not at low levels. This suggests external influences are having an influence on the monsoon system.

Study of the interannual variability is further complicated because no solid relationship exists between strengthened monsoon flow and heavier precipitation, and further to this, Ju and Slingo (1995) found no clear relation between the dynamic and rainfall onset dates. Although Sperber *et al.* (2000) found seasonal variations in AIR to be related to characteristic winds, they warn that occasionally the indices do not match up, being of opposite sign in both 1983 and 1985. Other studies such as Wang and Fan (1999) compare a wide range of indices and favour those based on convective variables such as OLR, although only a relatively short dataset is used (1984–1997).

The following section will describe one of the major influences on interannual monsoon variability, ENSO. Other factors are known to play a role in the seasonal rainfall, such as Asian or Eurasian snow cover during the boreal spring. They are, however, outside the scope of this thesis and will not be discussed here.

2.3 ENSO and interannual variability

This thesis focusses on the interannual variation in the Asian summer monsoon and its main influence, the El Niño-Southern Oscillation (ENSO). The interannual variation of summer season (JJAS) Indian rainfall over the last century is shown in Fig. 1.2. Indication is given in the figure of years which can also be classified as El Niño (warm events in the east Pacific), or La Niña (cold events). El Niño occurs predominantly with Indian drought, whilst flood years often feature La Niña events. This relationship is not exclusive however, occasionally being absent or reversed. This section will first consider early studies, before defining the components of ENSO and finally their influences on the monsoon system.

Several studies have looked at the importance of the link between ENSO and the

ASM. In the 1920s, Sir Gilbert Walker first thought of the significance of the Southern Oscillation when he described, ‘A swaying of pressure backwards and forwards between the Pacific Ocean and Indian Ocean.’ In their paper, Webster and Yang (1992) gave an overview of Walker’s earlier findings. Walker felt that the SO was of large enough spatial scale and on a long enough timescale that it could be used as a predictor for the ASM with a reasonable lead-time. Walker’s own measurements of Indian summer monsoon rainfall were found to correlate strongly with subsequent events, discounting his earlier idea that the monsoon was a passive feature influenced by the Southern Oscillation. This led Normand (1953) to state, ‘The Indian monsoon therefore stands out as an active, not a passive feature in world weather’.

2.3.1 ENSO

Before considering the impact of ENSO on the monsoon, a more detailed description of the oscillation will be given. Bhalme and Jadhav (1984) introduced the Southern Oscillation (SO) as an exchange of air between the south-east Pacific subtropical anticyclone and the Indonesian equatorial low. In common with earlier work, they describe the Southern Oscillation Index (SOI) as the anomalous SLP difference between Tahiti and Darwin. Looking at long period data, they find the period of oscillation to be 2–6 years, with most spectral power in the 2–3 year band. Pressure changes of the SO are linked to zonal (Walker) circulations (seen in Fig. 2.4), such that $\mathrm{SOI} > 0$ indicates a strong Walker circulation, with ascending air over Indonesia (near Darwin) and descent over the east Pacific. This leads to surface easterlies and upper level westerlies in the equatorial region.

Bhalme and Jadhav (1984) noticed weak Walker circulations in combination with a warmer, wetter equatorial east Pacific. The authors showed the strength of the Walker circulation to be inversely linked to surface temperature in this region, El Niño and La Niña being used to describe these warmings and coolings. They found 88% of El Niño events to occur when $\mathrm{SOI} < 0$. Schematic diagrams of normal and El Niño conditions are shown in Figs. 2.7a and 2.7b respectively. Under normal conditions (shown

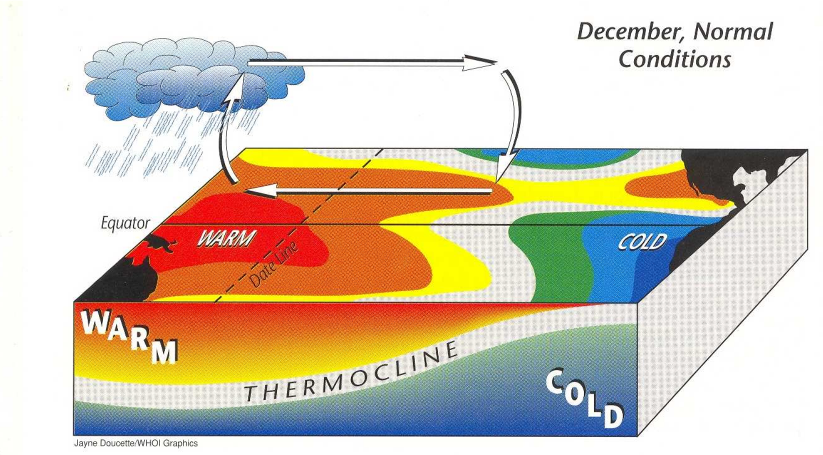

Jayne Doucette/WHOI Graphics

(a) normal conditions

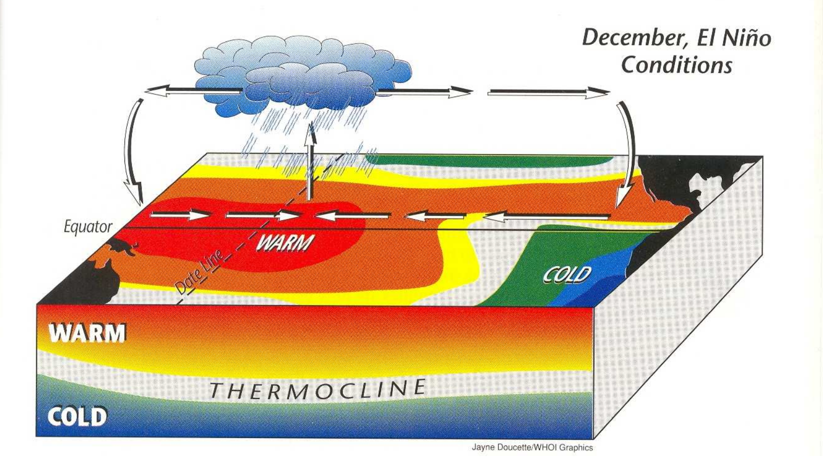

Jayne Doucette/WHOI Graphics

(b) El Niño conditions

Figure 2.7: Schematic diagrams illustrating the state of the equatorial Pacific and subsurface waters during (a) normal and (b) El Niño winters. Taken from Philander (1992), ©Jayne Doucette, Woods Hole Oceanographic Institution

for the boreal winter in Fig. 2.7a), easterly trade winds keep convection confined over the waters of the west Pacific warm pool. The strong westward winds cause equatorial upwelling in the Pacific Ocean, replenishing cool water in the central regions. The easterly wind bias causes increased sea-surface height in the west, as warm waters pile up there. The thermocline (the interface at which there is maximum vertical gradient in the subsurface ocean temperature, separating the warm upper ocean from the deep ocean, preventing vertical mixing) features a mean west-to-east tilt under normal conditions as shown in Fig. 2.7a.

Typical behaviour during El Niño conditions is succinctly described by Krishna Kumar *et al.* (1999), and shown in Fig. 2.7b. The coupled response to east Pacific warming involves longitudinal shifts in the tropical Walker circulation. During El Niño, the rising arm of the Walker cell, normally over the west Pacific, shifts toward the warmer central and eastern waters, taking with it tropical convection. This shift in the zonal circulations causes low-level convergence over the equatorial Indian Ocean, driving an anomalous Hadley circulation whose descent over the Indian subcontinent suppresses convection and precipitation. High pressure over the west Pacific and eastern Indian Ocean is contrasted with anomalous lows in the east and central Pacific ($\mathrm{SOI} < 0$). El Niño develops due to a disruption to the seasonal cycle of trade winds, most likely during boreal spring when zonal temperature and pressure gradients along the equator are at a minimum ($e.g.$, Webster and Yang, 1992). Westerly wind events (WWEs), which have been implicated in the onset of El Niño ($e.g.$, in 1997, Lengaigne *et al.*, 2002), cause warm water to accelerate down the sea-surface height gradient, together with the transmission of a downwelling Kelvin wave which propagates along the thermocline. As water moves eastward down the height gradient, sea surface height anomalies become nearly $0.4\mathrm{m}$ at the event peak (during the 1997 El Niño, McPhaden and Yu, 1999). As the edge of the warm pool moves further east and equatorial upwelling is suppressed by the Kelvin wave, the central and east Pacific regions warm up. The trade winds slacken even further and the zonal temperature gradient is reduced or even reversed. Associated with these changes at sea-level are changes to the subsurface, the thermocline responding to the advancing eastward warm waters by decreasing in gradient (shown in Fig. 2.7b), shoaling in the west and deepening in the east. This evolution of the thermocline during warm episodes was first described by Bjerknes (1966). In a neat summary of event growth, Collins (2000a) suggest that warm SST anomalies in the east (or central) Pacific cause the trade winds to slacken (via reduced zonal SST gradients), thus reducing the equatorial Ekman upwelling. Hence SSTs are further warmed, reinforcing the original anomaly. This process has come to be known as *Bjerknes feedback*, after its first description by Bjerknes (1969).

La Niña, the opposite phase to El Niño, features cooling in the central to east Pacific region, associated with enhanced easterly trade winds and a steeper thermocline with more upwelling in the east. Accordingly it is often thought as an extension to the seasonal cycle, intensifying the usual conditions. Whilst Bjerknes feedback also plays a role in the growth of these negative SST anomalies, it is unable to explain the termination of an event, or its phase change (conditions moving from El Niño to La Niña). Given that ENSO can be reasonably simulated in GCMs, argue Webster and Yang (1992), suggests it must have a straightforward mechanism. Several simple numerical models have tried to address this problem, giving idealised El Niño-La Niña variations against a climatological background state.

Zebiak and Cane (1987) provided one of the major early models of the El Niño-La Niña system, consisting of a Gill atmosphere (Gill, 1980) coupled to a linear reduced gravity model of a small region of the tropical Pacific. The atmosphere is based on steady-state linearized shallow water equations on the equatorial beta plane, incorporating Rayleigh friction and Newtonian cooling. The equations predict anomalies about an imposed seasonally varying basic state. An authoritative treatment of modelled ENSO dynamics is beyond the scope of this thesis, but the main simulated properties of the ZC model (Zebiak and Cane, 1987) will be outlined. Without anomalous external forcing, the ZC model produces irregular warm events in the basin, favouring a period of 3–4 years. El Niño development usually occurs during boreal summer, with sharp termination the following spring. This strong phase-locking of anomalies to the annual cycle is found by Zebiak and Cane (1987) to relate to seasonal changes in the coupling strength between the ocean and atmosphere. The model also simulates some characteristics of

El Niño consistent with observations, including westerly wind anomalies in the central regions, and the location of maximum SST anomalies in the east.

To help explain the period of oscillation, Suarez and Schopf (1988) create a simple non-linear model which makes allowances for the effects of equatorially trapped ocean waves, through the presence of a time-delay term. From equilibrium, an amplifying mode (such as the Bjerknes feedback) acts on the central Pacific (the region most strongly coupled to the atmosphere), increasing the SST anomaly there. Nonlinear effects, such as advective processes in the ocean or moist processes in the atmosphere must limit growth of the anomaly. Westerly wind anomalies driven by the initial warm SST perturbations initiate Rossby waves on the thermocline. At the same time, the wind forcing deepens the thermocline locally via eastward Kelvin waves, reinforcing the anomaly in a positive feedback. The westward Rossby waves reflect at the western boundary, forming equatorial Kelvin waves. Air-sea coupling is weak in the west due to the depth of the thermocline in the warm pool region, so these returning upwelling waves have little effect until they reach the central-east Pacific. Then thermocline displacements can act to quell the initial disturbance. Suarez and Schopf (1988) model this system using

$$\frac{dT}{dt} = T - T^3 - \alpha T(t - \delta), \tag{2.2}$$

where δ represents the (non-dimensional) wave transit time, and α measures the influence of the reflected signal relative to that of the local feedback. Being a negative feedback yet an imperfect reflection, α must lie within the domain $0 < \alpha < 1$. By this system, the period of oscillation must be at least twice the transit time of waves travelling from the anomaly to the western boundary and returning. It may be more due to imperfect cancellation of the initial warming.

In a more rigorous study of the ZC model, Battisti and Hirst (1989) consider a temporally constant background state. If the full coupled model is linearised, then unbounded growth occurs, leading to unrealistic amplitudes. However the basic characteristics such as the fundamental frequency and growth are determined by linear processes. It is nonlinearities which act primarily to restrict the amplitude, and equatorial wave dynamics in the western ocean basin which are responsible for the delayed negative feedback. Three sources of nonlinearity are suggested, covering the forcing of the atmosphere by surface moisture convergence, ocean wind stress forcing having squared dependence on the surface wind, and ocean SST anomaly dependence on horizontal advection and vertical upwelling. The authors find that only the nonlinear term associated with vertical upwelling is required to moderate event growth. Some simplifications then make their non-linear coupled model identical to that of Suarez and Schopf (1988).

2.3.2 The link to the monsoon

Bhalme and Jadhav (1984) found Indian rainfall data from 1875–1980 to reveal a drier Indian Ocean and large monsoon rainfall deficiency concurrent with weak Walker circulations. Strong Walker cells ($\mathrm{SOI} > 0$), feature cloudiness and rain over Indonesia, east Australia and India, whilst the east Pacific remains dry. Shukla and Paolino (1983) used only Darwin pressure and 1901–1950 Indian summer monsoon rainfall, to show that high (low) Darwin pressure coincides with low (high) monsoon rainfall. (High Darwin pressure represents in general $\mathrm{SOI} < 0$). The persistence of a pressure anomaly was found up to 6 months after the summer monsoon. The *trend* in Darwin pressure beforehand was found to be the most useful predictor, a decrease from winter (DJF) to spring (MAM) preceding a heavy monsoon summer. Knowledge of this trend was found to be more important than the winter or spring absolute values. Thus if spring Darwin pressure was below normal and falling, then Shukla and Paolino (1983) could be confident of a ‘non-occurrence’ of drought the following summer. In their extensive study on the interactive nature of the monsoon and ENSO systems, Webster and Yang (1992) also cite evidence for less precipitation over India when $\mathrm{SOI} < 0$.

Directly correlating the SOI with OLR and U_{200} from 1974–1987, Webster and Yang (1992) found the strongest agreement in the central to east Pacific. In a warm event ($\mathrm{SOI} < 0$), convection is stronger ($\mathrm{OLR} < \overline{\mathrm{OLR}}$), and upper level zonal winds are more easterly. Convection weakens around Indonesia, moving north-east and south-east, representing eastward migration of the SPCZ. Much stronger correlations between OLR and upper level winds exist in winter, with significant patterns over the Indian

Ocean and South Asia. These patterns are absent in summer, especially in the monsoon regions. Thus an advance knowledge of the SOI may be more useful in predicting the winter monsoon. Using 1935–1990 data, Webster and Yang (1992) performed lagged autocorrelations of the SOI. Correlations tended to halve between spring and summer, irrespective of when the lag correlations were commenced. A very rapid drop of correlation between April and May, with no corresponding drop in the autumn meant that only a knowledge of the SOI in spring could be useful for predicting the ASM, whereas the winter monsoon could be predicted up to 6 months in advance. Analogous results were obtained correlating the SOI with zonal winds. The authors term this decline in the prediction-observation correlation as the spring ‘predictability barrier’, limiting the role of SOI for interannual monsoon prediction. Bhalme and Jadhav (1984) had also noted the steep rise in correlation between interannual monsoon rainfall and the SO between spring and summer. However, the relationship between monsoon strength and Pacific trade winds does provide a physical connection between the ASM and ENSO. In spring the Walker circulation is at its weakest, meaning the symmetric system of the Pacific Ocean is least robust and most susceptible to influence. So any anomalous forcing introduced to the system via an anomalous trade wind regime will be communicated to the ocean via wind-stresses, providing the likely mechanism for the monsoon-ENSO link.

Studies by Webster *et al.* (1998) found a better correlation between monsoon rainfall (AIR) and Pacific Ocean SSTs than with the SOI, noticing diminished Indian rainfall following a period of enhanced Pacific SSTs. Thus drought years in the Indian region are usually (but not always) preceded by El Niño periods. Similarly heavy rainfall monsoon summers are usually preceded by La Niñas. Indeed Charney and Shukla (1981) suggested that low frequency variations in lower boundary forcing (such as ENSO) were essential for correct monsoon prediction, and Palmer (1994) later devised a chaotic model of the atmosphere to show that east Pacific warming increased the likelihood of negative rainfall anomalies over India.

Webster *et al.* (1998) also noted the good link between ENSO and the Australian monsoon. Sperber *et al.* (2000) put the exceptions to the usual El Niño-weak monsoon relationship down to the complexity of the system: SST variability in the Pacific being one of many modulators. When looking at monsoon composites in model El Niño and La Niña years, Ju and Slingo (1995) found that those years with warm east/central Pacific SSTs tend to have a delayed onset and weakened circulation, and vice-versa. La Niña years feature stronger monsoon flows than El Niño years. This flow discrepancy is most apparent at the onset and does not persist, such that both sets of years have similar retreat patterns. Webster *et al.* (1998) carried out lagged Indian monsoon rainfall/SST correlations to show a near-zero correlation between spring and early summer, another manifestation of the predictability barrier.

2.4 Indian Ocean SST and interannual variability

Shukla and Paolino (1983) noted that local SST anomalies in the Indian Ocean had an insignificant effect on the monsoon compared to ENSO. Yet the seasonal cycle of SSTs for the northern Indian Ocean and Arabian sea is as dramatic as elsewhere in the tropics, noted Ju and Slingo (1995). Substantial ocean warming occurs due to solar heating and the absence of cloud, due to the prevailing anticyclonic conditions and strong low level inversion. SSTs greater than $29°\mathrm{C}$ are reached by early May, just before the monsoon onset. As the monsoon develops, the westerly flow causes cold upwelling off the Somali coast, increased wind-driven mixing and enhanced surface evaporation. SSTs fall, as seen in Fig. 2.8, reaching a minimum in August, sometimes lower than that in winter. The September retreat and its declining flow pattern allow the waters to warm again, before again cooling with the changing season and southward movement of the solar maximum. Ju and Slingo (1995) also noticed the considerable interannual variability in the seasonal cycle of SSTs. By compositing the seasonal evolution of Arabian Sea SSTs for strong and weak monsoons, a clear relation is found with the season's monsoon character. These are derived from the dynamical monsoon index of Fig. 2.6 and their evolution is shown in Fig. 2.8. Weak monsoon years begin to have greater SSTs in May, which persist through to early winter. No SST differences are observed in winter and spring, illustrating the passive nature of Arabian Sea anomalies, resulting

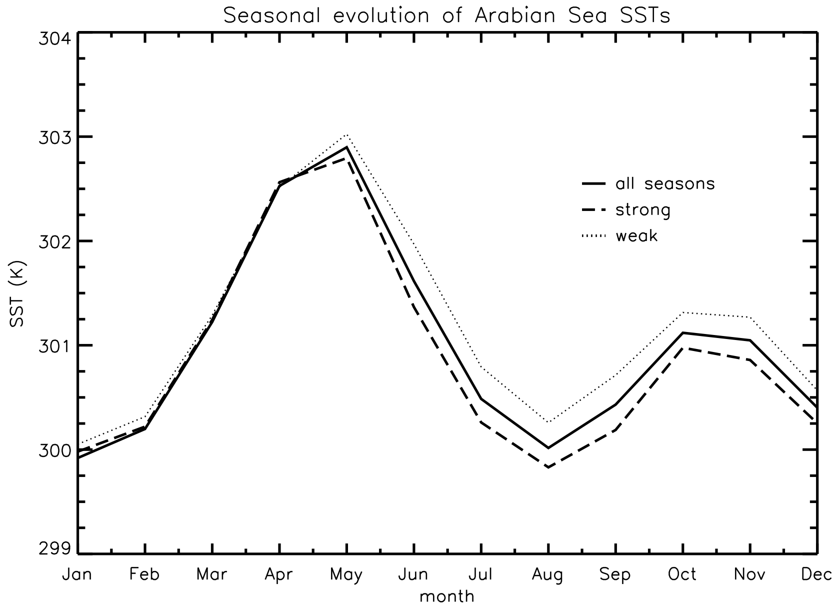

Figure 2.8: Annual cycle of Arabian Sea (0–15°N, 50–70°E) SSTs in ERA-40 data, after Ju and Slingo (1995). Curves for dynamically strong and weak monsoons are also shown, derived from Fig. 2.6.

from changes in the monsoon circulation. The SST difference between weak and strong years, through the nonlinear nature of the Clausius-Clapeyron equation, would represent an enhanced moisture supply to the Indian subcontinent in weak seasons, helping prevent the monsoon becoming too deficient.

The fact that the strength of upwelling off coastal Somalia depends on monsoon dynamics links the monsoon to another phenomenon of the Indian Ocean, that of the dipole mode (also known as the Indian Ocean Zonal Mode, IOZM). First discovered in observations by Saji *et al.* (1999), strong monsoons may lead to a *negative* dipole across the Indian Ocean basin, with strong upwelling leading to negative SST anomalies near Somalia, whilst downwelling occurs near to Sumatra, allowing positive SST anomalies to remain there. This dipole pattern may reverse during weak monsoon years. Saji *et al.* (1999) suggested that the Indian Ocean dipole and ENSO were independent oscillations, although more recent work suggests they may help link the Indian and Pacific regions during oscillations on biennial timescales. The dipole will be returned to in the next section.

2.5 Biennial variability

Variability occurring in the Indo-Pacific region on biennial timescales is particularly important for monsoon regions since it offers a particularly simple method of prediction, strong monsoons being followed by low rainfall in the following summer season, and vice-versa. Such biennial variability was noted in assessments of the Indian monsoon (Mooley and Parthasarathy, 1984, although only in the last 3 decades of their observations), and the East Asian monsoon, especially in southern China (Schen and Lau, 1995). Yasunari (1990) noted the negative correlations between Indian summer monsoon rainfall and central Pacific SSTs to be most strongly correlated on biennial timescales. Over in the Pacific, Rasmusson *et al.* (1990) studied observations over the 1950–1987 period and found a strong biennial peak to complement the longer period (4–5 year) ENSO variations. These were particularly prevalent in surface winds, which seemed to undergo biennial variation whilst strongly phase locked to the annual cycle, introducing a degree of regularity into the ENSO system. In their review of the subject, Webster *et al.* (1998) found prominent peaks in the 2–3 year band of Asian-Australian monsoon rainfall. The oscillation, often called the tropospheric biennial oscillation (TBO), appears fundamental to the monsoon system, with identifiable seasonality and structure. These characteristics were explained in detail by Meehl (1987) who looked at observed data since 1900. Meehl (1987) found that 2 out of 3 years have characteristics of Pacific warm or cold events. Strong or weak monsoon years independent of ENSO share similar characteristics and evolution but with a smaller amplitude. Composites were generated of relatively heavy and light rainfall summers, helping to define a sequence of events in strong and weak annual cycles, a simplified version of which is shown in Fig. 2.9 and summarized below.

1 In a strong monsoon year, perhaps during the onset of a Pacific cold event, the Indian summer features lower pressure and greater convection. Indian Ocean SSTs begin to cool due to a strong subtropical anticyclone and its associated stronger surface winds. A strong subtropical anticyclone also lies in the south Pacific, characteristic of La Niña, which together with the Mascarene High, helps weaken

the circumpolar trough. Suppressed eastern tropical Pacific convection is associated with the mean west-to-east exchange from the Indian to Pacific sectors.

2 The convective maximum moves south-east as it traverses Southeast Asia and north Australia, moving over the warmer ocean. The maximum is maintained in summer and autumn by weaker seasonal easterlies, decreased upper ocean mixing and reduced latent heat flux. Towards the end of the year, the local rainy season becomes established in north Australia. As strong conditions continue, SSTs to the north fall due to stronger westerly surface winds removing heat from the ocean.

3 Warmer SSTs ahead of the convective maximum maintain the strong convection on its eastward path to the Pacific, then decrease as it passes. A relative pressure low to the west and high to the east of the SPCZ lead to anomalous northerlies from the warm regions in the deep tropics.

4 The convective maximum reaches the tropical south-west Pacific SPCZ early in the year, displacing it south over warmer SSTs. By April the low pressure has moved south-east into the South Pacific High. The weakened high causes westerly wind anomalies in the equatorial west Pacific, contributing to warmer water and a deepening of the thermocline in the east. Greater convection established in the SPCZ leads to anomalous pressure gradients and the possible initiation of an El Niño event via the westerly surface wind anomalies in the final transition to a weak monsoon year.

5 A weak monsoon year features warm SSTs and enhanced convection and precipitation in the Pacific east of the SPCZ. Weakened South Pacific and Mascarene Highs, higher pressure in the tropical Indian sector west of the SPCZ (and less rain in the Indian monsoon) are associated with the weakened mean west-to-east mass exchange. In the weak annual cycle, a weaker convective maximum moves east to the Pacific from India, under the opposite conditions to strong monsoons.

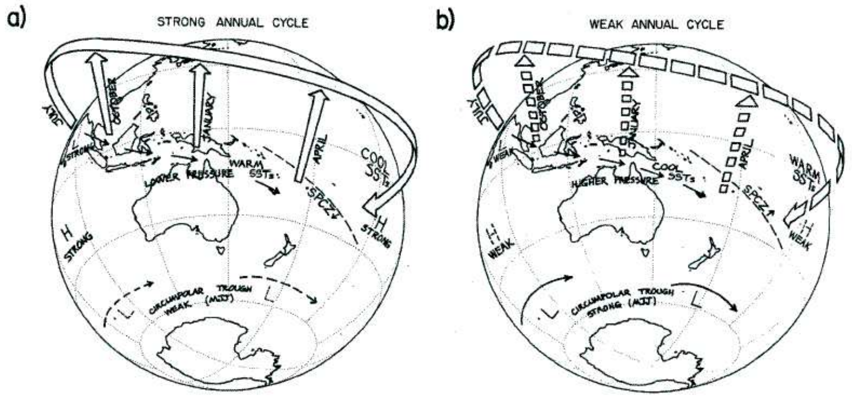

Figure 2.9: Evolution of processes in (a) strong and (b) weak composite annual cycles, from Meehl (1987).

The evolution can then continue, swapping to a strong monsoon year in the following boreal spring. Yasunari (1991) defines the ‘monsoon year’ in a similar fashion, beginning just before the boreal summer and delineating strong and weak annual cycles in the same way. These incorporate the northern winter persistence between the Asian summer and Australian monsoons, which Chang and Li (2000) attribute to the essential bridge of the west Pacific-Maritime Continent region, passing the convection anomaly from northern summer to winter monsoon regions. There follows a change in sign of the precipitation anomalies during boreal spring. This transitional season has already been highlighted as important to ENSO development in §2.2.1, and termed the predictability barrier by Webster and Yang (1992).

Further studies aim to find mechanisms for the existence and behaviour of the oscillation (Meehl, 1993, 1994, 1997). The importance of SST anomalies persisting for an entire seasonal cycle is highlighted by Meehl (1993), implicating thermocline tilts in the warm pool region of the Maritime Continent. In observations, heat content of the upper ocean is found to play an important role in their persistence.

Other work using coupled and atmosphere-only GCMs focuses on the role of anomalous surface temperatures of South Asia (Meehl, 1994, 1997), and associated alterations to mid-latitude circulations. They find that during the northern winter, anomalous mid-latitude circulations can help initiate contrasts in the land-sea temperature gradient which are important for monsoon development (Li and Yanai, 1996). Although

Asian snow cover is implicated as a boundary forcing for the monsoon, it is found in this case to be a symptom of the larger scale mid-latitude circulations, rather than a direct cause of the transition between strong and weak years.

Studying the observational record Meehl and Arblaster (2001) find the three main contributors to the transition season to be: tropical Pacific SST anomalies, atmospheric circulation anomalies related to South Asian surface temperatures and the meridional heating gradient, and Indian Ocean SST anomalies. Further, as any of the transition ingredients are excluded from their composites, the amplitude of the TBO, or likelihood of it occurring, reduces. Using singular value decomposition (SVD) analysis of CMAP and NCEP reanalysis data, Meehl and Arblaster (2002b) find anomalous SST anomalies in the Indian and Pacific Oceans to be the dominant transition conditions. In observations however, these conditions are tied together, and so atmosphere-only GCM integrations are required to determine if each condition alone could cause such a transition. Meehl and Arblaster (2002a) find that indeed they can act alone. Meehl *et al.* (2003) further relate this lower boundary forcing to the large-scale east-west Walker circulations linking the Indo-Pacific sectors. The involvement of Indian Ocean SST anomalies in the proposed TBO mechanisms suggests to Meehl and Arblaster (2002b) that it is somehow connected to the Indian Ocean dipole discussed earlier in §2.4 and originally discovered by Saji *et al.* (1999). More recent studies have further considered the importance of the Indian Ocean. Loschnigg *et al.* (2003) use the NCAR CSM[4] to prove that the IOZM plays a fundamental role in the TBO. The coupled dynamics of the Indian Ocean, together with cross-equatorial heat transport are found to be important mechanisms aiding the transition. Strong Asian monsoons lead to anomalous southward heat transport due the anomalous upwelling driven by the monsoon flow. This transport allows the maintenance of SST anomalies over multiple seasons (already noted in observations by Meehl, 1993) which act to influence the following Asian summer monsoon. Both Loschnigg *et al.* (2003) and Wu and Kirtman (2004) agree that the IOZM acts mainly as a passive response to the monsoon and ENSO, Wu and Kirtman (2004) suggesting the formation of SST anomalies in response to large scale surface

---

[4] Climate System Model

heat flux changes caused by monsoon-ENSO induced circulations. However, Chang and Li (2000) separate the two phenomena. They maintain that whilst ENSO can oscillate without the presence of a monsoon, such forcing is fundamental to the TBO. This seems counter to intermediate GCM studies (Li *et al.*, 2001; Kim and Lau, 2001) which show that ENSO has an increasingly biennial tendency in its evolution when there is strong coupling between ENSO and monsoon wind forcing over the west Pacific. Indeed Kim and Lau (2001) manually impose strong monsoon forcing, and manage to lock ENSO into a 2 year limit cycle.

2.6 Decadal and climatic variations of the monsoon-ENSO system

One of the major issues facing seasonal prediction is the variation on decadal and longer timescales of the teleconnection between Asian summer monsoon rainfall and east Pacific SSTs as suggested in the introduction. Figure 2.10 shows the correlation between the summer (JJAS) All-India Rainfall (Parthasarathy *et al.*, 1994) and HadISST (Rayner *et al.*, 2003) Niño-3 index for the same season. The Niño-3 index is a measure of SST in the east Pacific ($210°$–$270°\mathrm{E}$, $\pm5°\mathrm{N}$), with the seasonal cycle is removed to show only variation from monthly climatological means. Clear variations can be seen on multi-decadal timescales, indicating periods of reduced and increased monsoon predictability. In particular, the clear weakening of the teleconnection over recent decades, to a level not previously seen in the record, is worrying for seasonal monsoon prediction, which relies on the constancy of statistical relations or proper representation of the physics of climate change in a GCM.

Krishna Kumar *et al.* (1999) studied the full All-India Rainfall record (AIR) to suggest that the inverse ENSO-monsoon relationship has broken down over recent decades (Fig. 2.10). The low frequency variations of Indian monsoon rainfall resemble those of various Niño and SO indices until the late 1970s, but diverge thereafter. A southeastward shift in the Walker circulation associated with ENSO was found, featuring

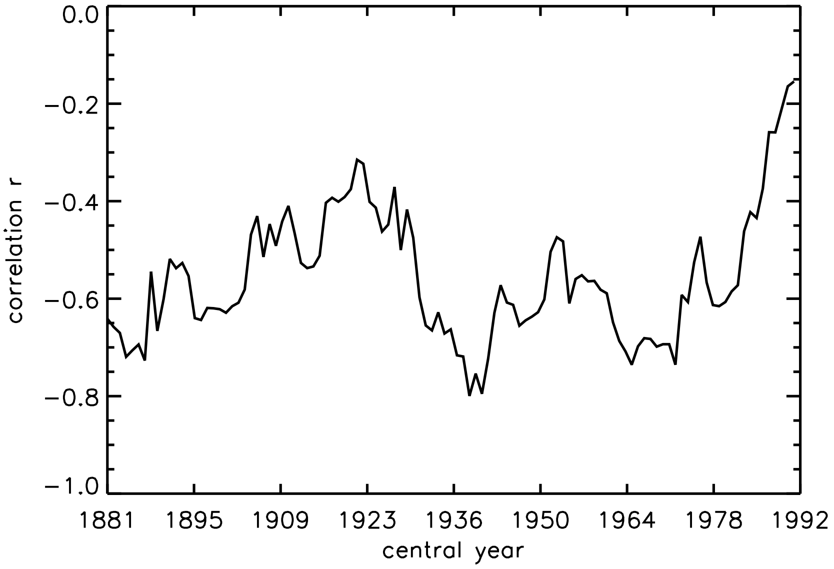

Figure 2.10: 21-year moving instantaneous correlation between summer (JJAS) HadISST Niño-3 region SSTs and the All-India Rainfall (AIR) gauge dataset. Period covered is 1872–2002.

reduced subsidence over the Indian region, favouring normal monsoon conditions, and increased subsidence over southern Indonesia and north-west Australia. This could explain the 1997 case shown in Fig. 1.2, a strong El Niño year, when Indian rainfall remained normal but there was a severe Indonesian drought. Two explanations are offered by Krishna Kumar *et al.* (1999) for the shift, either constituting natural variability of the monsoon-ENSO relationship, or global warming. A warming trend could have broken the monsoon-ENSO link, preventing monsoon failure even during strong El Niños. The authors report that recent warming trends over the Eurasian continent in winter have not been equally matched in the Indian Ocean, increasing the land-sea temperature gradient and strengthening the monsoon. IPCC (2001) noted a trend of up to $4°\mathrm{C}$ over Eurasia east of the Ural Mountains from 1949–1997, whilst over the same period the Indian Ocean warmed only by $1°\mathrm{C}$.

It is not easy to determine whether this recent weakening is part of decadal timescale changes seen earlier in the century, or due to the impact of global warming. Federov and Philander (2000) see this as an important question, asking whether interdecadal changes which lack any obvious physical basis are realistic. The remainder of this section thus splits research into the effect of interdecadal variations, and the effects of climate change on the monsoon-ENSO system.

2.6.1 Interdecadal modulation of the interannual variability

Interdecadal variations to the monsoon are often manifested as modulations to the interannual variability or its association with global conditions. Webster *et al.* (1998) noted the changing relationship between the SOI and Indian rainfall over the last century, and the difference in El Niño event evolution during the periods 1951–1973 and 1981–1992. In the latter, pre-El Niño warming no longer led to reduced monsoon rainfall, which the authors could not attribute to a land-warming trend.

Krishnamurthy and Goswami (2000) found good empirical evidence for the monsoon-ENSO association to vary on interdecadal timescales, such that the Indian summer monsoon season could be found in periods of above or below normal conditions, each of about 30 years. However the interdecadal Pacific SST variability is not as simple as changes in the frequency of El Niño or La Niña events, just as changes to the nature of the Indian monsoon are not confined to greater or fewer flood or drought years. Indeed a study by Torrence and Webster (1999) found periods of high (1875–1920, 1960–1990) and low (1920–1960) variance in the observed monsoon-ENSO system. Interestingly, during periods of high variance in both the monsoon and ENSO, the two systems are highly coherent, suggesting increased seasonal predictability during such epochs.

The summer monsoon strength depends on the regional Hadley circulation. The spatial structures of regional Hadley and Walker circulation anomalies associated with strong (weak) phases of the interdecadal or interannual oscillations are similar. Krishnamurthy and Goswami (2000) visualized these two oscillations acting independently in different phases (Fig. 2.11), the total monsoon variability given by their superposition. In the warm phase of *interdecadal* east Pacific SST variability, regional El Niño Hadley circulations would reinforce the prevailing interdecadal Hadley circulation, thus strongly associating El Niño with monsoon drought. A La Niña would oppose this, allowing internal processes or other influences such as Asian snow cover

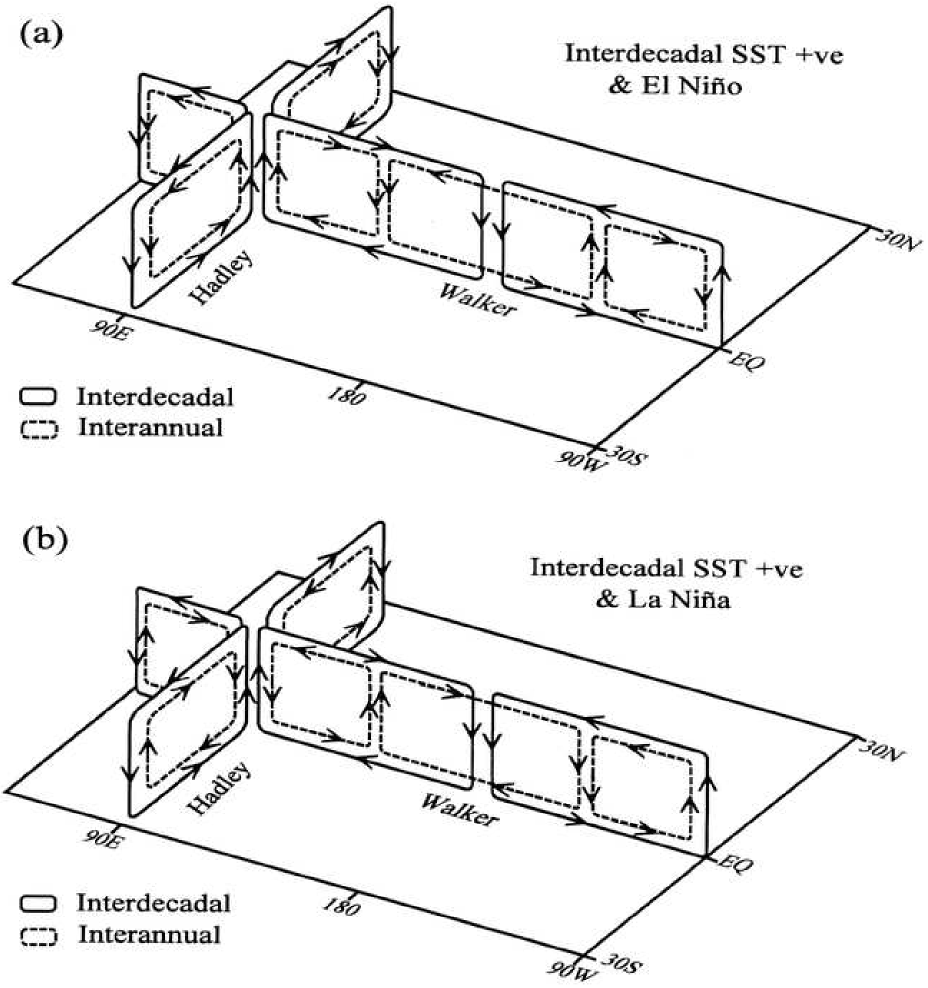

Figure 2.11: The combined effect of interannual and interdecadal modes on the monsoon-ENSO interaction, taken from Krishnamurthy and Goswami (2000).

or Indian Ocean SST anomalies to govern the state of the summer monsoon. In the cold phase of the interdecadal mode however, a La Niña event would reinforce the lower boundary-forcing. Descent over the equatorial Indian Ocean would suppress the equatorial TCZ, allowing the strong convection further north in the form of a strong monsoon. Conversely El Niño would exert little influence over the season.

2.6.2 Climate change

This section first considers GCM experiments which demonstrate changes to the Asian summer monsoon in response to climate change, before reviewing those which see the monsoon in the context of the wider monsoon-ENSO system.

In a study using the Hadley Centre coupled model, Bhaskaran *et al.* (1995) notice a change in the land surface temperature of the Indian subcontinent of 1–$4\mathrm{K}$ at the time of $\mathrm{CO_2}$ doubling, being greatest over the north of India due to the drier surface. Accordingly, the monsoon circulation in their model shifts north by 10°, and becomes more intense. The increased land-sea temperature contrast which may contribute to this process, together with increased atmospheric water content, help increase the moisture convergence over land, increasing the seasonal rainfall. Whilst no change is noted to variations in the monsoon onset date or intraseasonal behaviour, the model does feature enhanced interannual variability of monsoon rainfall, including a tendency for more heavy rain days.

Kitoh *et al.* (1997) used the MRI coupled GCM at $4^\circ \times 5^\circ$ resolution in transient simulations, taking time-slices under $2 \times \mathrm{CO_2}$ and $4 \times \mathrm{CO_2}$ conditions. At $850\mathrm{hPa}$, monsoon westerlies were weaker over the Arabian Sea, although the strong winds had moved to the north, intensifying from the Sahel to northwest India. They too noted that increased moisture content in the warm air led to a larger moisture flux convergence and increased seasonal rainfall over India, although little there was little impact over China. The future monsoon featured larger interannual variability albeit within the bounds of decadal-timescale changes.

In atmosphere-only doubled $\mathrm{CO_2}$ GCM experiments, there is also general agreement on the overall change to monsoon behaviour that concurs with the coupled models mentioned above. (Douville *et al.*, 2000, with 4 different AGCMs) and (May, 2002, using ECHAM4 at T106 resolution) both note an intensification of monsoon rainfall due to the general warming and consequent increase in the atmospheric moisture transport into the Indian region, despite overall weakening of the monsoon flow.

In another transient $\mathrm{CO_2}$ coupled model study by Hu *et al.* (2000), the ECHAM4/ OPYC3 combination simulates a more intense monsoon in the future climate, with a steady upward trend in broadscale precipitation since 1980 in an 1860–2100 integration. Although their current climate simulation overestimates Indian Ocean precipitation at the expense of rainfall over the subcontinent, pronounced enhancement is observed over India in the future. The familiar mechanism for this precipitation increase is cited, involving the larger land-sea temperature gradient enhancing the moisture convergence over land. This is accompanied by a northward shift in the convergence zone. In addition, a westward shift is noted in the northern summer rising branch of the Walker circulation, due to more rapid heating of the Asian continent. Future climate variability of the monsoon is found to be connected with concurrent increases in tropical Pacific SST variability, a finding which is repeated using the same model configuration by Ashrit *et al.* (2001). They contrast this enhanced variability in the monsoon-ENSO system with the recent observed weakening (Fig. 2.10). However the impact of warm events (El Niño) on the monsoon is diminished, whilst the connection between east Pacific cooling (La Niña) remains the constant in their future climate. The anomalous warming over the Eurasian land surface and enhanced moisture content of the atmosphere are cited by Ashrit *et al.* (2001) as possible reasons for the reduced influence of El Niño.

The effects of doubling $\mathrm{CO_2}$ on global spatial scales including the Asian monsoon are considered by Meehl *et al.* (2000), who notice 2 regional processes contributing to climate change. These are the El Niño-like response (discussed in previous studies such as Meehl and Washington, 1996), and high latitude sea-ice response. The sea ice response represents a positive feedback, the warmer future climate causing the ice to melt away. This meltdown exposes the ocean surface with its inherent lower albedo.

The sea ice is then bounded by warmer SSTs, decreasing the areal extent of new ice during the winter season. Consequently shrinking sea ice regions lead to a decreased global albedo. This sea ice feedback does not directly influence the Asian monsoon, being at high latitudes, and will not be considered further here.

The El Niño-like response describes greater warming in the east Pacific than the west, leading to a reduction in the climatological zonal equatorial gradient of SSTs (see Fig. 2.7). This suggested to the authors that warm events in the east Pacific may be correlated with global mean warmth. Meehl *et al.* (2000) test the two climate change responses in two different NCAR GCMs, CSM and DOE[5]. In particular, the El Niño-like response in the two models may be expected to have different influences on the mean monsoon climate.

The DOE model is seen to be very El Niño-like in its climate change response, whilst the CSM undergoes more uniform warming across the Pacific. Accordingly, the CSM features increased precipitation throughout the tropics, whilst a typical El Niño precipitation response is observed in the mean DOE future climate. Focusing on the Indian region, seasonal (JJAS) monsoon rainfall is seen to increase by 11.6% in the CSM future climate, partly due to the faster heating rate of the Asian land surface, increasing the meridional temperature gradient. The precipitation increase over Southeast Asia is suppressed by the mean El Niño conditions in DOE however, reaching only $+1.4\%$. Meehl *et al.* (2000) hypothesize that different systematic errors in the two control integrations could lead to different climate change responses, via different cloud forcing changes linked to the varying degrees of the slackening SST gradient. This is especially relevant to the current study, as shall be seen in later chapters.

Some authors consider the impacts of climate change on the ENSO system alone, given that it has such a large global-scale influence. Timmermann *et al.* (1999) ask if anthropogenic greenhouse gas forcing will change ENSO, using a flux-corrected coupled model forced with the IS92a emissions scenario. Although their control run simulates ENSO with a short (2 year) period, future predictions suggest greater interannual variability with more frequent, stronger cold events and an El Niño-like warming of the

---

[5] U.S. Department of Energy.

mean state.

Collins (2000a) used HadCM2, a version of the Hadley Centre coupled model, to show that there were no statistically significant changes to ENSO behaviour until $4 \times \mathrm{CO}_2$ conditions were considered. The model uses seasonally varying ocean surface heat flux adjustments to prevent climate drift. Under pre-industrial conditions, HadCM2 captures ENSO amplitude well, whilst at $4 \times \mathrm{CO}_2$, a 20% increase is seen, caused by the increased vertical gradient of the equatorial Pacific thermocline, itself relating to the El Niño-like surface warming in the mean. The temporal character of ENSO is also changed, with increases in power at 1.5–3 years, and reduced power at lower frequencies. The shortening period is found to relate to an increase in the meridional gradient of SST in the tropical Pacific, increasing the rate at which heat is discharged from and recharged into the thermocline.

Using a more recent version of the Hadley Centre model (HadCM3), Collins (2000b) found no significant changes to ENSO statistics even at $4 \times \mathrm{CO}_2$. The difference in the way these two models respond to climate change was traced to changes made to physical parametrization in the models leading to different meridional temperature gradients around the equator. These minor changes to the boundary layer scheme and relative humidity trigger altered the cloud responses to climate change and led to less pronounced warming on the equator of HadCM3. Thus the response of a GCM to climate change can depend in a nonlinear way, writes Collins (2000b), on changes in subgrid-scale processes.

In more recent transient studies with the ECHAM4/OPYC3 combination, Timmermann (2001) noticed a transition from stable to unstable ENSO oscillation. This change in linear stability coincides with an abrupt increase in ENSO activity, which the author explained in terms of changing ocean dynamics. Responses of ENSO to climate change, warns Timmermann (2001), as well those of the Asian summer monsoon and other global-scale phenomena, are likely to be model dependent.

2.7 Conclusions

While much work has been done on the Asian summer monsoon and its relationship with ENSO, as this chapter has shown, there are still gaps in knowledge. Those that will be covered in this thesis, in accordance with the aims outlined in §1.2, are listed below.

Chapter 1 introduced the problem of seasonal monsoon prediction using GCMs, and the idea that systematic biases in the mean climate could have a negative impact on the simulation of interannual monsoon variability (Sperber and Palmer, 1996). The effect of these is to degrade the predictability of the monsoon, both in terms of application of the correct lower boundary forcing, and the teleconnection in response to this, as described in §2.3. The effect of such errors will be studied in chapter 3 using a method devised by Inness *et al.* (2003).

The impacts of climate change on the monsoon and its predictability will also be studied. §2.6 outlined previous work in this field, but the impact of climate change on large-scale phenomena in the Indo-Pacific region is very much an open question. This is especially interesting when the recent weakening in the monsoon-ENSO relationship (§2.6) is compared with overall strengthening of the monsoon in climate change simulations (§2.6.2). The impact of climate change on the monsoon system of HadCM3 will be considered in chapter 4. Particularly relevent is the study of Meehl *et al.* (2000) who noticed different climate change impacts in models with different basic states. This issue will also be addressed in chapter 4.

Climate change will be considered alongside interdecadal change to the monsoon ENSO-system in chapter 5. The tropospheric biennial oscillation outlined in §2.5 also has relevance to this study.

Chapter 3

The role of the basic state

3.1 Introduction

In accordance with the motivations of this thesis, this chapter aims to assess the impacts of systematic model errors on simulation of the monsoon-ENSO system.

The Asian summer monsoon affects the lives of more than 2 billion people in India, China and the rest of south-east Asia, mainly through the reliance of agriculture on the timing, duration, and strength of the monsoon season. Sophisticated general circulation models (GCMs) are increasingly being used to predict these details of the monsoon season, potentially allowing crop sowing to be more efficiently timed or contingency plans to be made in the event of flood or drought seasons. However, the limited level of skill in dynamical forecasts for seasonal prediction means that they cannot be exclusively relied upon, and therefore empirical methods are still employed, such as by the India Meteorological Department (Rajeevan *et al.*, 2004).

The state of equatorial Pacific sea surface temperatures has long been regarded as an important predictor of the monsoon, with studies such as Charney and Shukla (1981) and Palmer (1994) suggesting that the low frequency Pacific SST variations predispose the monsoon to either a strong or weak season. Ju and Slingo (1995) also noted that the causal relationship between the monsoon and ENSO was central to seasonal prediction. Thus, GCMs used for seasonal prediction should be able to simulate the teleconnection between equatorial Pacific SST variations and the monsoon. This teleconnection depends on the Walker circulation to deliver the Pacific SST signal to the Indian Ocean sector (see, *e.g.*, Shukla and Paolino, 1983; Webster and Yang, 1992). Further, Meehl and Arblaster (2002b, 2002a) found that the monsoon and ENSO phenomena were part of a wider system termed the tropospheric biennial oscillation (TBO). This TBO involves a transition period in northern spring to the summer monsoon season such that a strong monsoon in the previous year is often followed by a relatively weak one in the following year. The transition is heavily reliant on coupled land-atmosphere-ocean processes, with Indo-Pacific Ocean SST anomalies being dominant. Meehl *et al.* (2003) further stress the importance of SST forcing, whilst highlighting the fundamental role of the Walker circulation in linking the anomalous atmospheric conditions and ocean dynamics across the Indo-Pacific sectors.

Therefore, a GCM should not only be able to simulate the correct Pacific SST variability, but must also produce a correct simulation of the mean Walker circulation in order to reproduce the correct monsoon response to Pacific SST variations. Indeed, Sperber and Palmer (1996) found that GCMs which generate mean climatologies most closely in agreement with observations were more likely to simulate the correct interannual variability of tropical precipitation. So a poorly represented mean state may impact on global teleconnections, and consequently limit the prospects for seasonal monsoon prediction.

The purpose of this study is to examine the role of basic state errors on the simulation of the monsoon-ENSO teleconnection in the Met Office Hadley Centre coupled model HadCM3. A system of limited area flux adjustments will be used to reduce the systematic biases of the GCM in the equatorial Pacific and Indian Ocean basins. The impact of these changes on the simulation of ENSO variability and the teleconnection between ENSO and the monsoon will be assessed. §3.2 will describe the model formulation, datasets used, and experimental design. §3.3 will look at the impact of tropical Pacific SST errors on the basic state of the model and associated mean circulation, first noting the systematic errors to the mean summer climate, and then noting any improvements following flux adjustments. The impact of basic state changes on monsoon variability will be documented in §3.4 and changes to the ENSO behaviour of the model will be described in §3.5. The monsoon-ENSO teleconnection will be considered in §3.6, followed by conclusions in §3.7.

3.2 Model, observed datasets, and experimental design

3.2.1 The HadCM3 coupled model

HadCM3 is a fully coupled general circulation model combining comprehensive atmosphere and ocean components. As a state-of-the-art coupled model, it was widely used to provide climate change scenarios for the Intergovernmental Panel on Climate Change Third Assessment Report (IPCC 2001). The simulated climate of HadCM3 is stable so that multi-century integrations can be performed with no significant climate drift, as noted by Johns *et al.* (2003).

Pope *et al.* (2000) provide a detailed description of the atmospheric component, HadAM3. The atmospheric component of HadCM3 has a regular grid of 3.75° longitude by 2.5° latitude, approximately comparable to a T42 spectral resolution. The default vertical resolution is 19 levels, but 30 levels are used in this study, halving the layer thickness in the mid-troposphere to $50\mathrm{hPa}$. This produces more realistic representation of the intraseasonal behaviour of tropical convection such as the Madden-Julian Oscillation (MJO), as found by Inness *et al.* (2001). A subsequent study (Spencer and Slingo, 2003) also found precipitation to respond better to high SSTs in the L30 version.

The oceanic component has a uniform resolution of 1.25° by 1.25° with 20 levels in the vertical. Gordon *et al.* (2000) describe the design of the ocean component in detail. The ocean and atmosphere components of HadCM3 are coupled once per day.

The L30 version of HadCM3 was integrated as a control (pre-industrial $\mathrm{CO_2}$) run for 100 years, after a 10-year spin-up period with initial conditions taken from an L19 integration of HadCM3. The L30 version of the model is also stable and its climatology is similar to that of the standard L19 version.

3.2.2 Observed datasets

Various observationally based datasets have been used to evaluate the model's performance, to identify the key systematic errors and to provide a description of monsoon variability and its teleconnections with El Niño. The recently completed ERA-40 dataset (Uppala *et al.*, 2005), covering 1958–1997, has provided the principle source of data for evaluating the model and describing monsoon variability. ERA-40 is based on a T159 L60 version of the ECMWF Integrated Forecasting System, incorporating externally produced analyses of sea-surface temperature (SST) from the Met Office (pre-1981) and NCEP (post-1981). Since precipitation is regarded as one of the least reliable fields, quantitatively, from reanalyses, the Climate Prediction Center Merged Analysis of Precipitation (CMAP) dataset (Xie and Arkin, 1997) is also used to assess the model's mean climate. However, to study monsoon variability and its teleconnections with ENSO, ERA-40 precipitation is used since it provides a longer dataset. For consistency with the dynamical fields, sea surface temperatures from ERA-40 have been used through out this study, for model evaluation and for describing observed monsoon variability.

In addition, the All-India Rainfall (AIR) dataset (Parthasarathy *et al.*, 1994), based on rain gauge data, has been used to provide another measure of monsoon variability. These data have been obtained from `http://www.tropmet.res.in` (2003). Data on oceanic temperature structure has been obtained from the Levitus dataset, (Levitus and Boyer, 1994).

3.2.3 Design of the flux-adjusted experiment

Flux adjustments were originally applied to coupled GCM integrations to prevent climate drift, such as in the previous version of the Met Office coupled model (HadCM2, Johns *et al.*, 1997). More recent model developments have made such corrections unnecessary for this purpose. In this case a flux-adjusted integration of HadCM3 is used to correct *systematic* errors in the mean tropical climate, to study the role of the basic state in the simulation of the Asian summer monsoon and its variability.

The flux adjustment procedure employed here was first carried out by Inness *et al.* (2003) to investigate the sensitivity of MJO simulation to basic state errors in low-level zonal wind and SST, crucial components of the proposed coupled mechanism for the MJO. The coupled model on 30 levels is first run for 20 years, with the SSTs from $10°\mathrm{S}$–$10°\mathrm{N}$ in the Indian and Pacific Oceans being relaxed back to climatology on a 14 day timescale. The relaxation timescale is controlled by a Newtonian relaxation constant in the model ($\sim 164\mathrm{W}/\mathrm{m}^2/\mathrm{K}$), the same value used by the Met Office to prevent drift in HadCM2. This timescale is chosen such that SST is maintained close to a prescribed state, while still allowing them to evolve over fairly short periods. The climatology used by Inness *et al.* (2003) was the GISST dataset 1960–1990 (Parker *et al.*, 1995). Whilst not ideal to consider relaxations from pre-industrial climate to some twentieth century scenario, this is in common with other coupled model control experiments when global flux correction was required. In any case, the difference in climate signal between the selected timescale and late nineteenth century is very small compared to the systematic errors in question.

Between $5°\mathrm{S}$–$5°\mathrm{N}$ the relaxation is applied in full, but is ramped down to zero at $\pm 10°$ such that SSTs outside of this band are freely evolving. Adjustments are made to this narrow latitudinal region because we wish to have as small an impact as possible on the basic state of the GCM, whilst fixing the coupled systematic error in the equatorial region, as explained by Inness *et al.* (2003).

The anomalous heat fluxes are saved and averaged to generate a mean annual cycle of flux adjustments. No adjustment is made to the wind stress. A second model integration for 100 years (HadCM3FA) then applies the flux adjustment cycle at the ocean surface. Daily flux adjustment values are interpolated linearly between monthly mean values. This strategy constrains the mean equatorial SSTs in the GCM close to observed values whilst still allowing variability of SST about the adjusted mean state.

3.3 The influence of tropical Pacific SST errors on the GCM basic state

To determine the influence of the basic state on the simulation of the monsoon-ENSO teleconnections, the mean climate of the model first needs to be assessed. Inness *et al.* (2003) documented the major tropical systematic errors in HadCM3 for the October-April season, and to a large extent, their findings are also true for the boreal summer (JJAS) season. Figure 3.1 shows the mean surface temperature, 850mb winds and precipitation for HadCM3 in JJAS, together with differences from ERA-40 and CMAP. Typical of many coupled models, the central equatorial Pacific is too cold by about 3K, with the waters around the Maritime Continent being too warm. Across the equatorial Pacific the easterly trade winds are too strong by about $5\mathrm{ms}^{-1}$, and HadCM3 also develops excessive precipitation around the Maritime Continent. Inness *et al.* (2003) describe these low-level wind, precipitation, and SST errors in terms of a coupled mechanism whereby the strong easterly winds confine the warm pool to the Maritime Continent. Convection is also confined to this region and is too strong, driving a strong Walker circulation with strong trades. In the central and east Pacific the anomalous easterlies lead to upwelling of cold water via Ekman divergence. The zonal SST gradient across the Pacific is thus enhanced, further reinforcing the excessive trade winds in HadCM3.

Over the Indian Ocean sector the main features of the monsoon flow are reasonably well simulated by HadCM3. The strength and position of the low level monsoon jet are captured, although the westerly flow across India and the southern Bay of Bengal is rather strong. The cross-equatorial component of the flow extends too far eastward rather than being confined to the Somali Jet, possibly related to the resolution of the atmospheric component of HadCM3. The main precipitation error in the Indian sector is a large dry bias just south of the equator in the centre of the Indian Ocean, arguably related to the systematic errors over the Maritime Continent (Neale and Slingo, 2003). Over India itself, rainfall totals are slightly too high on the west coast and somewhat deficient in the north-west. HadCM3 thus features several indicators of a bias towards a

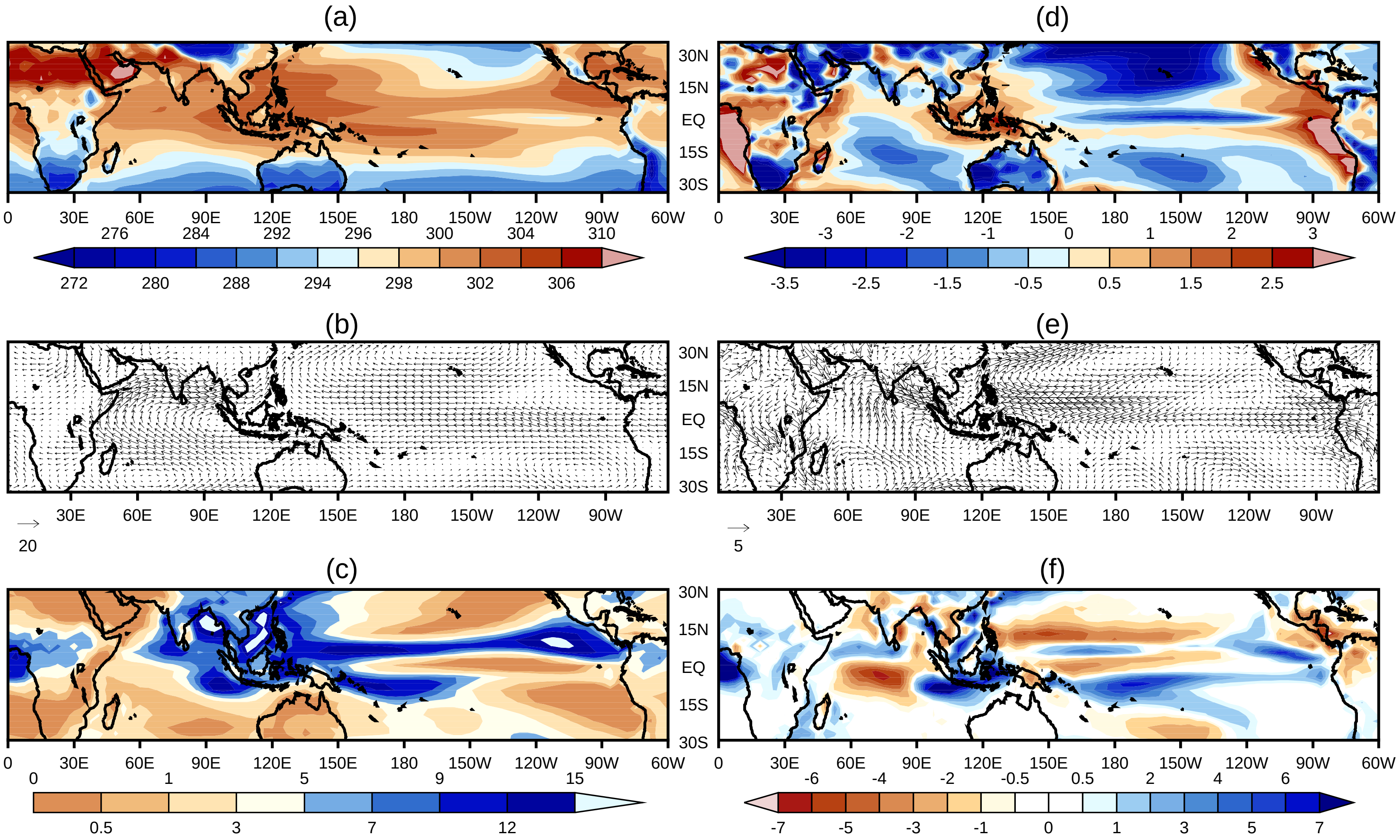

Figure 3.1: HadCM3 summer (JJAS) climatologies of (a) surface temperature (K), (b) $850\mathrm{hPa}$ winds (ms^{-1}) and (c) precipitation ($\mathrm{mm.day}^{-1}$). Panels (d) to (f) show differences in these fields from ERA-40 (d,e) and CMAP (f). Unit wind vectors are $20\mathrm{ms}^{-1}$ (climate) and $5\mathrm{ms}^{-1}$ (anomaly).

strong monsoon in its mean summer climate, such as the enhanced Pacific trade winds and stronger monsoon westerlies (see, $e.g.$, Webster *et al.*, 1998). So the model, although simulating the basic monsoon behaviour quite well, has some systematic errors, particularly in the Pacific sector, which may impact on the simulation of monsoon interannual variability. This will be investigated in §3.4.

Figure 3.2a shows the annual mean of the ocean heat flux adjustments applied to HadCM3FA to correct the model systematic errors in the Indo-Pacific sector. Large positive fluxes go into the ocean in the central equatorial cold tongue (up to $186\mathrm{Wm}^{-2}$ at $120°\mathrm{W}$). Adjustments are much smaller in the Indian Ocean and west Pacific warm pool, no greater than $\pm 30\mathrm{Wm}^{-2}$. The peak-to-peak amplitude of the annual cycle of flux adjustments (Fig. 3.2b) is generally small in this region, except in the upwelling region off the African coast. Figure 3.3d shows the impact of these flux adjustments on the JJAS SST climatology of HadCM3FA. As intended, the central equatorial Pacific has warmed by up to $2.5\mathrm{K}$ and SSTs around the Maritime Continent have been reduced by up to $1.5\mathrm{K}$. The overall effect is thus to extend the west Pacific warm pool eastwards towards the date-line (Fig. 3.3a) and to provide a better simulation of the zonal SST gradient.

The improved zonal temperature gradient across the west Pacific has reduced the anomalously strong easterly trades, whilst over the Indian Ocean, the zonal component of flow on the equator is more easterly. The monsoon flow across the Arabian Sea and the Indian peninsula is reduced, and there is an overall improvement in the simulation of the low level winds. Comparison of the precipitation changes (Figs. 3.3f and 3.1f) shows that the flux adjustments force precipitation changes which are opposite in sign to the systematic errors in HadCM3 throughout most of the Indian Ocean and Pacific sectors. In particular, the excessive precipitation around the Maritime Continent has been reduced, with more rain occurring along the west Pacific ITCZ, and also just south of the equator in the Indian Ocean. Over India itself, the west coast is drier in HadCM3FA. However, the north west of India, which was already too dry in HadCM3, is now even drier in HadCM3FA.

These precipitation and wind changes over the tropical Pacific in both winter (In-

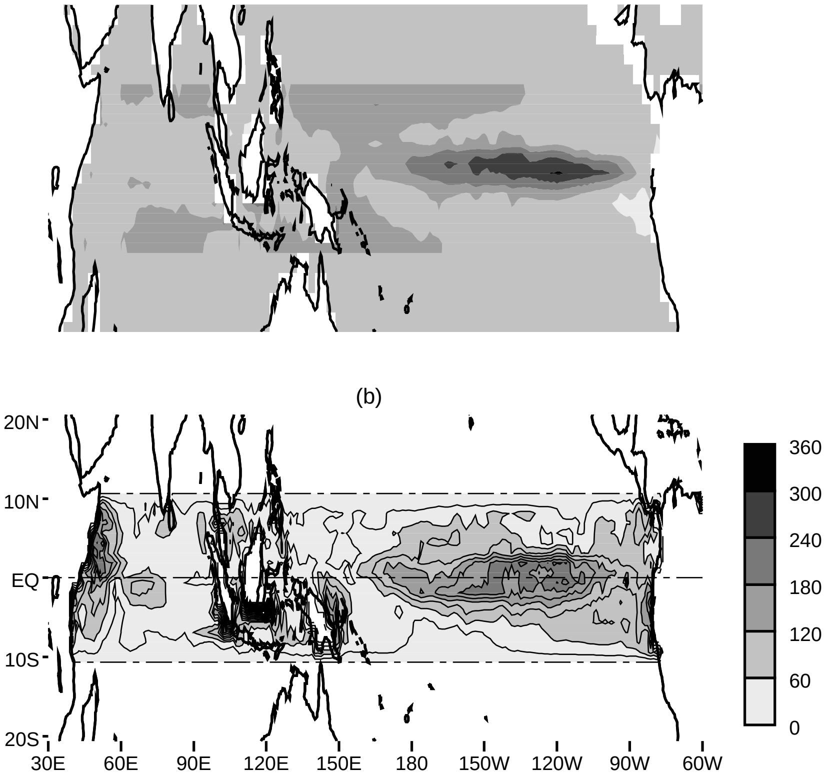
(b)
20N
10N
EQ
10S
20S
30E
60E
90E
120E
150E
180
150W
120W
90W
60W
360
300
240
180
120
60
0

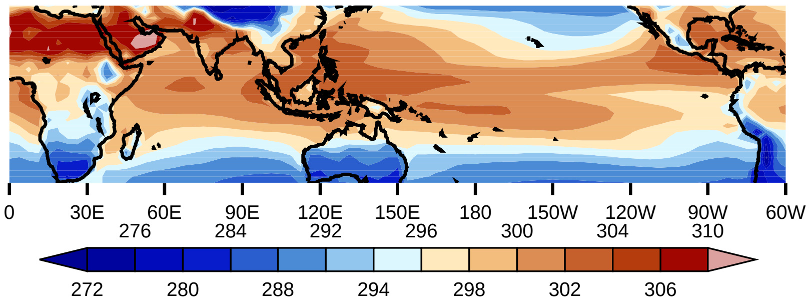
0
30E
60E
90E
120E
150E
180
150W
120W
90W
60W
276
284
292
296
300
304
310
272
280
288
294
298
302
306

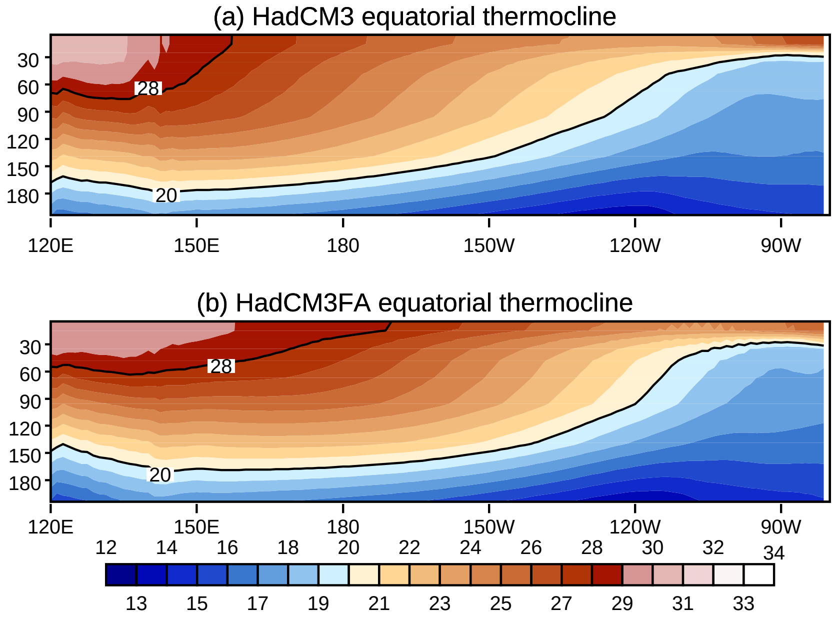

Figure 3.4: Annual mean thermocline profile along the equatorial (0.625°N–0.625°S) Pacific for (a) HadCM3 and (b) HadCM3FA. The 20°C and 28°C isotherms are highlighted.

method is to consider the evolution of lower and upper level winds in the monsoon region. Figure 3.5 shows the mean annual cycle of upper ($200\mathrm{hPa}$) and lower ($850\mathrm{hPa}$) tropospheric winds, (after Webster and Yang, 1992). The region chosen for study, 5–$20^\circ\mathrm{N}$, 40–$110^\circ\mathrm{E}$, covers India, Saudi Arabia, Thailand and the western part of the Maritime Continent, as well as most of the northern Indian Ocean including the Arabian Sea and Bay of Bengal. It is this region that undergoes the major shifts in wind associated with the Asian summer monsoon. Rather than undergoing a reversal in mid-April as in ERA-40, the low-level winds in HadCM3 change direction about a month earlier in mid-March (Fig. 3.5). Thus the anticyclone over the Arabian Sea is giving way to the Somali Jet just north of the equator in the Indian Ocean too early. The flux adjustments have made no significant alterations to the timing of the monsoon, both in terms of its onset and withdrawal, although at upper-levels the winds are about $5\mathrm{ms}^{-1}$ more westerly in the preceding spring with flux adjustments.

One of the factors contributing to the onset of the Asian Summer Monsoon is the dramatic warming of the Arabian Sea during spring, as discussed by Ju and Slingo (1995). The observed SSTs rise through March and April and peak in May, before the

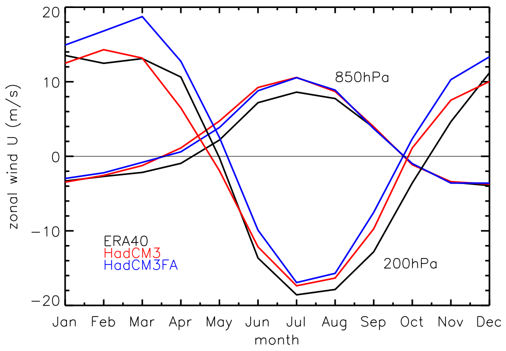

Figure 3.5: Annual cycle of 850 and $200\mathrm{hPa}$ level winds in ERA-40, HadCM3 and HadCM3FA in the region 5–$20°\mathrm{N}$, 40–$110°\mathrm{E}$.

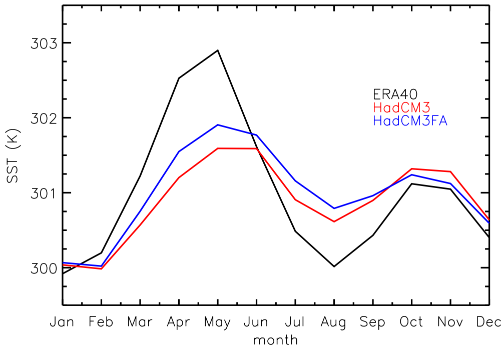

Figure 3.6: Annual cycle of Arabian Sea (0–$15°\mathrm{N}$, 50–$70°\mathrm{E}$) SSTs in ERA-40, HadCM3 and HadCM3FA.

strong monsoon flow in the form of the Somali Jet increases the upper ocean mixing and evaporation, as well as generating cold upwelling off the Somali coast. Thus SSTs fall, reaching a minimum in August. The retreating monsoon allows temperatures to rise again, peaking again in October. In both versions of the GCM, the same basic temperature cycle is present but substantially damped, as seen in Fig. 3.6, suggesting that the early monsoon onset in HadCM3 is related to other factors such as land surface warming. After flux adjustments, the peak of Arabian Sea SSTs in May is slightly higher, but since flux adjustments in the Indian Ocean are minimal (Fig. 3.2), the resulting difference between the two model versions is small. This suggests any changes in the nature of the monsoon are communicated by the atmospheric teleconnection to the Pacific, and are not due to different Indian Ocean behaviour. The seasonal cycle in the Arabian Sea is a fundamental error of the model and, as shown by Spencer *et al.* (2005), is related to major errors in the depth of the mixed layer. It is also possible that the warmth of the Arabian Sea during the monsoon season may be a contributory factor in the overly strong monsoon in HadCM3.

3.4 The role of the basic state in monsoon variability

3.4.1 Representation of monsoon variability

Monsoon variability can be determined in several ways, from the study of the large-scale circulation, to more localized indicators such as the rainfall over a particular area of interest. Here, a dynamical monsoon index (DMI), first suggested by Webster and Yang (1992) is used as a measure of the summer (JJAS) monsoon strength over the south Asia region (5–$20°\mathrm{N}$, 40–$110°\mathrm{E}$). The DMI is a measure of the anomalous zonal wind shear, and was defined in Eq. (2.1). The use of such a measure allows the selection of extreme monsoon summers, which exhibit globally coherent patterns ($e.g.$, Ju and Slingo, 1995; Webster *et al.*, 1998; Sperber *et al.*, 2000). An alternative would be the selection of extreme seasons based on more local rainfall data, such as the All-India Rainfall timeseries. However, the extent to which GCMs can represent such localized rainfall variability is limited by their resolution, hence the choice here of the DMI as an index of the strength of the large-scale monsoon circulation. As will be noted later, the results are largely independent of the precise index used.

The time series of the DMI for ERA-40 (40 years) and the 2 GCM integrations (100 years) are shown in Fig. 3.7, along with the standard deviation for each time series. Note that in HadCM3, the interannual variability of the monsoon circulation is too weak, whereas in HadCM3FA it is too strong. Those years in which the DMI falls outside of half a standard deviation from the mean have been defined as strong or weak monsoons in terms of their circulation.

3.4.2 Monsoon interannual variability in the GCM

By compositing the dynamically strong and weak monsoon seasons, the global climate anomalies associated with anomalous monsoons can be constructed. Figures 3.8 and 3.9 show the strong minus weak difference plots of lower tropospheric wind/precipitation and surface temperature respectively. These composites could also be made by using the All-India rainfall to define strong and weak years. If this is done (not shown here),

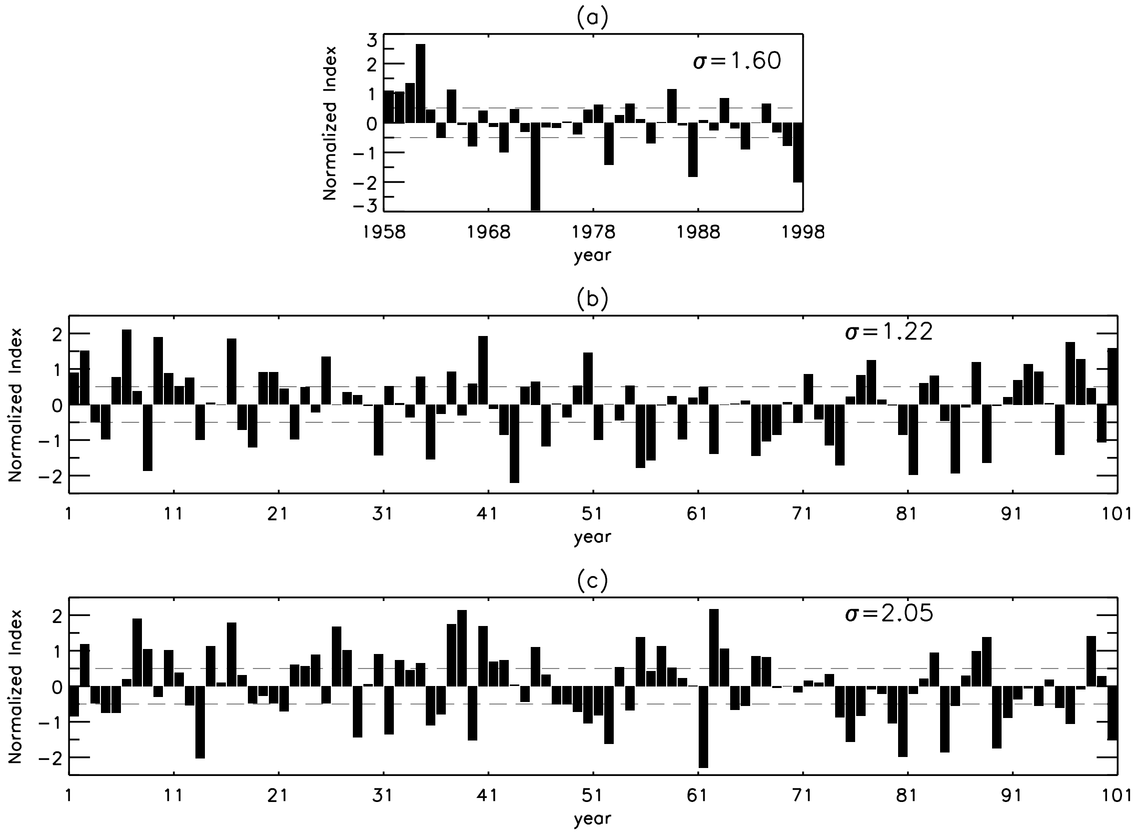

Figure 3.7: The dynamical monsoon index as defined in Eq. (2.1) averaged over 5–20°N, 40–110°E after Webster and Yang (1992), for (a) ERA-40, (b) HadCM3 and (c) HadCM3FA. Note that the years in each of the two model runs are entirely independent.

the overall patterns are very similar to those shown in Figs. 3.8 and 3.9, the main difference being that the rainfall signal over India is stronger if AIR is used to define the composites.

Table 3.1 shows the correlation between the summer monsoon wind strength (DMI) and Indian rainfall (AIR). For the model integrations the rainfall regions cover the Indian region as described by Gadgil and Sajani (1998). For comparison with the models, the ERA-40 DMI is correlated with the All-India Rainfall gauge dataset. HadCM3FA

HadCM3	HadCM3FA	ERA-40/AIR
0.25	0.47	0.55

Table 3.1: Correlation between the summer (JJAS) dynamical monsoon index (DMI) and the All-India Rainfall (AIR) for the two models and the reanalysis/observations.

features a stronger and more realistic relationship between monsoon dynamics and precipitation, consistent with the results shown in Fig. 3.8.

In the reanalysis (ERA-40), strong monsoons have several characteristics, both local to India and further afield. Figure 3.8a shows stronger easterly trade winds across all of the equatorial Pacific during strong monsoon summers. This is a well-known signature of strong monsoons, as suggested by Webster and Yang (1992) and Webster *et al.* (1998). The South Pacific High is also found to be stronger, as noted by Meehl (1987). Figure 3.8a clearly shows a stronger south-westerly monsoon flow across India, continuing on over Thailand and Burma. As expected, India is wetter in strong monsoon years, but there are also precipitation signals elsewhere, with the north-west Maritime Continent and equatorial Pacific being drier and the south east Maritime Continent wetter.

In terms of surface temperatures (Fig. 3.9a), the results from ERA-40 show that SSTs in the central to eastern Pacific are reduced by up to $2\mathrm{K}$ during strong monsoons, characteristic of a La Niña pattern and consistent with cold upwelling in the east and Ekman divergence at the surface with the strengthened trades. The stronger monsoon flow over the Arabian Sea causes stronger upwelling and increased evaporation, resulting in local cooling. Indian land surface temperatures are up to $2\mathrm{K}$ cooler during strong monsoon summers, consistent with increased precipitation over the subcontinent (Fig. 3.8a).

HadCM3 represents some of the features associated with monsoon interannual variability correctly but other aspects are less well captured. The monsoon flow across the Arabian Sea and India is stronger during strong monsoons, but this strengthening does not extend across the Bay of Bengal. Instead there is an increase in westerly flow on the equator in the eastern Indian Ocean, which is the equatorial branch of a cyclonic circulation in the southern Indian Ocean. The circulation error present over the Bay of Bengal in both versions of the GCM indicates a tendency of the models to have very tight zonal structures, an independent error not alleviated by flux adjustments.

The increase in precipitation over India during strong monsoons in HadCM3 is rather weak. The strengthening of the Pacific trade winds is confined to the western

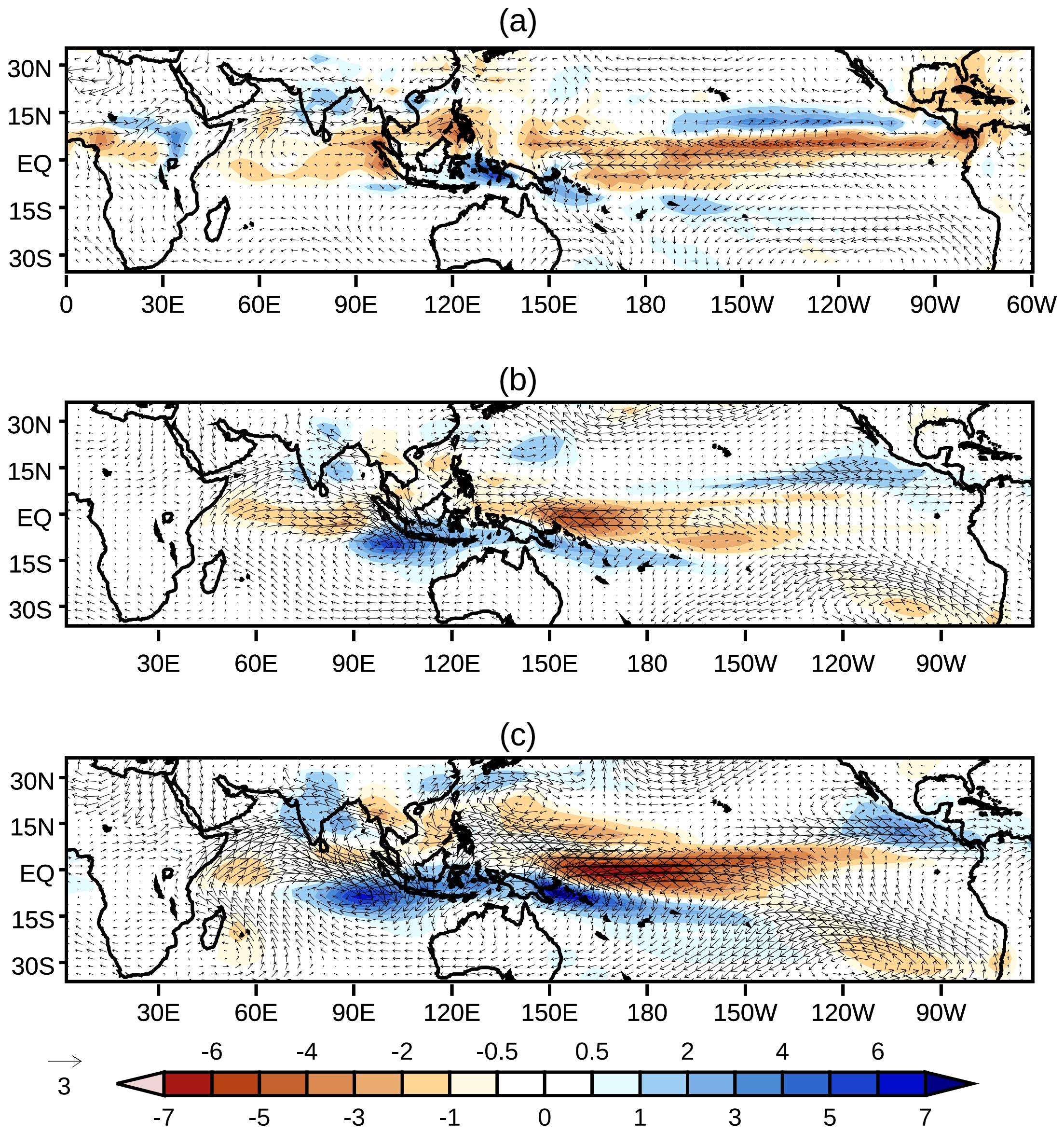

Figure 3.8: Strong minus weak summer (JJAS) composite difference plots of lower tropospheric $(850\mathrm{hPa})$ winds and precipitation for (a) ERA-40, (b) HadCM3, and (c) HadCM3FA. Unit wind vectors are $3\mathrm{ms}^{-1}$.

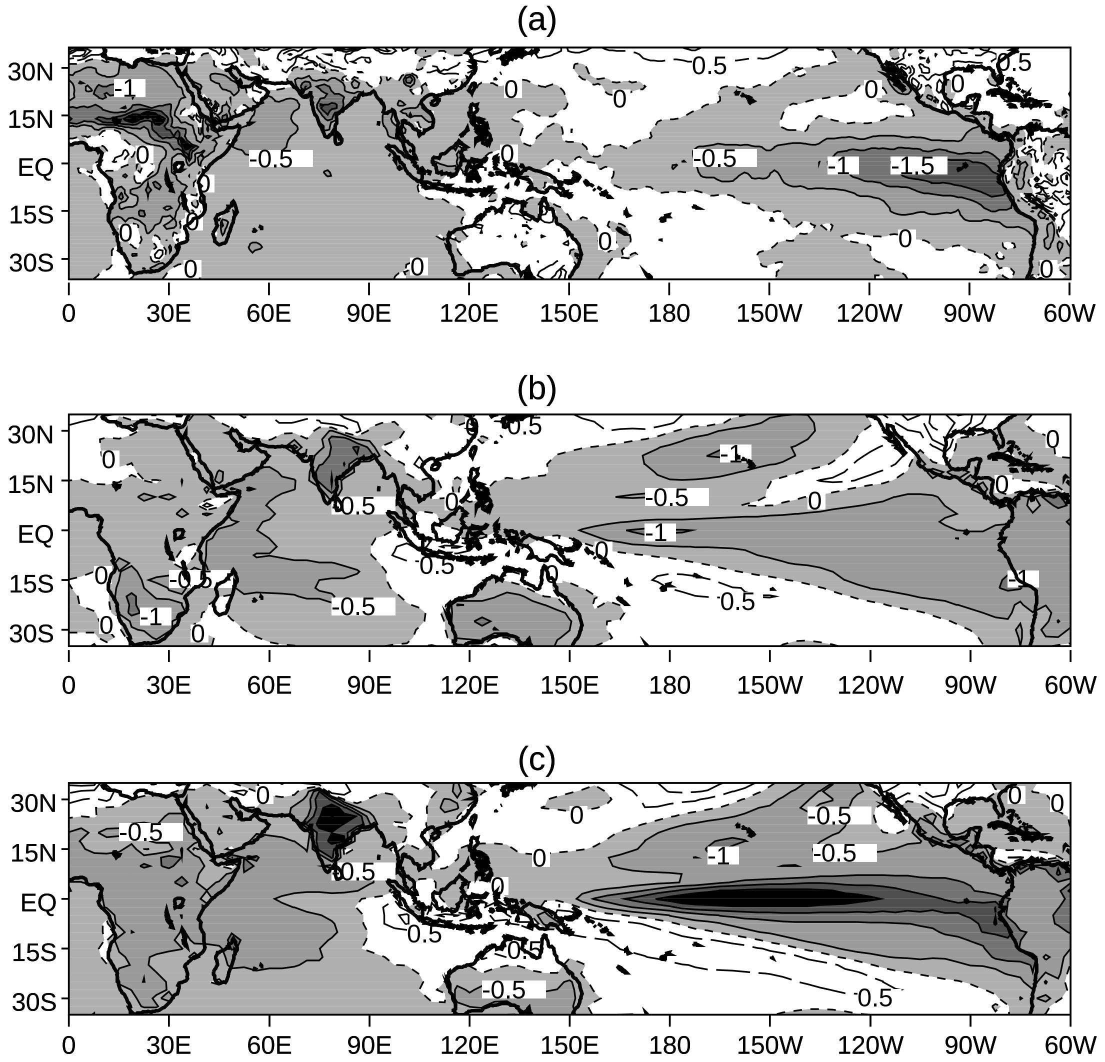

Figure 3.9: Strong minus weak summer (JJAS) composite difference plots of surface temperature (K) for (a) ERA-40, (b) HadCM3, and (c) HadCM3FA. Negative differences are shaded whilst dashed contours show positive differences. Contour interval is $0.5\mathrm{K}$.

Pacific, and the associated reduction in precipitation is also largely confined to the west of the date-line. The SST anomaly pattern associated with strong vs. weak monsoons in HadCM3 (Fig. 3.9b) shows only a weak association with ENSO, although the cooling of the Indian Ocean and subcontinent surface are reasonably well captured. The largest negative SST anomalies occur near the date-line rather than in the east Pacific, which, with the strengthened trades only over the west Pacific, may be associated with the warm pool confinement in HadCM3.

The flux adjustments in HadCM3FA have a significant effect on the interannual variability both of the monsoon and in the Pacific sector (Figs. 3.8c and 3.9c). Consistent with the increase in the standard deviation of the DMI in HadCM3FA, the strong minus weak monsoon differences are also larger than in HadCM3. However, there are also changes to the *patterns* of wind, precipitation and SST differences. The enhancement of the Pacific trades during strong monsoon years now extends further to the east, with the associated reduced precipitation anomaly also extending further across the Pacific, although the maximum precipitation anomaly is still near the date-line. The La Niña-like SST signal is much stronger in HadCM3FA than HadCM3, although it still extends too far to the west, and remains very equatorially confined. This stronger signal in equatorial SST indicates a potentially stronger teleconnection between ENSO and the monsoon in HadCM3FA, which will be investigated in subsequent sections. Over the Indian sector, the pattern of the strong minus weak signal in HadCM3FA is generally the same as HadCM3 but rather stronger, particularly the enhanced westerly flow near the equator. The rainfall signal over India itself is also stronger than in HadCM3, despite the weakened summer-mean Indian rainfall shown in Fig. 3.3. This suggests that stronger monsoon perturbations in HadCM3FA are due to stronger ENSO.

3.5 The impact of the basic state on ENSO variability

As Fig. 3.9 shows, the equatorial Pacific SST signal associated with interannual variability of the DMI is far stronger in the GCM when flux adjustments are applied, indicating that the teleconnection between ENSO and the monsoon is potentially much

Niño-3	HadCM3	HadCM3FA	ERA-40
$\bar{T}$	299.30	299.35	299.18
annual cycle σ	0.76	0.82	0.89
SST anomaly σ	0.94	1.21	0.85

Table 3.2: Mean temperature and variability of east Pacific SSTs. Standard deviations (σ) of the annual cycle and seasonally adjusted Niño-3 ($5°$N–$5°$S, 150–$90°$W) timeseries are shown. Units are K.

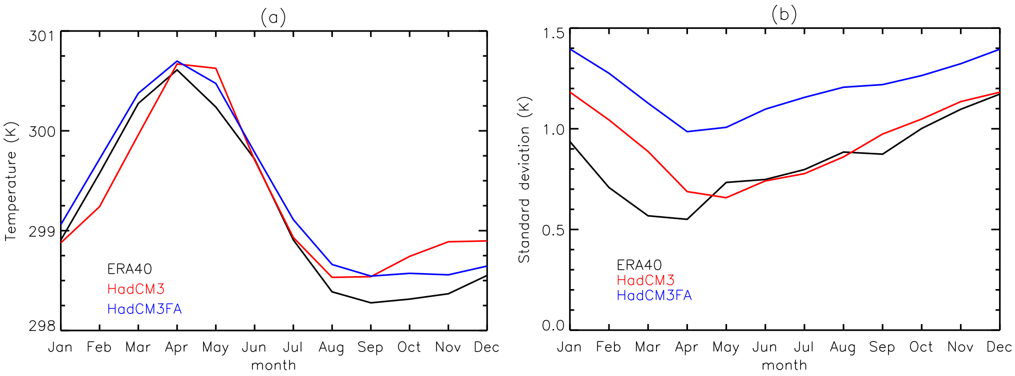

SST seasonal cycle

Cycle of interannual SST standard deviation

Figure 3.10: Niño-3 region SST behaviour for ERA-40, HadCM3, and HadCM3FA.

stronger in this version of the model. Before this teleconnection is investigated in more detail, the nature of ENSO itself in each of the model experiments needs to be evaluated. Standard deviations of the seasonally adjusted Niño-3 time series, (i.e. with the climatological cycle removed), are shown in Table 3.2 as a simple indicator of interannual variability. HadCM3FA has a larger standard deviation than HadCM3, which itself is slightly larger than the observed value.

The mean annual cycle of Niño-3 region SSTs provides a useful indication of the performance of a GCM in simulating equatorial Pacific SST. Figure 3.10a shows that the mean seasonal cycle of Niño-3 SSTs is well captured by both versions of the model. However, the use of flux adjustments to correct the mean state in the Indo-Pacific Warm Pool has had a significant impact on the interannual variability of the Niño-3 SSTs. Figure 3.10b shows the interannual standard deviation of Niño-3 SST anomalies for each month of the year. The standard deviation in all months is higher in HadCM3FA than HadCM3, further substantiating the enhanced SST variability in the adjusted model. The ERA-40 data indicate phase-locking of east Pacific SST variability to the annual cycle, with weakest variability in April and strongest in December, as found by, amongst others, Latif *et al.* (2001). In contrast, HadCM3 has its minimum variability slightly too late, in May, which is partially corrected in HadCM3FA. However, it is worth noting that both model versions perform well in their representation of the annual cycle of Niño-3 SSTs when compared with other coupled models studied by Latif *et al.* (2001). The seasonally adjusted Niño-3 timeseries for the ERA-40 dataset and the two model integrations are shown in Fig. 3.11. It is promising that in each of the model integrations shown in Fig. 3.11, El Niño seems to evolve in a very similar manner to those in ERA-40. Flux adjustments have not unduly upset the manner of the El Niño-La Niña oscillation, the only clear difference between them being the increased interannual variability in HadCM3FA.

Another impact of flux adjustment has been its effect on the periodicity and regularity of El Niño. Figure 3.12 shows the power spectra of seasonally adjusted Niño-3 region SST anomalies. In this figure the extended Hadley Centre observed SST dataset (HadISST, Rayner *et al.*, 2003) for the period 1900–1999 is used to give a comparable length of record to the model integrations. As noted by Guilyardi *et al.* (2004), the HadCM3 spectrum is strongly peaked at timescales between 3 and 4 years, indicating that ENSO in HadCM3 is too periodic. In HadCM3FA, variability at all time-periods is stronger, and there is a broader distribution of power across a range of frequencies. One explanation for the increased SST variability may lie in the warmer mean climate resulting from the flux adjustments. Codron *et al.* (2001), using a different coupled GCM, found that a warmer mean state in the Pacific caused interannual SST variability in the region to double. The current work confirms their results that the variability of tropical oceans is very sensitive to the mean state. The improved mean state has made the thermocline more intense (see §3.3), and Meehl *et al.* (2001) have argued that those models with a high ENSO amplitude share this characteristic. Interestingly, the power spectrum for HadCM3FA shows much increased power on biennial timescales, and this will be discussed in §3.6.

The trade wind response to Niño-3 SST variations gives a simple indication of

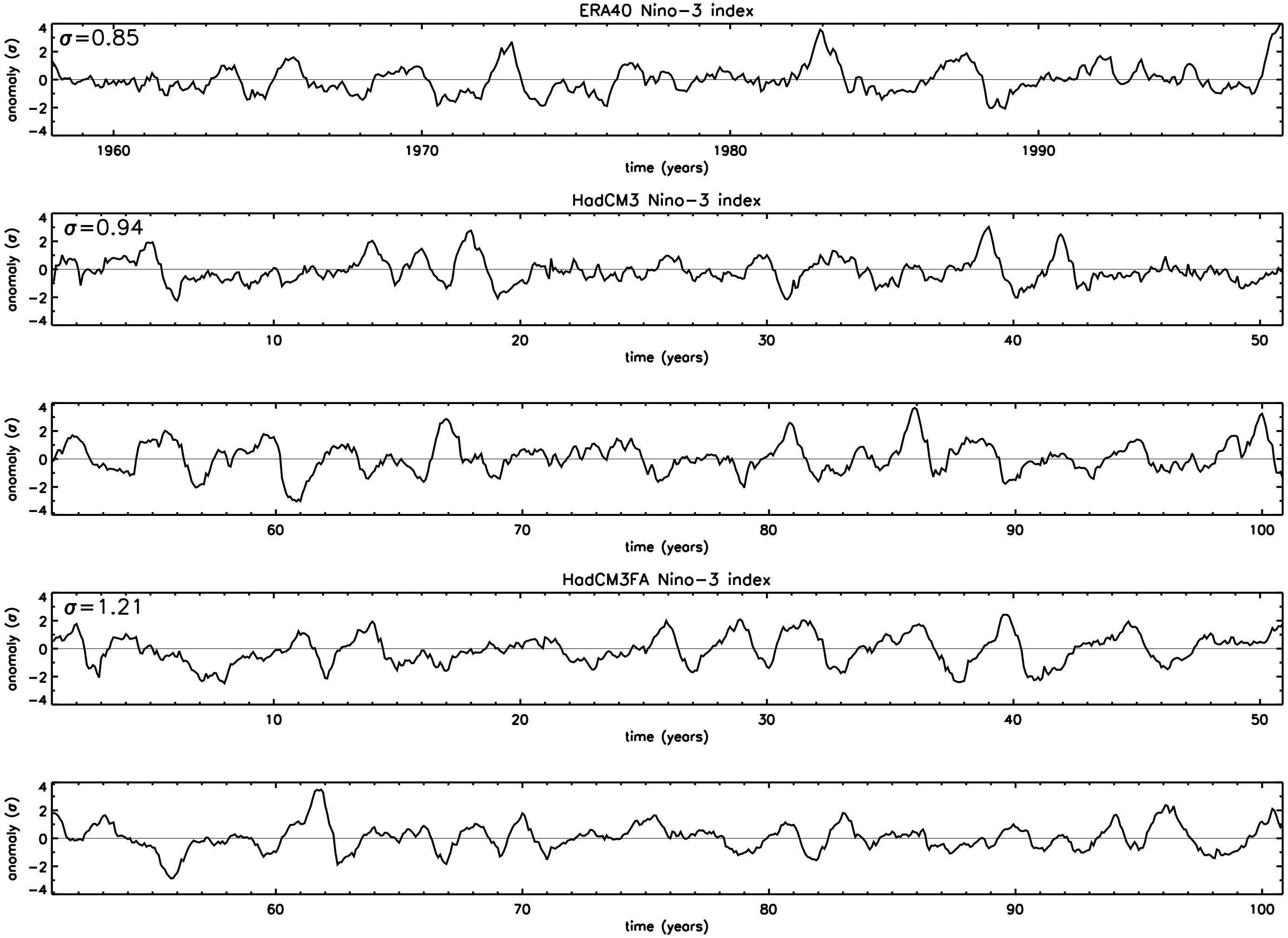

Figure 3.11: Timeseries of seasonally-adjusted Niño-3 SST anomalies in HadCM3 and HadCM3FA. Standard deviations of the anomalies are also shown (in K).

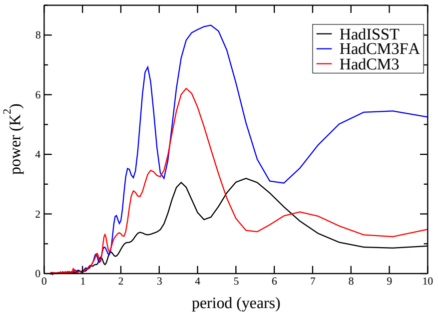

Figure 3.12: Power spectra of seasonally adjusted Niño-3 region SSTs in the 100-year HadISST dataset and the HadCM3 and HadCM3FA model integrations. Data are smoothed through a 20-year Tukey window.

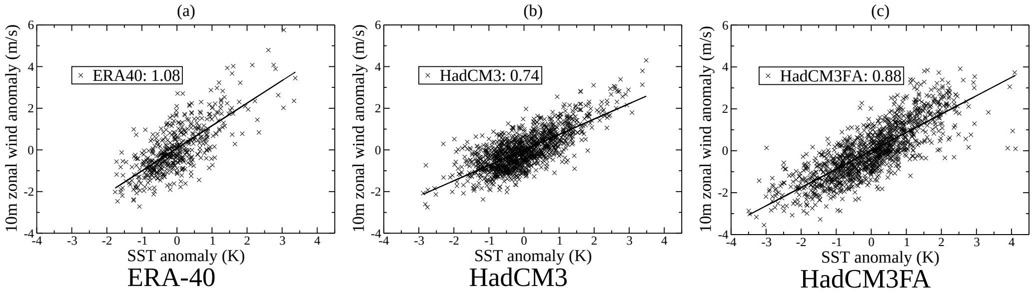

ERA-40 HadCM3 HadCM3FA

Figure 3.13: Monthly Niño-4 region $10\mathrm{m}$ zonal wind anomalies plotted against Niño-3 SST anomalies for the (a) ERA-40, (b) HadCM3 and (c) HadCM3FA. The coefficients shown are gradients of the best-fit lines, in units of $\mathrm{ms}^{-1}\mathrm{K}^{-1}$.

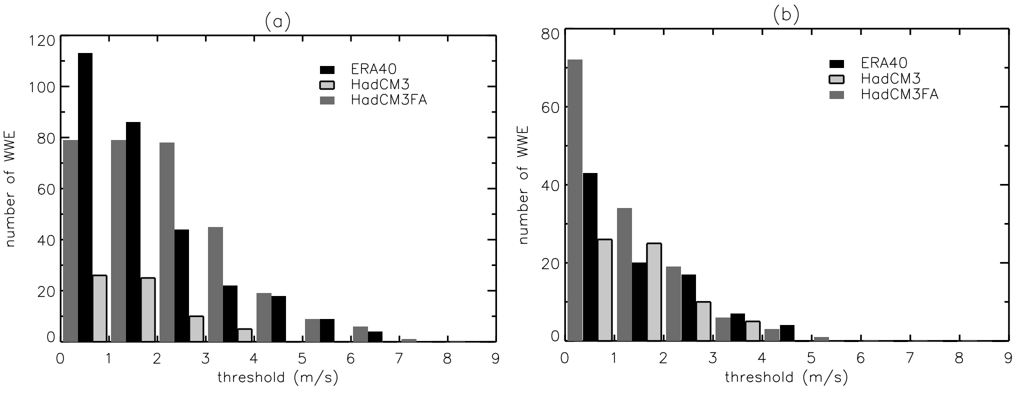

Westerly wind events

Mean-adjusted westerly wind events

Figure 3.14: Number of westerly wind events exceeding the given threshold which persist for longer than 5 days in daily data of 40 years of ERA-40, HadCM3, and HadCM3FA. Count made in the 148.175–$178.175°$E, $\pm1.25°$N region.

the coupling strength in a GCM. Figure 3.13 shows the relationship between zonal surface winds in the Niño-4 region ($160°$E–$150°$W) and the Niño-3 SST anomalies (150–$90°$W), computed from monthly mean data for each of the three datasets. The regression coefficients (gradient of the best-fit lines) are also shown. The distribution of Niño-3 SSTs in ERA-40 in Fig. 3.13a shows more frequent but minor cool events (La Niña), together with fewer but stronger east Pacific warmings (El Niño), whereas the two versions of the model tend towards a normal distribution, only slightly biased to a greater number of cold events (Figs. 3.13b,c). When considering the ocean-atmosphere coupling, it is clear that the variability of central Pacific trade winds in HadCM3FA is more closely coupled to Niño-3 SST variability than in HadCM3, although neither model version reproduces the observed strength of this relationship. This suggests that the surface winds in HadCM3FA can respond more realistically to east Pacific SST variations once some of the systematic biases have been removed. The more intense thermocline found in the flux adjusted model allows equatorial upwelling to tap into sub-thermocline waters more readily when a given wind variation is applied.

Lengaigne *et al.* (2004) describe how a single strong equatorial west Pacific westerly wind event (WWE), applied to a coupled ocean-atmosphere model, was able to excite an El Niño in part through the generation of a downwelling Kelvin wave that propagates eastward, causing SST anomalies in the east Pacific. In addition, the WWE caused an eastwards extension of the Warm Pool, thus allowing convection and subsequent WWEs to extend further into the Pacific, reinforcing the developing El Niño. Their results suggest that stochastic forcing can broaden the spectrum of Niño-3 SST variability, moving the ENSO cycle away from a slowly evolving, rather predictable oscillation. Although a detailed study of the ENSO dynamics in HadCM3 is beyond the scope of this study, the occurrence of WWEs in the two model versions has been analysed. Figure 3.14a shows the number of WWEs of varying strengths that persist for longer than 5 days in ERA-40 and in the HadCM3 and HadCM3FA models. Flux adjustment removes some of the easterly bias inherent in HadCM3, so thresholds have been adjusted in Fig. 3.14b to take account of the mean zonal wind strength in the west Pacific in the different GCM versions. The figures show more and stronger WWEs in the flux-adjusted model, consistent with improved simulation of the Madden-Julian Oscillation (MJO), as found by Inness *et al.* (2003). The greater stochastic forcing on intraseasonal timescales in HadCM3FA may contribute to the less regular ENSO cycle, already noted in Fig. 3.12.

The different nature of ENSO in HadCM3FA will obviously have a global impact through remote teleconnections. The influence of ENSO on global SST can be seen by correlating Niño-3 temperatures with global surface temperatures, as in Fig. 3.15. In ERA-40 strong positive correlations extend broadly over the east Pacific, with a horseshoe pattern of negative correlations around this region. The positive correlations over the Indian Ocean indicate the result of atmospheric teleconnections with El Niño (see, $e.g.$ Spencer *et al.*, 2005). HadCM3 captures the main features of this pattern but with some differences. The positive correlations in the equatorial Pacific extend too far west, splitting the horseshoe pattern of negative correlations into two branches. In the east Pacific, the pattern is rather meridionally confined, a feature common to many coupled models. With flux adjustment, there is some improvement in the pattern of correlations over the Pacific although the Indian Ocean teleconnection has become consistently stronger, indicating that ENSO now has a greater bearing on behaviour in the Indian sector, as evident also in Fig. 3.9. The strong link between the Pacific and

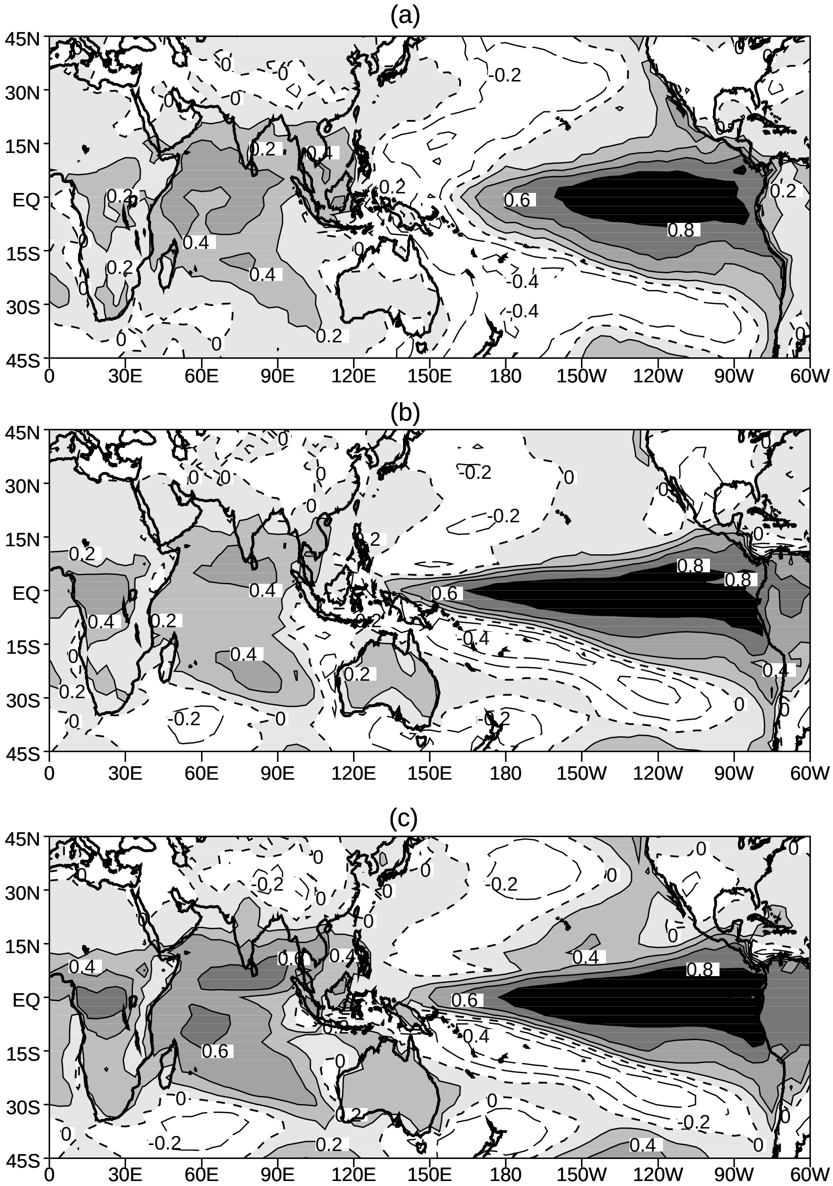

Figure 3.15: Concurrent correlations between Niño-3 and global SSTs in (a) ERA-40, (b) HadCM3, (c) HadCM3FA. Positive correlation regions are shaded whilst dashed lines show negative correlations. Contour interval 0.2. Correlations are significant in all but 5% of cases outside ± 0.2 for the 100 year model runs and ± 0.31 for ERA-40.

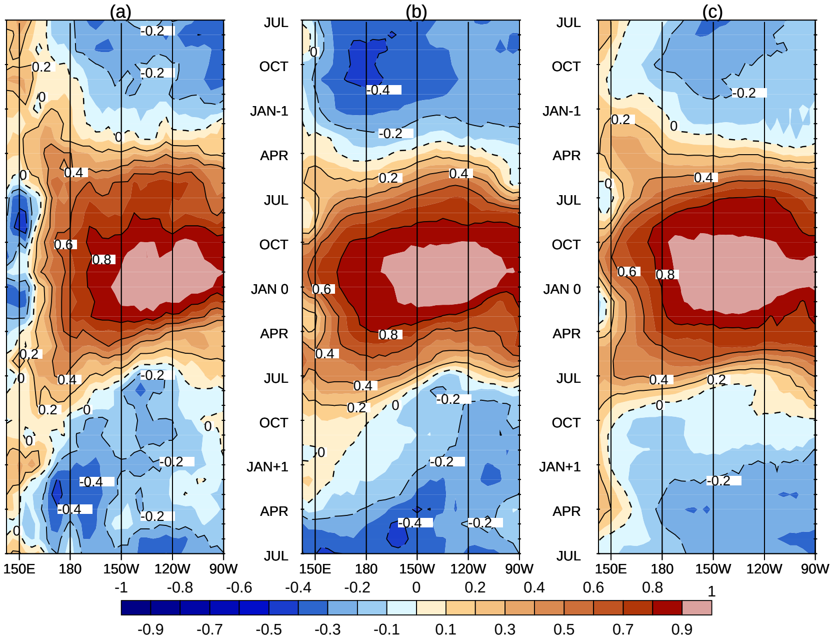

Figure 3.16: Lag correlations between winter season (DJF) Niño-3 SSTs and monthly equatorial Pacific (2.5°N–2.5°S) SSTs in (a) ERA-40, (b) HadCM3, (c) HadCM3FA. Negative correlation contours are dashed. Significance levels are as in Fig. 3.15.

Indian sectors in HadCM3FA is consistent with a TBO system described by Meehl and Arblaster (2002b, 2002a) and Meehl *et al.* (2003).

El Niño evolution can be described by lag-lead correlations of Niño-3 SSTs with SSTs across the whole of the equatorial Pacific. Figure 3.16 shows the correlations between winter season (DJF) Niño-3 SSTs and monthly-meaned equatorial (2.5°N–2.5°S) Pacific SSTs for the 18 months preceding and following the peak of El Niño. The correlations with the ERA-40 data indicate that El Niño is associated with warming across the central and east Pacific, as well as cooling of the west Pacific warm pool as the thermocline deepens in the east and rises in the west. In the winter and spring before the peak of El Niño, a lobe of positive correlations is seen in the region 150–180°E, representing pre-El Niño extension of the warm pool, often associated with anomalous westerlies (see, $e.g.$, Lengaigne *et al.*, 2002). As already noted in Fig. 3.15b, El Niño extends too far west in HadCM3, and the confinement of the warm pool means that the negative correlations at 140°E are limited when compared to observations. In addition, there is no proper representation of the pre-El Niño warm pool extension, potentially

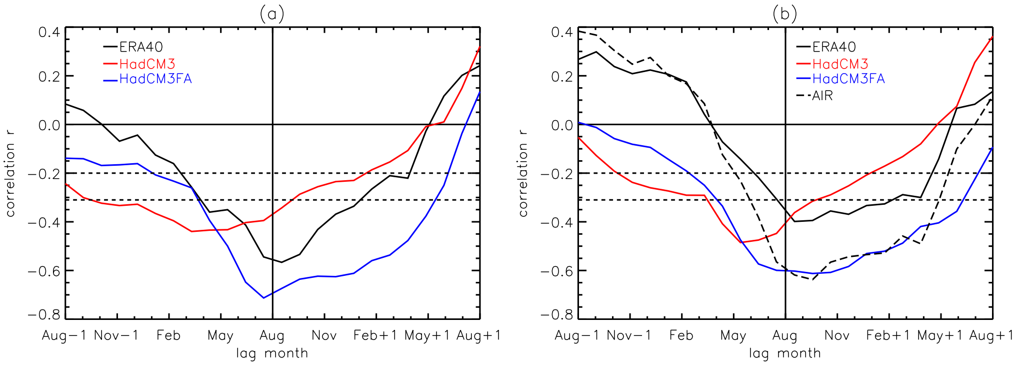

Nino-3 SST vs. DMI

Nino-3 SST vs. Indian Rainfall

Figure 3.17: Correlation between Niño-3 and summer (JJAS) (a) DMI or (b) Indian rainfall plotted against lag time. In (b), AIR refers to the All-India Rainfall precipitation data being correlated with ERA-40 SSTs. 'Aug-1' indicates the August Niño-3 anomaly the year before the measured rainfall. Correlations significant in all but 5% of cases are indicated outside the dashed lines: $|r| > 0.31$ for the 40 year datasets, $|r| > 0.20$ for the 100 years datasets.

an important part of the evolution of ENSO. The negative correlations before and after El Niño are also too strong, in part because El Niño in HadCM3 is too regular, with a periodicity in the region of 36 months. This regularity was also noted in the CNRM coupled model by Ashrit *et al.* (2003).

Flux adjustments lead to some improvements in the evolution of El Niño. There is now some evidence, albeit weak, of negative correlations in the west Pacific. The presence of a positive lobe in spring between $150°$E and $180°$E in Fig. 3.16c shows that HadCM3FA is reproducing the pre-El Niño warm pool extension, consistent with the increased westerly wind activity shown in Fig. 3.14. The negative correlations in the boreal summers are less pronounced in HadCM3FA, indicating again that ENSO is less periodic in its strongest mode, supporting Fig. 3.12.

3.6 The basic state and monsoon-ENSO teleconnections

The monsoon-ENSO teleconnection is arguably the strongest link between the Asian summer monsoon and other global phenomena, and has been studied as far back as the 1920s by Gilbert Walker ($e.g.$, Webster and Yang, 1992). In coupled models used for seasonal prediction of the monsoon, it is therefore important that the Pacific SSTs are well simulated, and also that the signal from the equatorial Pacific is correctly transmitted to the monsoon region.

It was shown in §3.4 that there is a stronger Pacific SST signal during anomalous monsoon years when flux adjustments are applied to HadCM3, suggesting a stronger teleconnection, and in §3.5 that the interannual Niño-3 variability is stronger and less regular in HadCM3FA than the standard version of the GCM. The monsoon-ENSO teleconnection will now be examined in more detail. Figure 3.17 shows the correlation between the monthly Niño-3 time series (through the whole year) and indices of the strength of the summer monsoon. Considering first the large-scale monsoon variability, represented by the DMI, Fig. 3.17a shows that in ERA-40, the strongest inverse correlation occurs in the middle of the monsoon season, between July and August. Thus high boreal summer surface temperatures in the Niño-3 region (El Niño) correlate well with dynamically weak monsoons in agreement with many other studies ($e.g.$, Shukla and Paolino, 1983; Webster and Yang, 1992). Prior to the monsoon the negative correlations only become significant during March-April, a manifestation of the predictability barrier first suggested by Webster and Yang (1992), in which equatorial Pacific SST conditions prior to April are of little use in summer monsoon prediction. Furthermore, the ERA-40 results show slightly larger negative correlations after the monsoon than before, suggesting that the monsoon leads El Niño.

HadCM3 does not represent the timing of the teleconnection correctly, instead finding May Niño-3 SSTs to be most strongly correlated with monsoon strength (Fig. 3.17a). The shape of the correlation curve is also incorrect, with no obvious spring predictability barrier; instead the negative correlations are significant from the preceding autumn. Also the lag correlations after the monsoon are insignificant, suggesting that in HadCM3 the monsoon has little influence on El Niño. Thus HadCM3 is not correctly reproducing the monsoon-ENSO teleconnection, even though the mean monsoon is quite well simulated. By correcting the systematic errors in the Indo-Pacific region, the teleconnections between the monsoon and ENSO are dramatically improved in HadCM3FA. The maximum negative correlation now occurs in summer although its strength supports the result that ENSO plays a more dominant role in monsoon behaviour than before. The spring predictability barrier is also simulated in HadCM3FA, with the negative correlation being insignificant until March preceding the monsoon. The asymmetry in the lead-lag correlations is even more pronounced in HadCM3FA than in ERA-40, suggesting that the monsoon has a significant influence on the evolution of El Niño. Hence in HadCM3FA the monsoon could be regarded as becoming, ‘more active in world weather’, to paraphrase Normand (1953).

Looking back at the Pacific SST power spectra in Fig. 3.12, increased power is found at quasi-biennial timescales in HadCM3FA. Kim and Lau (2001) found the key to quasi-biennial tendency in El Niño evolution to lie in the strong coupling of ENSO to monsoon wind forcing in the west Pacific. Manually increasing this coupling in their simplified GCM made the ENSO system more biennial, and in our study Fig. 3.17a has indicated the strengthened monsoon-ENSO relationship in HadCM3FA. Lau and Wu (2001) noted some observational evidence for strong monsoon-ENSO interactions during El Niño events with a strong biennial tendency, whilst Wu and Kirtman (2004) found that a strong biennial tendency was possibly due to the strong monsoon-ENSO interaction in their model. However, they concede that systematic model bias may also be the cause, illustrating the difficulty in drawing such conclusions in coupled model experiments.

So far the monsoon-ENSO teleconnection has been described in terms of the dynamical monsoon index (DMI). It might be argued that a more localized index such as All-India Rainfall is more relevant to the seasonal forecasting issue. Fig. 3.17b also shows lag-lead correlations with east Pacific (Niño-3) SSTs, but this time with seasonal (JJAS) All-India Rainfall from Parthasarathy *et al.* (1994). The grid squares chosen for the Indian region in the models were as in Gadgil and Sajani (1998). ERA-40 rainfall data were interpolated onto the model grid, allowing the same squares to be selected. The results show that only with flux adjustment is the model able to capture the seasonality of the teleconnections between the monsoon and ENSO. Again the asymmetry in the lead-lag correlations support the role of the monsoon as an active rather than passive player in El Niño, and that it is only HadCM3FA that is able to capture that role.

used with reasonable success since 2003.

Whilst making predictions of future monsoon behaviour is a key goal of climate change research, the answers are not always in agreement. May (2004) cites a number of different studies which give no overall indication of how the Asian summer monsoon will respond to increased greenhouse forcing. Ashrit *et al.* (2003) identify several large uncertainties, all of which contribute to the spread in prediction: the different emission scenarios used; whether or not to include sulphate aerosol forcing; the variety of theories covering multidecadal internal variability, and model differences contributing to discrepancies in current monsoon simulation. As Federov and Philander (2000) note, an essential debate about changes to El Niño is deciding on the realities of decadal fluctuations, which lack any obvious physical cause.

This study particularly relates to uncertainties in the mean climate representation in GCMs and its effect on monsoon prediction through variability and teleconnections. Meehl *et al.* (2000), for example, compare two NCAR coupled GCMs and suggest that as the control integrations feature different systematic errors, then the climate change responses are not likely to be comparable. Just as Sperber and Palmer (1996) noted the link between correct simulation of the climatological basic state in the tropics and accurate seasonal prediction of precipitation variability, Federov and Philander (2000) realised that such errors could have an enormous effect on future predictions. Trying to calculate how global warming will alter the basic state and thus influence El Niño and the monsoon will therefore have large uncertainties.

Two further 100-year integrations of the Met Office Unified Model HadCM3 are analysed in this chapter. These represent stable future climate conditions ($2 \times \mathrm{CO}_2$) in both the standard version of the model and the limited area flux corrected version (HadCM3FA) introduced in chapter 3. The method is outlined in §4.2. §4.3 looks at the effect of climate change on the mean state, whilst §4.4 addresses changes to monsoon variability. These are related to ENSO changes in §4.5, whilst the predictability of the monsoon via its teleconnection with ENSO is considered in §4.6. Conclusions are drawn in §4.7.

4.2 The climate change integrations

This chapter uses results from both the HadCM3 and HadCM3FA versions of the Unified Model under doubled carbon dioxide conditions. A vertical resolution of $\mathrm{L}30$ is used, as in chapter 3.

The HadCM3 $2 \times \mathrm{CO}_2$ experiment was initialised from an existing 150-year $2 \times \mathrm{CO}_2$ Hadley Centre run, previous to which the carbon dioxide had been ramped up at a rate of 1% per year for 70 years.[1] A further period of 10 years was discarded, allowed as a cautious spin-up to 30 vertical levels in the atmosphere, as in the chapter 3 integrations. This experiment is designed to look at the effect of climate change on the monsoon climate, the ENSO system and the teleconnection between them. That the integration is non-transient ($i.e.$, greenhouse forcing is fixed) allows the monsoon-ENSO system to be studied in detail, undergoing no varying external forcing.

Clearly, if HadCM3 features systematic errors under a twentieth century forcing scenario then these errors will also be present under future greenhouse forcing conditions. Making the assumption that the errors will be of the same magnitude under future conditions, the same heat flux adjustments are applied to an integration initiated in the future climate (after the 10 year spin-up to $\mathrm{L}30$). Although the non-linearity of the modelled coupled atmosphere-ocean system makes it unlikely that the basic state errors would be of equal magnitude, previous greenhouse forcing experiments with older coupled GCMs used the same seasonal cycle of anomalous fluxes ($e.g.$, Collins, 2000a, using HadCM2) as in their current climate. In any case, the application of this system of flux correction to a future climate will serve as a useful experiment, and verification of conclusions already drawn in Turner *et al.* (2005) and chapter 3.

Adding heat fluxes to an already warmer Pacific Ocean proves challenging for the model code and in the first instance, numerical instabilities build up after a period of 35 years. Restarting the model integration at this stage simply reproduces the exact conditions, hence an alternative approach is required. Slightly different initial conditions are generated by offsetting the ocean and atmosphere start dumps by an arbitrary period,

---

[1] Atmosphere and ocean start dumps were provided by Jason Lowe of the Hadley Centre.

in much the same way as ensemble members of weather forecasts could be generated. The ocean dump was the most recent calendar year start before the crash (1 January 2555) whilst the atmosphere was initialised exactly 5 years earlier (1 January 2550). A successful 100 year integration then follows, of which the first five years are discarded, allowing the coupled system to adjust to the start dump mismatch.

Neither integration takes account of sulphate aerosol forcing, which may act to counter some of the effects of carbon dioxide, as noted by Ashrit *et al.* (2003).

4.3 The influence of climate change on the GCM basic state

Figure 4.1 shows the effect of climate change (doubling CO_2 concentration) on the mean summer climates of HadCM3. Firstly considering surface temperatures (Fig. 4.1a,d), it is clear that warming has taken place across the whole of the Indo-Pacific sector. Land regions have warmed by a greater degree than the sea due to the large heat capacity of water. Hence relatively more warming occurs in the northern hemisphere, as noted in the IS92a simulation of Timmermann *et al.* (2004). There is also evidence of an *El Niño-like warming* in the equatorial Pacific Ocean, $i.e.$, the east has warmed more than the west ($1.5 - 2°\mathrm{C}$ in places, compared to more than $1°\mathrm{C}$ in the west). This pattern of warming in the mean climate amounts to a reduction in the zonal equatorial temperature gradient, and may lead to some monsoonal changes. Meehl *et al.* (2000) compared two NCAR coupled GCMs under 1% per year increasing CO_2, and noted that the model with El Niño-like warming saw a suppressed increase of rainfall in Southeast Asia *relative* to the other. Timmermann *et al.* (1999) noted an El Niño-like warming in their transient climate change integration, as did Ashrit *et al.* (2003) who noticed it more so in summer. It is interesting to note that in their review of the CMIP[2] integrations, Collins and The CMIP Modelling Groups (2005) found the most likely scenario was one of no El Niño- (or La Niña-) like climate change. Indeed

---

[2] Coupled Model Inter-comparison Project

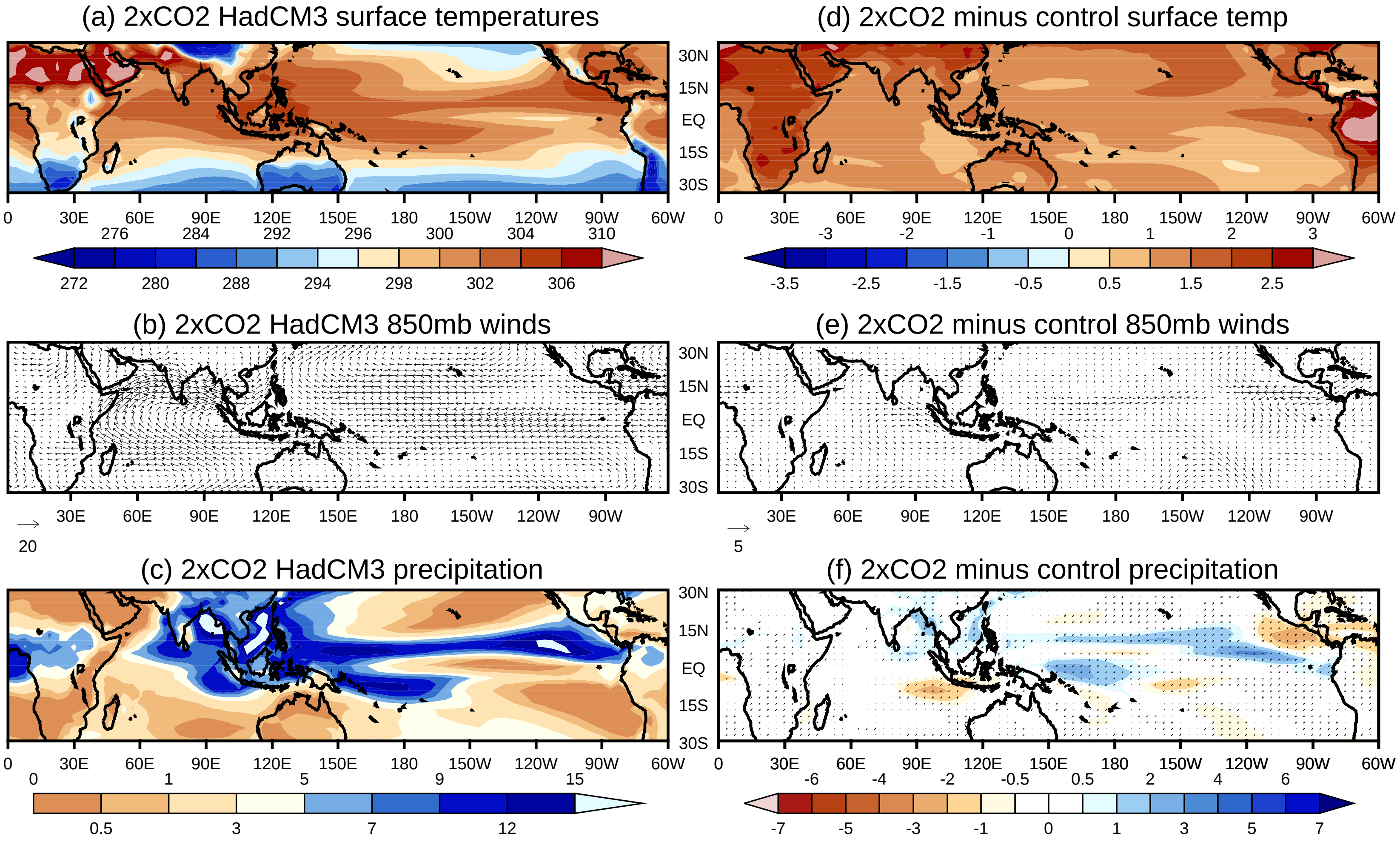

Figure 4.1: HadCM3 $2 \times CO_2$ summer (JJAS) climatologies of (a) surface temperature (K), (b) $850\mathrm{hPa}$ winds (ms^{-1}) and (c) precipitation ($\mathrm{mm.day}^{-1}$). Panels (d) to (f) show differences in these fields from HadCM3 under pre-industrial conditions. Unit wind vectors are $20\mathrm{ms}^{-1}$ (climate) and $5\mathrm{ms}^{-1}$ (anomaly). Speckling on the precipitation difference (f) indicates significance at the 95% level using a student t-test.

those models with the largest El Niño-like warming in future climate scenarios were those which performed least well at simulating present day ENSO variability. This finding allows climate change predictions using a variety of models to be weighted in favour of those which perform best. However, by artificially tuning the scientific parameters of HadCM3 to better represent ENSO, future El Niño warming in the mean was found to increase (Matt Collins, *personal communication*, September 2005).

The differential in surface warming between the land and sea has led to an *increase* in the land-sea meridional gradient of temperature in the Indian region. This may act to strengthen the monsoon dynamics, as argued by Hu *et al.* (2000) who found enhanced moisture convergence over land under such conditions. Meehl and Arblaster (2003) however, found the effects of varying local and remote SST forcing under climate change to be of greater consequence for the monsoon than the land-sea contrast.

Looking at the lower tropospheric winds ($850\mathrm{hPa}$) in Figs. 4.1b,e, it is clear that increased greenhouse forcing has affected the mean winds in only a few localities. The Pacific trade winds at about $5°\mathrm{N}$ are approximately $1\mathrm{ms}^{-1}$ weaker in the region $150°\mathrm{E} - 150°\mathrm{W}$, likely as a result of the El Niño-like surface warming. Over the Indian Ocean, the flow at lower levels is more easterly just west of Sumatra, $i.e.$ weaker in its final push across the south Bay of Bengal. It is difficult to relate this weakening to El Niño-like warming in the Pacific given that the flow is actually stronger by almost $1\mathrm{ms}^{-1}$ in the northern Arabian Sea and then on over the north of India. This amounts to a slight northward shift of the monsoon flow structure, which May (2004) attributes to the increased meridional heating gradient in his ECHAM4 AGCM (T106) study. Using the CNRM coupled model, Ashrit *et al.* (2003) note a slight northward shift but with no overall magnitude trend in transient simulations of the late twenty-first century. In transient runs of the MRI globally flux-corrected coupled GCM, Kitoh *et al.* (1997) note a decrease in $850\mathrm{hPa}$ winds over the Arabian Sea and an increase from the Sahel region to northwest India. This northward motion of the monsoon jet acts to decrease the zonal wind shear index (DMI) as measured in the region stated in chapter 3.

The anomalous easterlies out of Sumatra are part of a small anomalous anticyclone in the southern hemisphere, leading to a drier precipitation climate there (up to

$3\mathrm{mm.day}^{-1}$ in Fig. 4.1f). Significant increases (at the 95% level using a student t-test) in daily precipitation are noted in the main summer ITCZ and SPCZ bands across the Pacific Ocean. The ITCZ is wetter by $2\mathrm{mm.day}^{-1}$ right across the Pacific basin, with up to $5\mathrm{mm.day}^{-1}$ extra at $120°\mathrm{W}$. The visible northward displacement of the ITCZ is related to the preferential warming of the northern hemisphere (greater land mass), displacing the 'thermal equator' in HadCM3 (Johns *et al.*, 2003). The SPCZ east of New Guinea is wetter by more than $2\mathrm{mm.day}^{-1}$. Now considering the effect of increased greenhouse forcing on the Asian summer monsoon, it is clear that daily precipitation during the summer season increases by between $0.5\mathrm{mm.day}^{-1}$ in the northern states and at the tip of peninsula India, and $2\mathrm{mm.day}^{-1}$ in the north-eastern Bay of Bengal, Bangladesh and Myanmar. The South China Sea off Hong Kong and Vietnam also sees significant increases of this magnitude. HadCM3 $2 \times \mathrm{CO}_2$ compares well with other studies. Kitoh *et al.* (1997) note significant extra rainfall over India with their coupled MRI model, whilst Hu *et al.* (2000) see enhanced precipitation over the Indian peninsula. In their transient run of the late twenty-first century, Ashrit *et al.* (2003) see significant increases over northwest India and the far south, despite a weakened flow there. In a time-slice coupled experiment at $2 \times \mathrm{CO}_2$, May (2004) sees an overall intensification of the summer precipitation pattern, increasing along the Indian west coast, north Bay of Bengal and Bangladesh, whilst drying in the northern peninsula and the adjoining Bay of Bengal where the flow has decreased.

The overall pattern of precipitation increase is similar to that found by Meehl and Arblaster (2003) using the Parallel Coupled Model (PCM), although they found no drying south-west of Sumatra. Rather than the increased meridional temperature gradient, they attribute the increase in mean south Asian monsoon rainfall to the warmer Indian Ocean providing increased moisture, as in an earlier study by Meehl *et al.* (2000). Enhanced moisture convergence is also cited as the principal mechanism providing increased precipitation by Kitoh *et al.* (1997) and Ashrit *et al.* (2003). Using SRES[3] transient simulations in HadCM3, Johns *et al.* (2003) also note significantly wetter conditions for South Asia during summer.

---

[3] Special Report on Emission Scenarios for the IPCC Third Assessment Report: A1F1, A2, B1, B2.

It is interesting to look at the effect of climate change on regions further afield, such as the Amazon basin. The El Niño-like warming observed in the Pacific Ocean (Fig. 4.1b) is related to large precipitation decreases over the Amazon by Betts *et al.* (2004). They used a fully-interactive vegetation model as part of HadCM3 and found that this served only to increase the drying as part of a positive feedback mechanism. The positive feedback led to dieback of the forested region, a potentially disastrous consequence for the global carbon cycle. Alternatively, using a fully-coupled carbon cycle, Cox *et al.* (2004) demonstrated an increase in atmospheric $\mathrm{CO_2}$ concentration concurrent with a decrease in the uptake of carbon by the land surface and the amounts held in both vegetation and soil. The inclusion of an interactive carbon cycle acts to accelerate climate change, eventually changing the terrestrial biosphere to an overall source of carbon, according to Cox *et al.* (2000). In Fig. 4.1f the Amazon drying response is clear in this version of the model, together with a high degree of surface warming (Fig. 4.1b), despite lacking the interactive vegetation. Thus forest dieback cannot be ruled out, and further additions to the model physics with vegetation and carbon-cycle schemes can only enhance this feedback.

Now we come to consider the effect of a climate change scenario in the flux adjusted version of the model. Figure 4.2 is as Fig. 4.1, but showing the mean summer climate of the HadCM3FA $2 \times \mathrm{CO_2}$ integration (a-c) and its differences with HadCM3FA $1 \times \mathrm{CO_2}$ (d-f). Looking at the summer (JJAS) surface temperature difference in Fig. 4.2d, it is clear that the flux corrected version of the model shows a similar response pattern to the standard model, with increased warming over land regions and preferential response in the east Pacific, reducing the east-west SST gradient in the equatorial waters. Warming reaches as much as $2.5°\mathrm{C}$ in the far-eastern Pacific, while the Amazon region in South America is warmed in excess of $3°\mathrm{C}$.

The surface wind response shown in Fig. 4.2e indicates a more marked pattern of change in the Indian monsoon region than in HadCM3 (Fig. 4.1e), with the increase in the low-level flow in the northern Arabian Sea more obvious. There is increased convergence at $850\mathrm{hPa}$ in the warmer eastern equatorial Pacific, which aids the increased precipitation along the ITCZ noted in Fig. 4.2f. The magnitude of rainfall increase in

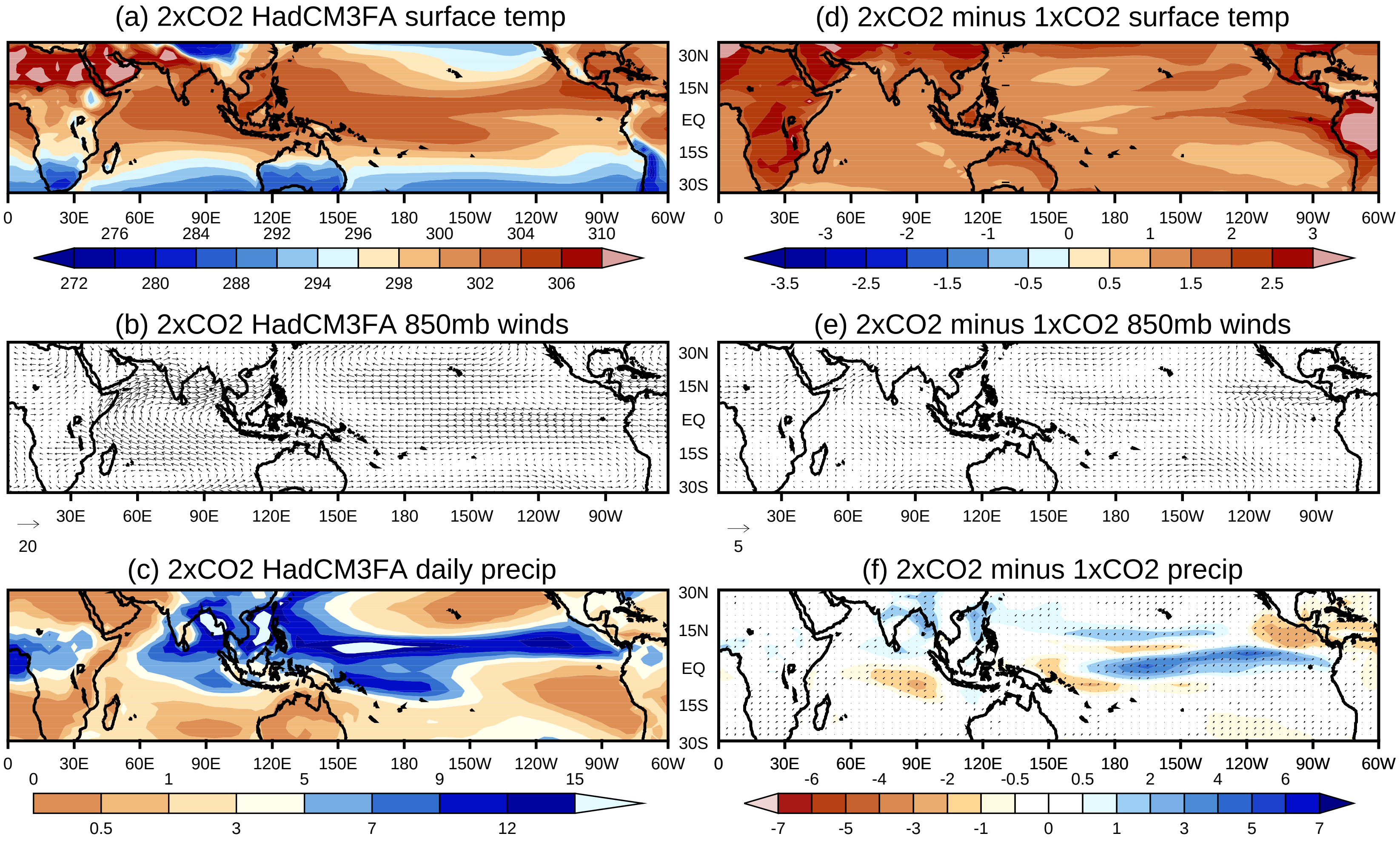

Figure 4.2: HadCM3FA $2 \times \text{CO}_2$ summer (JJAS) climatologies of (a) surface temperature (K), (b) 850hPa winds (ms^{-1}), and (c) precipitation (mm.day^{-1}). Panels (d) to (f) show differences in these fields from HadCM3FA under pre-industrial conditions. Unit wind vectors are 20ms^{-1} (climate) and 5ms^{-1} (anomaly). Speckling on the precipitation difference (f) indicates significance at the 95% level using a student t-test.

the tropical convergence zone of the Pacific is much larger with flux adjustments, reaching almost $5\mathrm{mm.day}^{-1}$ with climate change. The region of drying in HadCM3 west of Sumatra (Fig. 4.1f) is slightly larger and farther west, likely related to the stronger anticyclone there. As far as the Indian monsoon is concerned, the same response pattern is represented in both versions of the model, although here it is much stronger, especially in the north of India, the north Bay of Bengal, Bangladesh and south central China.

The patterns of change are very similar in all three fields shown in Figs. 4.1 and 4.2, although the flux adjusted version seems to have a greater response to climate change than the standard model. The major *difference* lies in the precipitation response, where the standard model (Fig. 4.1f) shows a wetter ITCZ and SPCZ, whereas HadCM3FA (Fig. 4.2) indicates increased precipitation in a band from the SPCZ in the west across to the central ITCZ, and further increases in a band in the central Pacific north of the equator. This relates to the spatial pattern of applied flux adjustments.

It is therefore possible that due to its systematic errors in the tropical oceans, HadCM3 may be underestimating the change due to increased greenhouse gas forcing. These errors in the basic state would propagate through to the interannual variability as described in chapter 3, and thus have a negative impact on the predictability of monsoon systems in the future climate.

One can also consider the effect of flux adjustments alone during a future climate scenario. Figure 4.3 shows the summer response to flux correction in (a) surface temperature, (b) $850\mathrm{hPa}$ winds and (c) daily precipitation. The surface temperature response is very similar, as one would expect, to that shown in Fig. 3.3, reflecting the identical application of flux corrections. The wind response is also similar (Fig. 4.3b), although the reduction in the monsoon jet over the Arabian Sea is less obvious. This is likely because the temperature changes induced by the anomalous fluxes are taking place against a warmer background state ($2\times\mathrm{CO}_2$) than in chapter 3 ($1\times\mathrm{CO}_2$), so their influence on the absolute meridional temperature gradient will be less noticeable. The pattern of precipitation response is almost identical to that under $1\times\mathrm{CO}_2$ conditions, (Fig 3.3f).

Now that both future-climate versions of the model have been introduced, we can

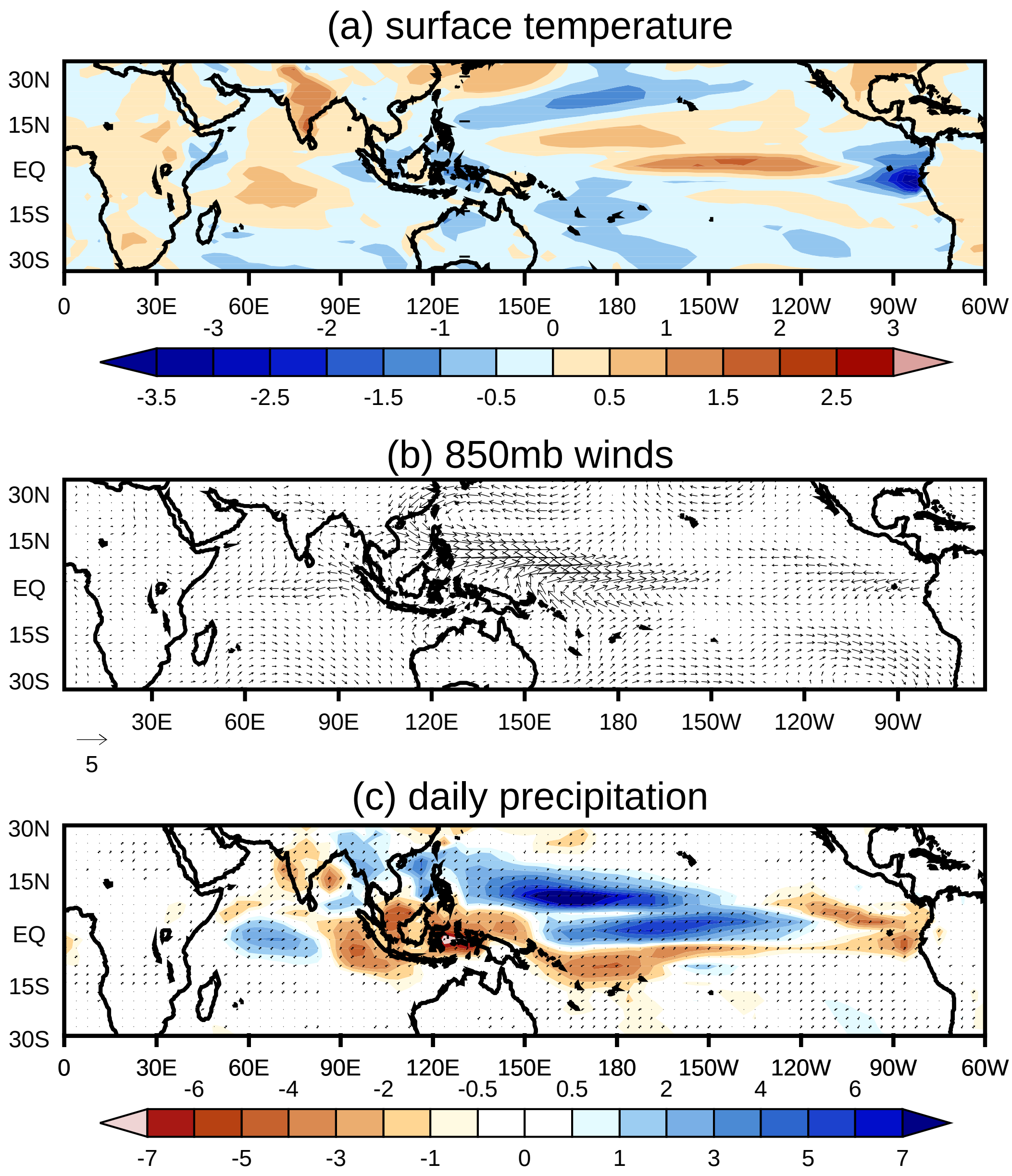

Figure 4.3: Response of the mean summer (JJAS) climate to flux adjustments at 2 × CO$_2$ for (a) surface temperature (K), (b) 850hPa winds (ms^{-1}) and (c) precipitation ($\mathrm{mm.day}^{-1}$). Unit wind vector is $5\mathrm{ms}^{-1}$. Speckling on the precipitation difference (c) indicates significance at the 95% level using a student t-test.

(a) Indian land surface

CO_2	HadCM3	HadCM3FA	$\Delta rain_{\mathrm{FA}}$
$1 \times CO_2$	4.29	3.41	-20.5%
$2 \times CO_2$	4.44	3.84	-13.5%
$\Delta rain_{CO_2}$	$+3.5\%$	$+12.7\%$	-

(b) $5 - 40°$N, $60 - 100°$E

CO_2	HadCM3	HadCM3FA	$\Delta rain_{\mathrm{FA}}$
$1 \times CO_2$	5.17	4.76	-7.9%
$2 \times CO_2$	5.44	5.17	-4.9%
$\Delta rain_{CO_2}$	$+5.2\%$	$+8.5\%$	-

Table 4.1: Daily gridpoint rainfall totals ($\mathrm{mm.day}^{-1}$) during the JJAS season over (a) the Indian land surface, as defined by Gadgil and Sajani (1998), (b) the $5 - 40°$N, $60 - 100°$E region used by Meehl and Arblaster (2003). Changes due to flux adjustment and CO_2 doubling are also shown.

make a quantitative estimate of the precipitation increase over the Indian region. First we consider the Indian land area already used in the rainfall teleconnection patterns of Fig. 3.17, and as defined by Gadgil and Sajani (1998). The summer monsoon season (JJAS) daily rainfall totals per gridpoint are shown in Table 4.1a, along with changes from the $1 \times CO_2$ scenarios. Clearly, increased greenhouse gas forcing causes an increase in monsoon season precipitation, between 3.5 and 12.7% depending on model version. The flux adjustments have a very significant effect on this value. This reinforces the suggestion that systematic errors in HadCM3 may be masking the true impact of doubling CO_2 concentration. It is also interesting to note the effect of flux adjustment alone for a given greenhouse gas concentration. The excessive summer monsoon in HadCM3 is reduced (as discussed in chapter 3), by 20.5% after flux adjustment. Removing the same systematic errors has a less noticeable effect in the future, (-13.5%).

For comparative purposes, and to give an idea of the broader behaviour, seasonal rainfall has also been measured over a larger region covering India, the Bay of Bengal, Arabian Sea and the Himalaya as well as other parts of Southeast Asia. The region is $5 - 40°$N, $60 - 100°$E, after Meehl and Arblaster (2003), who noted a change in gridpoint rainfall of $+9\%$ when carbon dioxide concentrations were doubled, looking at the JJA season. The response range to increased greenhouse gas concentration in HadCM3 as shown in Table 4.1b is $+5.2$ to $+8.5\%$ for JJAS ($+4.6$ to $+8.4\%$ for JJA).

The precipitation response to climate change can also be viewed in the context of air-sea interactions in the coupled system. Precipitation is plotted as a function of underlying SST for all months in the west Pacific ITCZ region in Fig. 4.4. These plots are probability density functions derived from a two dimensional Gaussian Kernel estimator devised by Marshall and Molteni (1993). The region chosen is $120-240°\mathrm{E}$, $10°\mathrm{S}-5°\mathrm{N}$ covering the bulk of the equatorial Pacific ITCZ after Spencer (2002).[4] The data used are all monthly mean values, and no further area or time averaging is carried out. The SST and precipitation ordinates are effectively split into bins into which the probabilities are estimated. Those data points near to the bin centre take a higher weighting using Gaussian functions. The main advantage of this technique over others $e.g.$, scatter plots, is that differences can be readily calculated. Accordingly, all four integrations are shown in Fig. 4.4, along with their differences, and CMAP precipitation versus HadISST surface temperatures $1979-1997$. Figure 4.5 shows the difference between the pdfs of each of the model integrations and the observed CMAP/HadISST pattern. The pdfs for HadCM3 and CMAP/HadISST look quite similar, indicating suppressed convection at low SST, increasing exponentially as SST rises. This similarity was also noted between the atmospheric component of the model, HadAM3, and observations by Spencer and Slingo (2003). It is clear from Fig. 4.4 that maximum precipitation (measured at the highest probability) is occurring at a higher underlying surface temperature in HadCM3 than observations, $30°\mathrm{C}$ compared to $29°\mathrm{C}$. This shift to higher rainfall at higher SSTs is also noted in the probability difference of Fig. 4.5.

One can look at the change in precipitation response due to flux adjustments at each of the carbon dioxide concentrations. Figure 4.4 shows that flux adjustment seems to tighten the contours in the main response peak (increased probabilities over $29-30°\mathrm{C}$ waters, and reduced probabilities either side). Thus the rainfall response to increased SST is steeper in HadCM3FA. There is also a reduction in probability for drizzle to occur over a range of SSTs in the mid-20s. Now looking at Fig. 4.5, it is evident that this

---

[4] The MATLAB code for the Gaussian Kernel estimator was provided by Hilary Spencer.

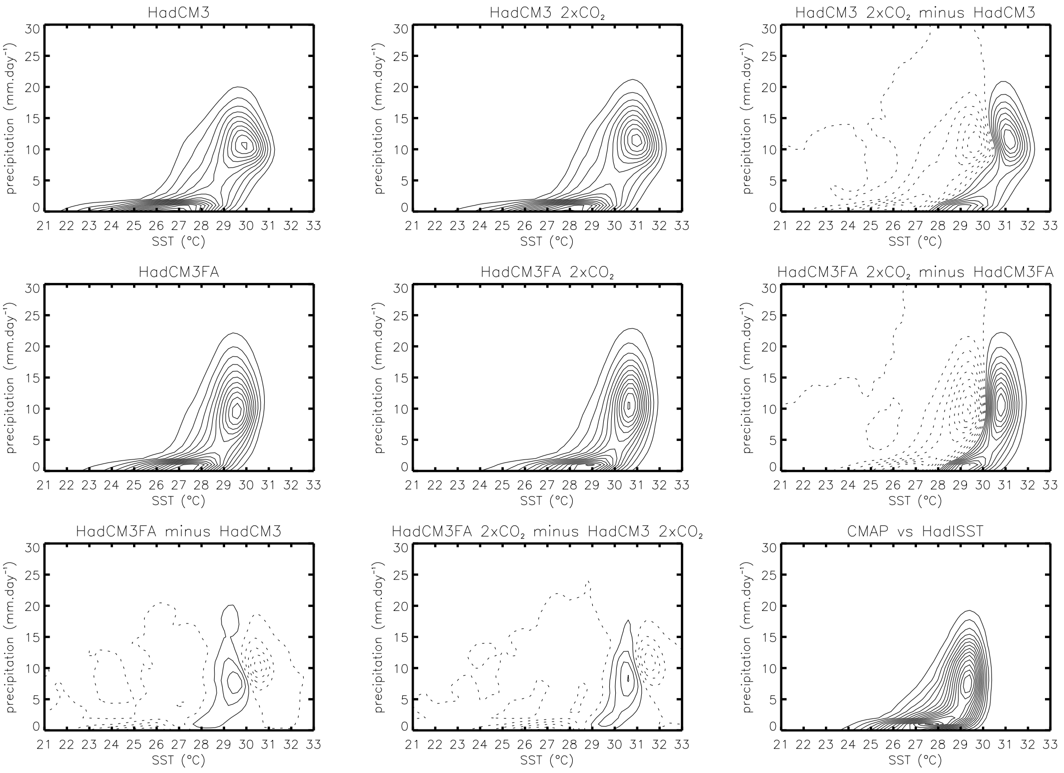

Figure 4.4: Probability density function of monthly-mean precipitation as a function of local SST for all months in the model integrations and 1979–1997 in the CMAP observations. Differences between the model versions are also shown. Measurements are taken at each grid point in the area $120°\mathrm{E} - 120°\mathrm{W}$, $10°\mathrm{S} - 5°\mathrm{N}$. CMAP data was first interpolated to the model grid. Contour spacing is 0.25%, and negative differences are dashed.

system of flux correction has made the SST-rainfall interaction more realistic, although the reason for this is unclear. Looking back at Fig. 4.4, the response of this interaction to flux adjustment is clearly independent of the background greenhouse forcing. The response to increasing $\mathrm{CO_2}$ concentration is much more marked than the impact of flux adjustment alone, however, as seen in Figs. 4.4 and 4.5. Both HadCM3 and HadCM3FA under doubled $\mathrm{CO_2}$ conditions feature a shift to higher underlying SSTs of the monthly-mean precipitation response. Heavy precipitation now tends to occur over waters about $1°\mathrm{C}$ warmer, a point which will be returned to later.

Another way to look at the precipitation-SST interaction is to divide the SST into bins and then average the precipitation over regions with that SST. This is done in Fig. 4.6a after Rajendran *et al.* (2004) for regions in the Indian and west Pacific Oceans

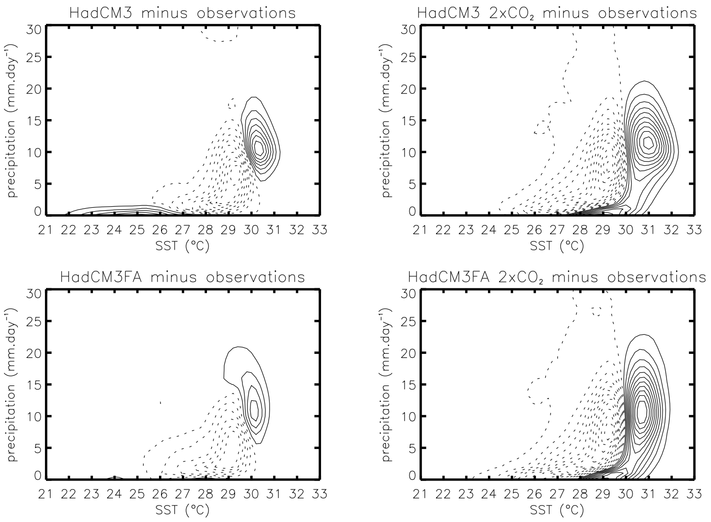

Figure 4.5: As Fig. 4.4 but showing pdf differences between the four model integrations and CMAP/HadISST (1979–1997) observations.

during summer (JJAS). The observations and model response both show that organized convection does not occur over the cold oceans, as in the MRI-CGCM2 studied by Rajendran *et al.* (2004). This trigger value seems to lie at just over $27^\circ\mathrm{C}$ for the observed curve, with good model agreement. Thereafter, a region of almost linear precipitation increase with SST occurs, represented well in both versions of the model and in both ocean regions shown. After maximum response, there is then a sharp decrease in precipitation with SST. The value at which this occurs is approximately $29^\circ\mathrm{C}$ in the Indian Ocean whilst $30^\circ\mathrm{C}$ in the west Pacific. There seems to be little difference between the models with and without flux correction under $1 \times \mathrm{CO}_2$ conditions, although the precipitation maximum in the Indian Ocean does seem more realistic. The effect of climate change is very similar to that shown in the whole year pdfs of Fig. 4.4, and again much more significant than that of the flux adjustment. The thresholds both for convection and convection cut-off seem to be shifted to warmer SSTs, by about $1.5^\circ\mathrm{C}$ in each ocean. Note that the sharp peaks around $32^\circ\mathrm{C}$ in the west Pacific can be thought of as outliers, being the mean of only one or two datapoints, compared to hundreds for other parts of the curve.

Figure 4.6b shows the close relationship between increasing SST and vertical ascent, and consequently illustrates the proximity of ascent and precipitation anomalies.

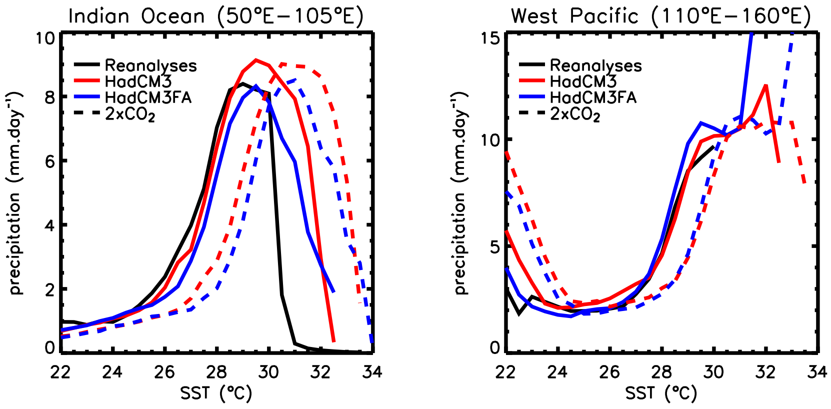

(a) Precipitation response to SST

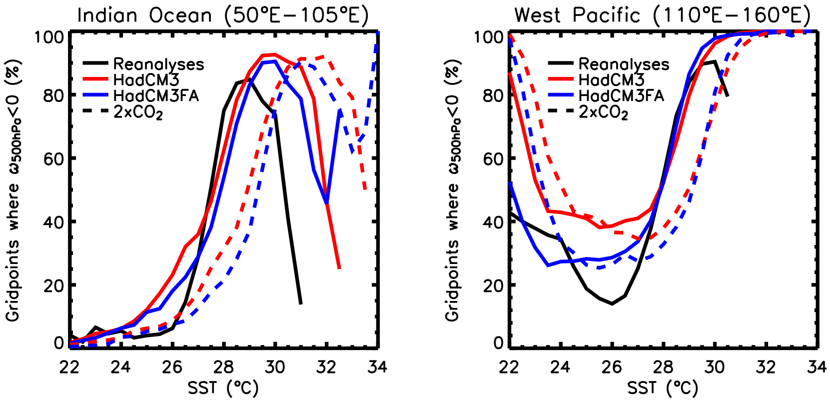

(b) Vertical velocity response to SST

Figure 4.6: (a) Precipitation response and (b) regional fraction undergoing vertical ascent at $500\mathrm{hPa}$ over given SST. CMAP precipitation, ERA-40 vertical velocities and HadISST temperatures are used as observations over 1979–1997 for consistency. Bins are $0.5^\circ\mathrm{C}$ wide, and the rainfall or ascent is meaned within each bin. Measurements are made at each gridpoint in the Indian Ocean (50–$105^\circ\mathrm{E}$) and west Pacific region (110–$160^\circ\mathrm{E}$), both over the latitudinal band $20^\circ\mathrm{S}$–$30^\circ\mathrm{N}$ after Rajendran *et al.* (2004). June-September monthly means are used.

The regions of the curves in Figs. 4.6a,b which show a linear relationship between vertical ascent or precipitation with increasing underlying SST seem to coincide for all datasets. This linear correspondence stops at a certain level due to the shading effect of convective clouds on the water below, argue Bony *et al.* (1997). That the fraction of vertical ascent decreases over the warmest SSTs suggests the presence of cloud free areas over these waters, also found by Rajendran *et al.* (2004). Bony *et al.* (1997) suggest that these further SST increases may only occur when convection is suppressed by subsidence due to remote forcing. Thus rather than obeying a Clausius-Clapeyron type relation at these high temperatures, the fall in convective activity occurs due to the resulting subsidence of remote large scale convective activity such as a monsoon system, which acts to regulate ocean temperature. Alternatively the local presence of intraseasonal activity such as the suppressed phase of the MJO may allow increasing SSTs. The effect of climate change on the $\omega_{500} - \mathrm{SST}$ relationship is the same as that on the precipitation response to SST, namely that the trigger and cut-off SSTs are shifted upward in quite a linear fashion. Whilst continuing to indicate the close relationship between vertical ascent and organized convection, this rather suggests that the simple Clausius-Clapeyron relation is not adequate to explain this response. It is interesting to note that the precipitation or ascent peak remains at the same level when carbon dioxide concentration is increased in the models. With the increasing availability of observational data it would be interesting to see if a similar shift in the curve occurs after a climatic or interdecadal change in SST. In addition, consideration of data at different frequencies such as daily data may have a profound impact on the study.

4.4 The role of climate change in monsoon variability

As well as the mean monsoonal climate, the future variability of the season will be of prime importance. Any increase in the spread around the mean will require societies to be increasingly adaptable. The dynamical monsoon index (DMI) is shown in Fig. 4.7 for both versions of the Unified Model under $2\times\mathrm{CO}_2$ conditions. Table 4.2 summarizes the interannual standard deviation on the DMI. This reaches $1.51\mathrm{ms}^{-1}$ in HadCM3 $2\times$

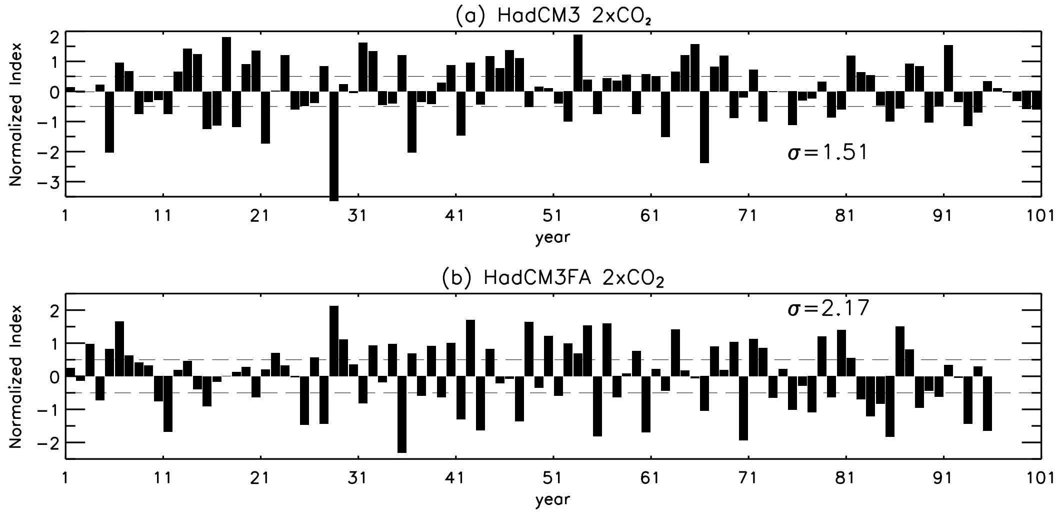

Figure 4.7: The summer (JJAS) dynamical monsoon index as described in Eq. (2.1) averaged over 5–20°N, 40–110°E for (a) HadCM3 $2 \times CO_2$ and (b) HadCM3FA $2 \times CO_2$. Note that the years in the two model runs are entirely independent.

CO_2	HadCM3	HadCM3FA	ERA-40
reanal.	-	-	1.60
$1 \times CO_2$	1.22	2.05	-
$2 \times CO_2$	1.51	2.17	-

Table 4.2: Interannual standard deviation (σ) of the summer (JJAS) DMI in Figs. 3.7 and 4.7.

CO_2, an increase of nearly 24% over the equivalent $1 \times CO_2$ integration, but still lower than that for the ERA-40 reanalysis. Using flux adjustments (Fig. 4.7b), variability is increased, as was found in the $1 \times CO_2$ scenarios of chapter 3. Kitoh *et al.* (1997) in a transient CO_2 experiment, and May (2004) in a future $2 \times CO_2$ timeslice experiment, also observe larger interannual variability of the Asian summer monsoon.

The HadCM3 $2 \times CO_2$ integration in Fig. 4.7a features some very dynamically weak monsoons, but otherwise the distribution of events is not unlike that under $1 \times CO_2$ conditions (Fig. 3.7b). Whilst having a higher spread, HadCM3FA $2 \times CO_2$ (Fig. 4.7b) shows clear evidence of a period of biennial monsoon variability, $i.e.$, a dynamically strong monsoon followed by a weak one, and vice-versa. This characteristic will be studied in more detail later. The spread of extreme monsoons can be described by a probability density function (pdf) chart of the DMI, as shown for all model integrations and ERA-40 in Fig. 4.8. Figure 4.8f shows a line plot of all pdfs for comparative purposes. The general behaviour in the model is one of higher probabilities in the extremes and reduced occurrence of normal conditions. Hence the pdfs are slightly squashed, HadCM3 (Fig. 4.8a) and HadCM3FA (4.8b) showing greater tendency for monsoons to occur in the ±0.5–2σ range than ERA-40 (Fig. 4.8e). Although difficult to draw any robust conclusions due to the number of timepoints available, the effect of both flux adjustments and CO_2 doubling is one of more frequent and stronger extremes. Further evidence for this can be seen in the following composite analysis.

Continuing as under $1 \times \mathrm{CO}_2$ conditions, the DMI can be used to delineate strong and weak monsoons, indicated by the $\pm0.5\sigma$ lines in Fig. 4.7. A composite difference of strong and weak summer monsoon seasons (JJAS) is shown for precipitation and $850\mathrm{hPa}$ winds in Fig. 4.9, and for surface temperature in Fig. 4.10.

The wind difference pattern for HadCM3 $2 \times \mathrm{CO}_2$ is similar to that at $1 \times \mathrm{CO}_2$ (Fig. 3.8) although stronger, the cyclonic anomaly over the Bay of Bengal being stronger, the monsoon flow being stronger, and the anomalous inflow into the Maritime Continent being greater. Associated with these circulation patterns are precipitation increases, dynamically strong monsoons now being wetter by $2\mathrm{mm.day}^{-1}$ in the west of India, and up to $3\mathrm{mm.day}^{-1}$ in the Bay of Bengal, whilst the Maritime Continent and the Indian Ocean to the west of Sumatra receive a further $4\mathrm{mm.day}^{-1}$. The drier region associated with the anomalously strong Pacific trades is down by $6\mathrm{mm.day}^{-1}$ during strong monsoon years. The West African monsoon winds seems noticeably stronger in HadCM3 $2 \times \mathrm{CO}_2$ during strong Asian summer monsoon years. Now looking at Fig. 4.9b for HadCM3FA, as in $1 \times \mathrm{CO}_2$ case, the flux adjustments have caused an increase in variability in the Indo-Pacific basins. The same systematic patterns are evident as in the uncorrected model. India is now wetter by $3\mathrm{mm.day}^{-1}$, and $4\mathrm{mm.day}^{-1}$ over the Bay of Bengal, during strong monsoon summers. The anomalous cyclonic flow just south west of Sumatra means that strong monsoon summers are $6\mathrm{mm.day}^{-1}$ wetter there than weak summers. There is now evidence of additional wetness in the Gulf of Guinea, part of the West African monsoon, coinciding with the anomalous westerlies across the continent.

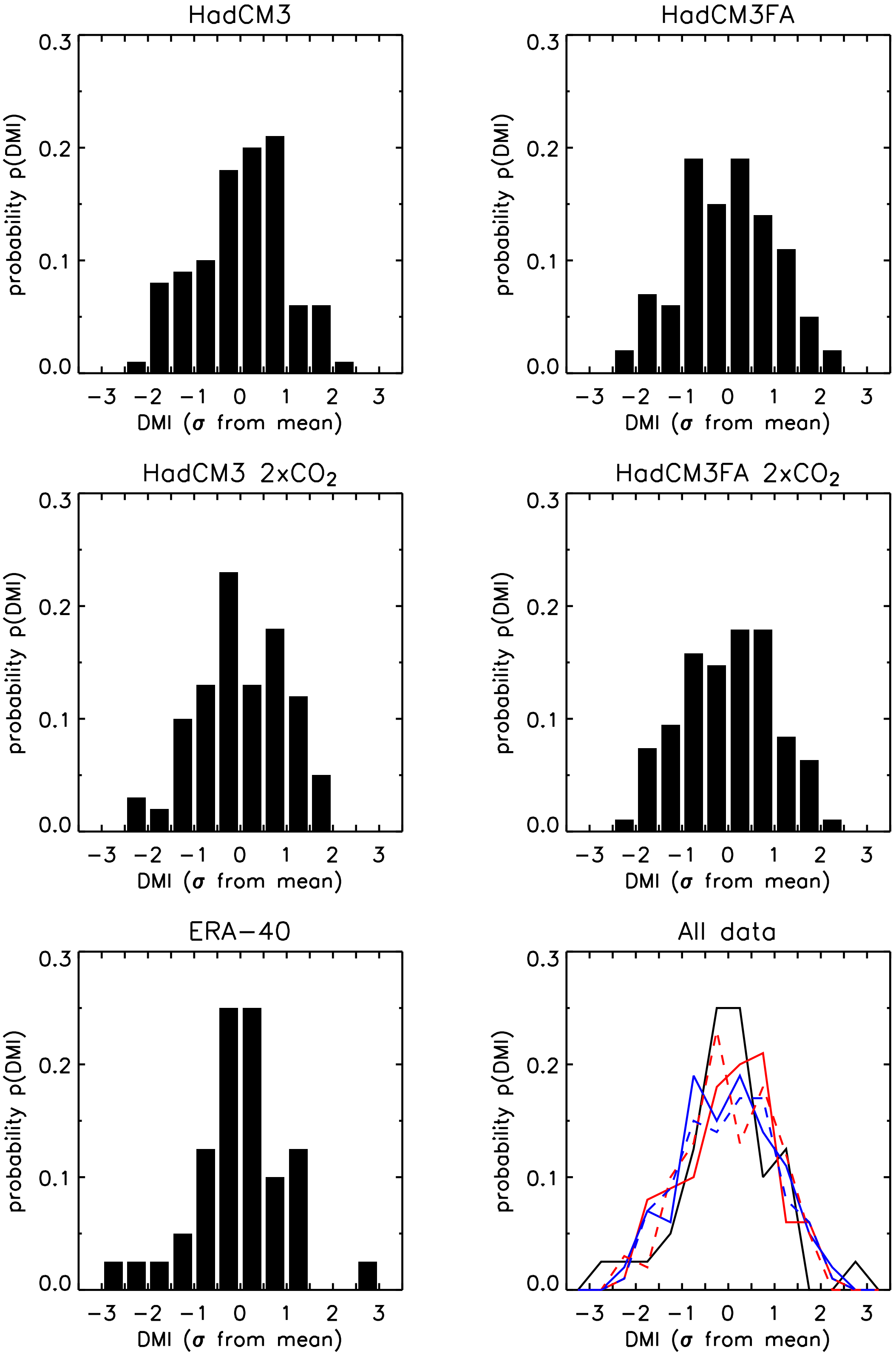

Figure 4.8: Probability density functions of the DMI in each model integration (a-d) and ERA-40 (e). Curves for all datasets are plotted in (f). Bins are 0.5σ wide. Those monsoons outside the $\pm 0.5\sigma$ bounds are those classed as strong or weak in the composite plots.

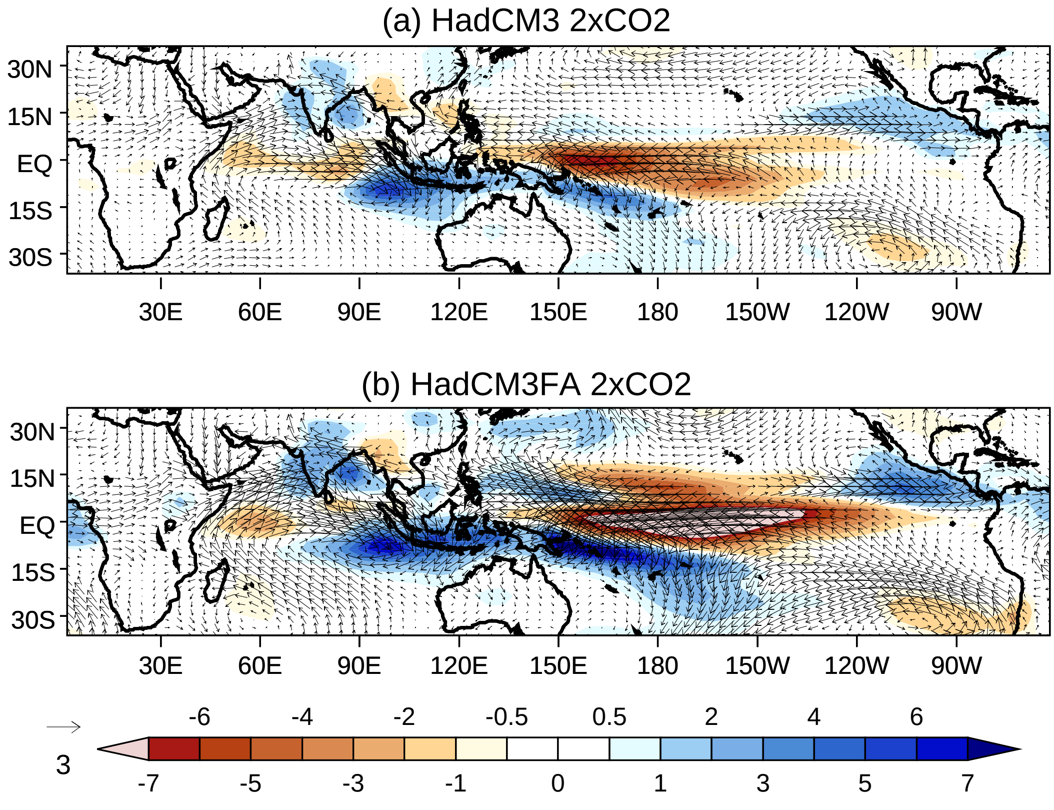

Figure 4.9: Strong minus weak summer (JJAS) composite difference plots of lower tropospheric $(850\mathrm{hPa})$ winds and precipitation for (a) HadCM3 $2 \times \mathrm{CO}_2$ and (b) HadCM3FA $2 \times \mathrm{CO}_2$. Unit wind vectors are $3\mathrm{ms}^{-1}$.

Now looking at the monsoon difference composite for surface temperature (Fig. 4.10), climate change has increased the variability in the central equatorial Pacific, $1.5°\mathrm{C}$ colder in strong summers than weak summers for HadCM3, rising to $4°\mathrm{C}$ in HadCM3FA $2{\times}\mathrm{CO}_2$. It is interesting to note that as the monsoon variability increases (Fig. 4.9), and with it the equatorial Pacific variability (Fig. 4.10), the Indian Ocean surface temperature variability changes little, both in the application of flux-adjustments and the response to increased greenhouse forcing. This highlights the dominating teleconnection between the Asian summer monsoon and ENSO.

(a) HadCM3 2xCO2

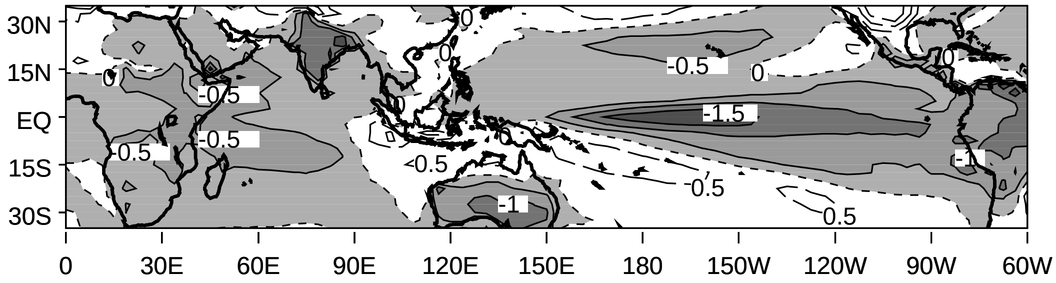

(b) HadCM3FA 2xCO2

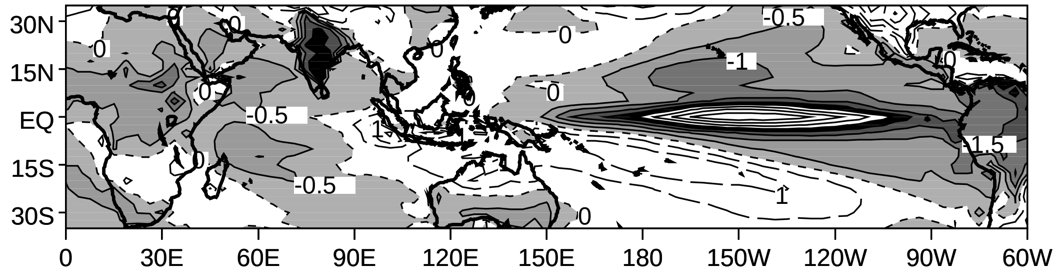

Figure 4.10: Strong minus weak summer (JJAS) composite difference plots of surface temperature (K) for (a) HadCM3 $2 \times \mathrm{CO}_2$ and (b) HadCM3FA $2 \times \mathrm{CO}_2$. Negative differences are shaded whilst dashed contours show positive differences. Contour interval is $0.5\mathrm{K}$.

4.5 The impact of climate change on ENSO and its variability

4.5.1 The mean thermocline

Timmermann *et al.* (1999) argue that the most important change to the future mean climate that could effect ENSO is strengthening of the thermocline. Figure 4.11 shows the mean state of the equatorial Pacific thermocline under $2 \times \mathrm{CO}_2$ forcing conditions in both versions of the Unified Model, and Fig. 4.12 then shows the thermocline response to increasing greenhouse gas forcing. Doubling carbon dioxide concentration has quite a dramatic effect on the positioning of the west Pacific warm pool in both versions of the model. Comparing Figs. 4.11 and 3.4, it is clear that at the ocean surface on the equator, the edge of the warm pool (defined here as the $28°\mathrm{C}$ isotherm) is brought further east by $15 - 20°$, even reaching past the dateline in HadCM3FA $2 \times \mathrm{CO}_2$ (Fig. 4.11b). The west Pacific warm pool is also noticeably shallower comparing HadCM3FA and

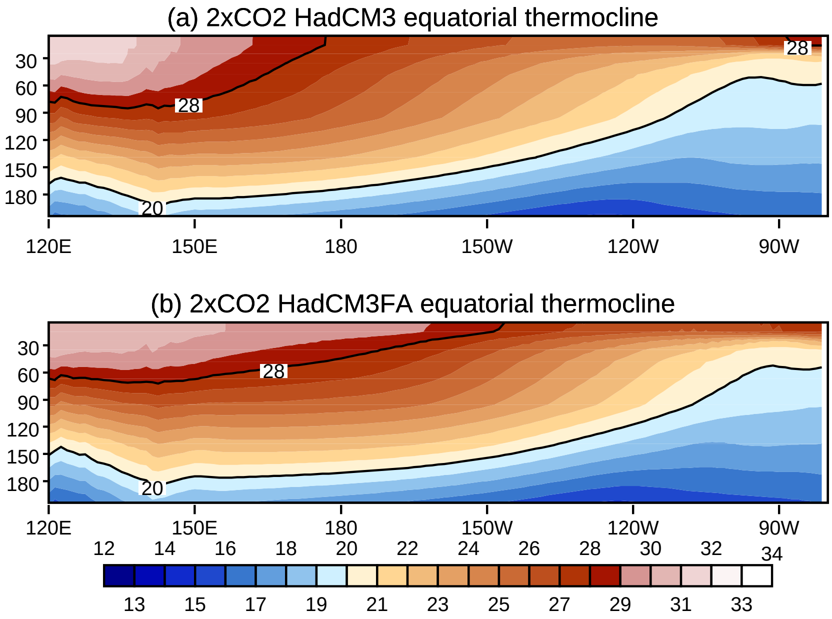

Figure 4.11: Annual mean thermocline profile along the equatorial (0.625°N–0.625°S) Pacific for (a) HadCM3 2 × CO_2 and (b) HadCM3FA 2 × CO_2. The 20°C and 28°C isotherms are highlighted.

HadCM3, both at 2 × CO_2. The shallow cold waters in the east (below 20°C), seem to be more zonally confined in both the 2 × CO_2 integrations when compared to 1 × CO_2 (Fig. 3.4), likely due to the high surface warming there. This reduction in volume of the cold water region does not seem to denigrate the ability of the models to form large El Niño-La Niña events through tilting of the thermocline, as we shall see later.

Looking at the response to greenhouse gas doubling in Fig. 4.12, the thermocline is intensified by climate change. This is not simple amplification of the mean, but more heating in the upper eastern region compared to the lower and western regions. On the surface, this contributes to the slackening of the zonal SST gradient, or El Niño-like warming noted earlier. Collins (2000b) notes that the vertical temperature gradient is enhanced at 2 × CO_2 due to the slow rate of heat penetration into the ocean. Once warmed, the upper levels become stable due to their buoyancy, allowing downward advection of heat only by diffusion. This prevents rapid warming at depth, contributing to the modelled pattern in Fig. 4.12.

The impact of flux correction on the equatorial region of the mean thermocline is assessed in Fig. 4.13. It is clear flux adjustments affect the thermocline in a slightly

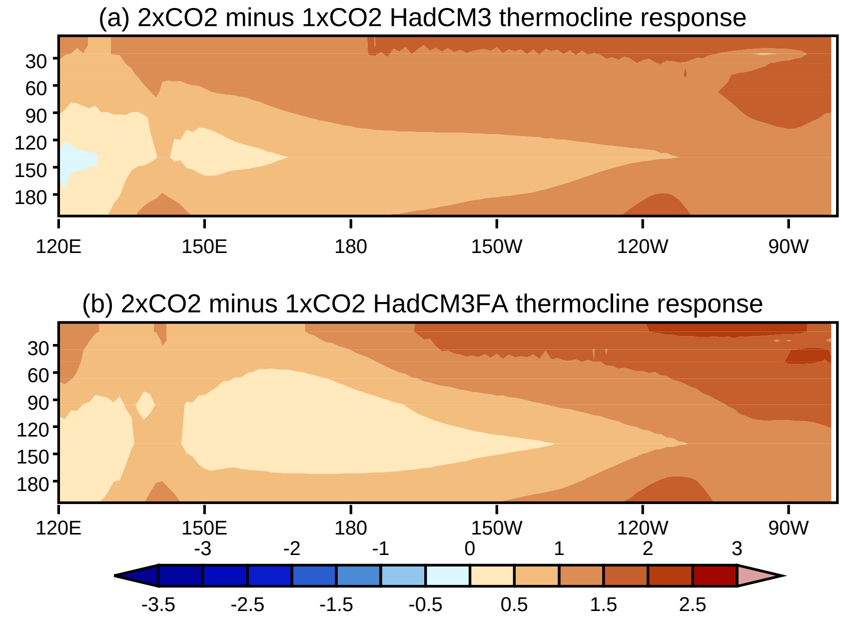

Figure 4.12: Response of the annual mean thermocline to increasing greenhouse gas forcing for (a) HadCM3 (b) HadCM3FA.

different way to increased greenhouse gas forcing. The concentration of the largest fluxes in the central Pacific (Fig. 3.2a) warms a large span of the region which continues to depth. The edge of the west Pacific warm pool is moved eastward whilst the region beneath is cooled by up to $2°\mathrm{C}$ at $100\mathrm{m}$ depth. The pattern at $2 \times \mathrm{CO}_2$ is almost identical to that at $1 \times \mathrm{CO}_2$ (Figs. 4.13b,a), as expected given the identical application of flux adjustment. Interestingly, these flux adjustment response patterns are very similar to those shown in the transient warming trend of Timmermann *et al.* (1999). Their study noted the thermocline trend to resemble anomaly patterns of El Niño. We have already noted earlier in this chapter the propensity for greater El Niño-like warming in the HadCM3FA version of the model, so this similarity is not surprising.

4.5.2 The annual cycle in the Pacific

Before considering the possible effect of climate change on ENSO variability, it is important to look at the effect on the annual cycle of the equatorial Pacific. Figure 4.14 shows the evolution of equatorial Pacific SST anomalies for HadCM3 under both greenhouse forcing conditions, and their difference. As the anomaly to the annual mean is

(a) HadCM3FA minus HadCM3 response (1xCO2)

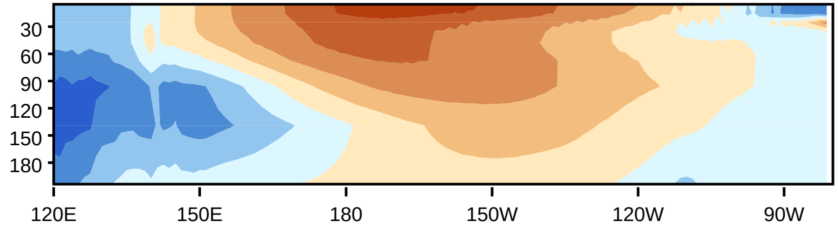

(b) HadCM3FA minus HadCM3 response (2xCO2)

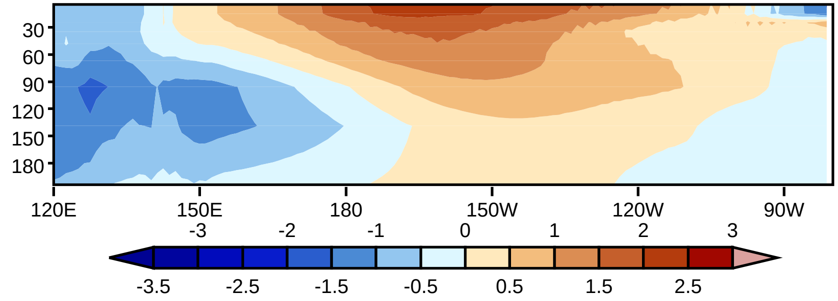

Figure 4.13: Response of the annual mean thermocline to flux adjustment at $1 \times \mathrm{CO}_2$ and $2 \times \mathrm{CO}_2$.

taken, this will allow easy recognition of any shifts in the timing of the annual cycle. In Fig. 4.14a, the warming through spring followed by cooling during northern autumn at $\sim 120^\circ\mathrm{W}$ is a reminder of typical Niño-3 region SST evolution shown earlier in Fig. 3.10. In the east Pacific, SST evolution is damped slightly under $2 \times \mathrm{CO}_2$ conditions, while slightly enhanced in the *central* region. This is slightly contradictory to the findings of Timmermann *et al.* (2004) who attributed a strong east Pacific intensification of the annual cycle under the IS92a emissions scenario to the asymmetric temperature response in the region, mainly due to the uneven hemispheric land mass distribution. Given that the same condition holds here, it is likely some other mechanism is at play. Looking at the difference (Fig. 4.14c), there seems to be evidence of precession of the warming and cooling antinodes of the annual cycle, *i.e.*, the warming (and cooling) bands are occurring earlier in the calendar year. We can compare the changes to the annual cycle of SST with surface winds. Figure 4.15 shows the evolution of 10m zonal winds across the Pacific (Fig. 4.15a), and their anomaly to the annual mean (Fig. 4.15b), in both emission scenarios of HadCM3. The mean winds across the Pacific are predominantly easterly (negative), and their relaxation during the boreal spring is clearly noted in Fig. 4.15a. How this spring relaxation affects El Niño devel-

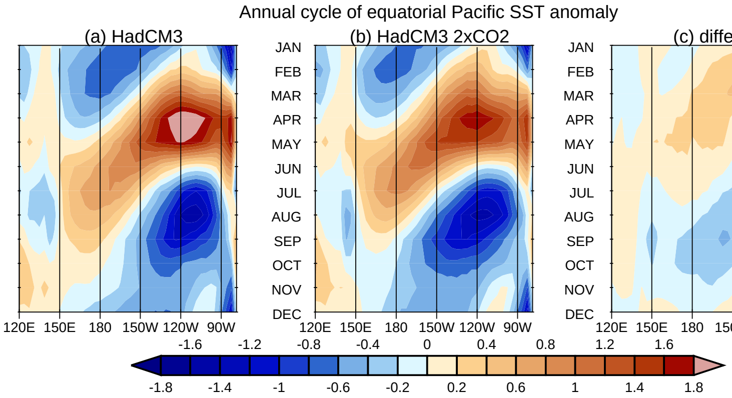

Figure 4.14: Annual cycle of equatorial ($\pm 2.5°$N) Pacific SST anomalies to the annual mean in (a) HadCM3, (b) HadCM3 $2 \times CO_2$ and (c) the response to $2 \times CO_2$.

opment will be considered later in this section. The relaxation is clearly intensified by doubling CO_2, although the period of strong central Pacific trades later in the year is diminished in length. Now looking at the anomalies to the annual mean in Figs. 4.15d-f, the difference (Fig. 4.15f) again demonstrates an intensification of the cycle, with evidence of precession. This is particularly obvious in the east Pacific. Whilst the annual cycle in the west is largely controlled by the seasonal motion of the sun, that in the east is driven mostly by strong ocean-atmosphere coupling (Guilyardi, 2006), and thus most susceptible to change. The reason for this change however remains unclear.

4.5.3 Niño-3 behaviour

Now focussing on the eastern equatorial Pacific, we have already seen in Fig. 3.10 that HadCM3 is quite good at simulating the climatological seasonal cycle there. Figure 4.16 shows how this simulation changes for the Niño-3 region in a future climate. Both versions of the model are consistently warmer by around $1.8°C$ at $2 \times CO_2$. The flux corrected version is slightly hotter than the standard Unified Model. No changes to the timing of the cycle are seen here.

Looking at the interannual variability for each month of the year in the Niño-3 region, Fig. 4.16 now takes into account the impact of climate change. Uncorrected, the HadCM3 east Pacific responds to $2 \times CO_2$ with a slightly preferential increase in variability in the (northern) late autumn-winter season, $i.e.$, the system of El Niño-La

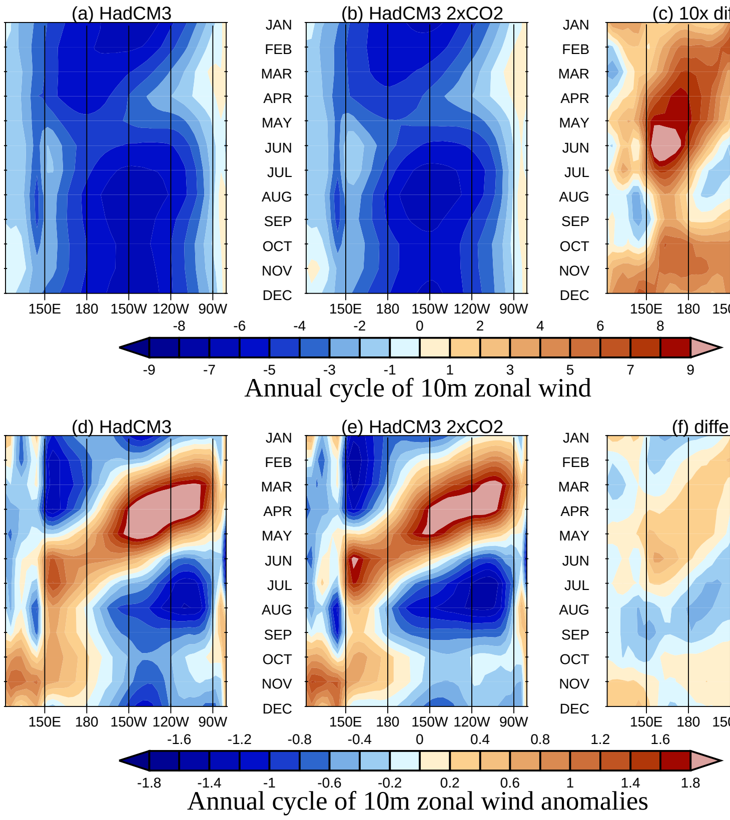

Figure 4.15: Annual cycle of equatorial ($\pm 1.25°$N) Pacific surface zonal winds (a-c) and their anomalies to the annual mean (d-f) in HadCM3, HadCM3 $2 \times \mathrm{CO}_2$ and the response to $2 \times \mathrm{CO}_2$. Units are ms^{-1}, and $\times 10^{-1}\mathrm{ms}^{-1}$ in (c).

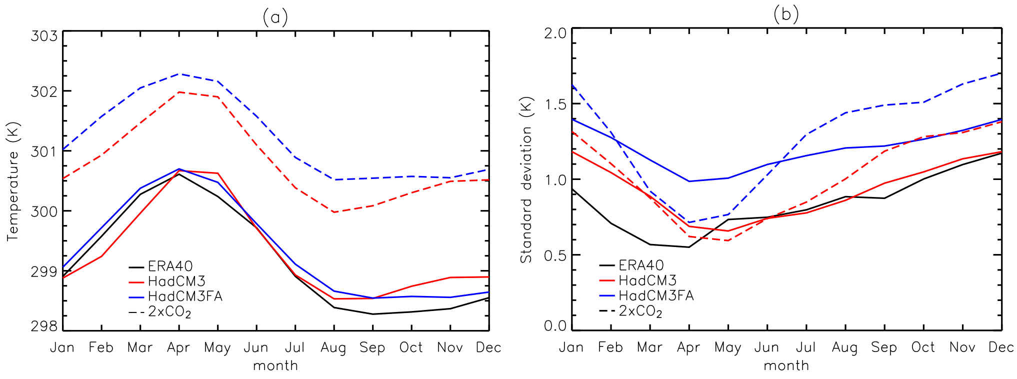

SST seasonal cycle

Cycle of interannual SST standard deviation

Figure 4.16: Niño-3 region SST behaviour for ERA-40, HadCM3, and HadCM3FA. (a) SST seasonal cycle, (b) Seasonal cycle of interannual standard deviations. Solid lines are for $1 \times \mathrm{CO}_2$ conditions whilst dashed lines are the $2 \times \mathrm{CO}_2$ scenario.

CO_2	index	HadCM3	HadCM3FA	ERA-40
reanal.	SPL	-	-	0.19
	σ	-	-	0.85
$1 \times CO_2$	SPL	0.19	0.14	-
	σ	0.94	1.21	-
$2 \times CO_2$	SPL	0.28	0.35	-
	σ	1.05	1.32	-

Table 4.3: Seasonal phase lock index (SPL) and El Niño anomaly amplitude (σ) of the Niño-3 region. Units are $^\circ$C.

Niña warming and cooling is slightly more phase locked to the seasonal cycle. In the $1 \times CO_2$ climate, flux adjustments had resulted in an increase in variability for all months of the year. At $2 \times CO_2$ however, flux adjustments cause an increase in Niño-3 SST variability in the autumn and winter seasons, whilst the boreal spring remains a variance minimum, or *spring predictability barrier*. Hence in HadCM3FA $2 \times CO_2$, ENSO is much more strongly phase-locked to the seasonal cycle.

A useful measure of this characteristic is devised by Guilyardi (2006), defined as the standard deviation of the monthly stratified standard deviation of Niño-3 anomalies, $i.e.$, the standard deviation of the curves in Fig. 4.16. This *seasonal phase lock index* (SPL) will indicate the impact of the relaxation of the seasonal cycle (the slackening of equatorial Pacific trade winds in boreal spring, seen in Fig. 4.15a) on the potential for developing El Niño events. A small SPL will show that the seasonal cycle does not offer enough relaxation time to allow El Niño to develop via Bjerknes feedback. Table 4.3 shows the SPL for all model integrations and ERA-40, together with the El Niño amplitude, defined as the standard deviation of the Niño-3 anomaly index. For the uncorrected and flux adjusted version of the model, as carbon dioxide concentration increases, the SPL index and Niño-3 amplitude both increase, indicating the role of seasonal wind relaxation in allowing El Niño to develop. We have already shown in Fig. 4.15b that the relaxation of winds at $2 \times CO_2$ is intensified when compared to $1 \times CO_2$. Indeed, Guilyardi (2006) found the modelled El Niño amplitude to have an almost linear relationship with the SPL index, when looking at pre-industrial, $2 \times \mathrm{CO}_2$ and $4 \times \mathrm{CO}_2$ scenarios. However, Guilyardi (2006) excludes the only flux adjusted model in the IPCC AR4 suite (MRI-CGM2.3.3) from the linear fit of these statistics. It performs much better at this relation than several of the other models, which often show a negative tendency with CO_2 forcing, no tendency, or one which changes sign between $2 \times \mathrm{CO}_2$ and $4 \times \mathrm{CO}_2$. Hu *et al.* (2000) noticed increased ENSO variability in transient simulation of a warmer climate, connected to higher monsoon variability, which appears to be the case here.

Guilyardi (2006) also defines the El Niño amplitude as an inverse function of the mean trade winds (the annual mean zonal wind stress in the Niño-4 region). Thus GCMs with a systematic bias of strong trade winds are likely to feature weak El Niños. We have already established that the flux corrected model at both CO_2 levels features trade winds of reduced strength, and this is reflected in the increased El Niño amplitude. The strength of trade winds in the model integrations will be returned to in chapter 5.

The relative strength of the seasonal cycle was also used by Guilyardi (2006) to define the amplitude of El Niño, as an inverse function, since a strong seasonal cycle is less likely to be disturbed. The power spectra of the Niño-3 region SSTs are shown (with no seasonal adjustment) in Fig. 4.17. The curves are normalized to the annual cycle in order to demonstrate the relative power of oscillations on El Niño timescales, and the normalization factors are indicated in the figure. At $1 \times \mathrm{CO}_2$ and HadCM3 $2 \times \mathrm{CO}_2$, the annual cycle dominates. It is clear the two versions of the model obey the inverse relation: applying flux adjustments at a given carbon dioxide concentration increases the relative power at interannual timescales (although the power in the annual cycle is also increased, as measured by the normalizing factors in Fig. 4.17). Similarly, a given model version features more power at interannual timescales relative to the annual cycle when under $2 \times \mathrm{CO}_2$ conditions (and the strength of the annual cycle declines). Indeed, in the HadCM3FA $2 \times \mathrm{CO}_2$ integration, the annual cycle is no longer the dominant peak. These findings mirror those of Guilyardi (2006), who found that there was likely to be an increased El Niño amplitude under stronger greenhouse gas forcing. Using HadCM2, Collins (2000a) found no significant change to ENSO characteristics at the

$2 \times \mathrm{CO_2}$ level, whilst in HadCM3 Collins (2000b) found no change even at $4 \times \mathrm{CO_2}$. The different greenhouse gas response in HadCM2 and HadCM3 was not attributed to the removal of global flux corrections, thus there are no direct implications for our use of partial corrections here. Using the NCAR CCSM ensemble under SRES-A1 forcing, Zelle *et al.* (2005) also note no significant change to ENSO amplitude, whilst Ashrit *et al.* (2003) regard the ENSO climate response as model dependent. Timmermann *et al.* (1999) found interannual ENSO variability to be much stronger during IS92a forcing.

Now moving on to the effects of climate change on ENSO period, both Zelle *et al.* (2005) using a model ensemble, and Guilyardi (2006) reviewing the IPCC AR4 models, found no significant or consistent changes to ENSO period. At $1 \times \mathrm{CO_2}$ we have already noted an increase in power on biennial timescales and broadening of the main ENSO peak (Turner *et al.*, 2005, and chapter 3) using HadCM3FA. Here, the doubling of $\mathrm{CO_2}$ in HadCM3 has caused no overall shift in the interannual peaks (Fig. 4.17). However, the spectrum for HadCM3FA $2 \times \mathrm{CO_2}$ looks very different. The dominant power at interannual timescales is confined to the biennial period and is much reduced at lower frequencies associated with ENSO. Whether this is a consequence of climate change previously masked by the systematic errors in HadCM3 or a facet of flux adjustments (HadCM3FA $1 \times \mathrm{CO_2}$ saw more power at biennial timescales) will be discussed in chapter 5. Using HadCM2 Collins (2000a) saw increased power over the $1.5 - 3\mathrm{yr}$ range in a $4 \times \mathrm{CO_2}$ simulation, but Collins (2000b) saw no such tendency in HadCM3. Timmermann (2001) also saw no significant trend in ENSO frequency in his $\mathrm{IS92a}$ forced integration of future climate using the ECHAM4/OPYC3 combination.

4.5.4 Basin-wide El Niño behaviour

Given the changes in El Niño characteristics discussed above it is useful to look at the behaviour across the whole Pacific basin while El Niño is at its peak. Figure 4.18 illustrates the lag-correlation between northern winter (DJF) Niño-3 SSTs and SSTs averaged across the equatorial Pacific ($2.5°\mathrm{N} - 2.5°\mathrm{S}$) for the two model versions under

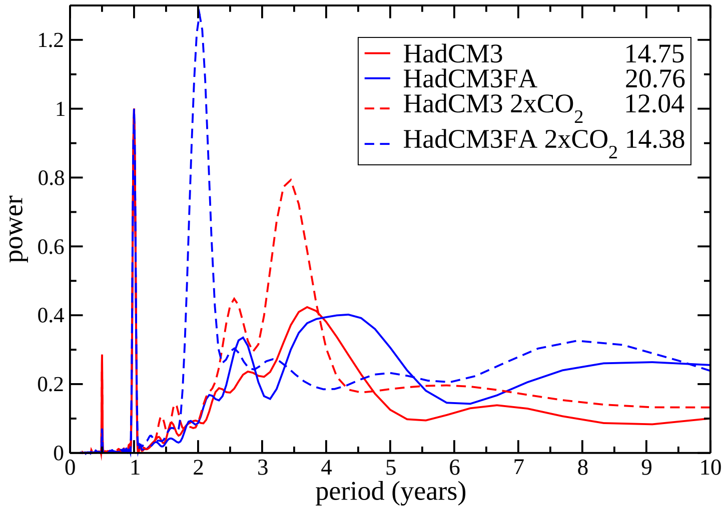

Figure 4.17: Power spectra of seasonally adjusted Niño-3 region SSTs in the HadCM3 and HadCM3FA model integrations. Solid lines indicate $1 \times CO_2$ conditions whilst dashed lines are for the $2 \times CO_2$ eventuality. All data are passed through a 20-year Tukey window before being normalized to the annual cycle, and the normalization factors are given.

$2 \times CO_2$ forcing. Comparing Fig. 4.18a with $1 \times CO_2$ conditions (Fig. 3.16b), the general pattern of correlation strength does not seem to have changed. However, there is more evidence of pre-El Niño extension of the warm pool. The post-El Niño pattern of warm pool retreat ($i.e.$, the return of warm waters from the central Pacific to the west) that was in evidence both in the reanalysis and HadCM3 (Figs. 3.16a,b respectively) seems no longer to occur under $2 \times CO_2$ conditions. This suggests a change in the shape of the teleconnection pattern right across the Pacific basin in the 6 months before and after an El Niño or La Niña event. There is now a hint of surface west to east propagation.

Now looking at the flux adjusted model and comparing the current and future climate scenarios (Figs. 3.16c and 4.18b) it is clear that the negative correlation strengths have increased during the periods before and after the ENSO event, now reaching -0.6. There is an obvious biennial character to the correlation pattern, indeed positive correlations can be seen returning 24 months after they originally appear. There is still good

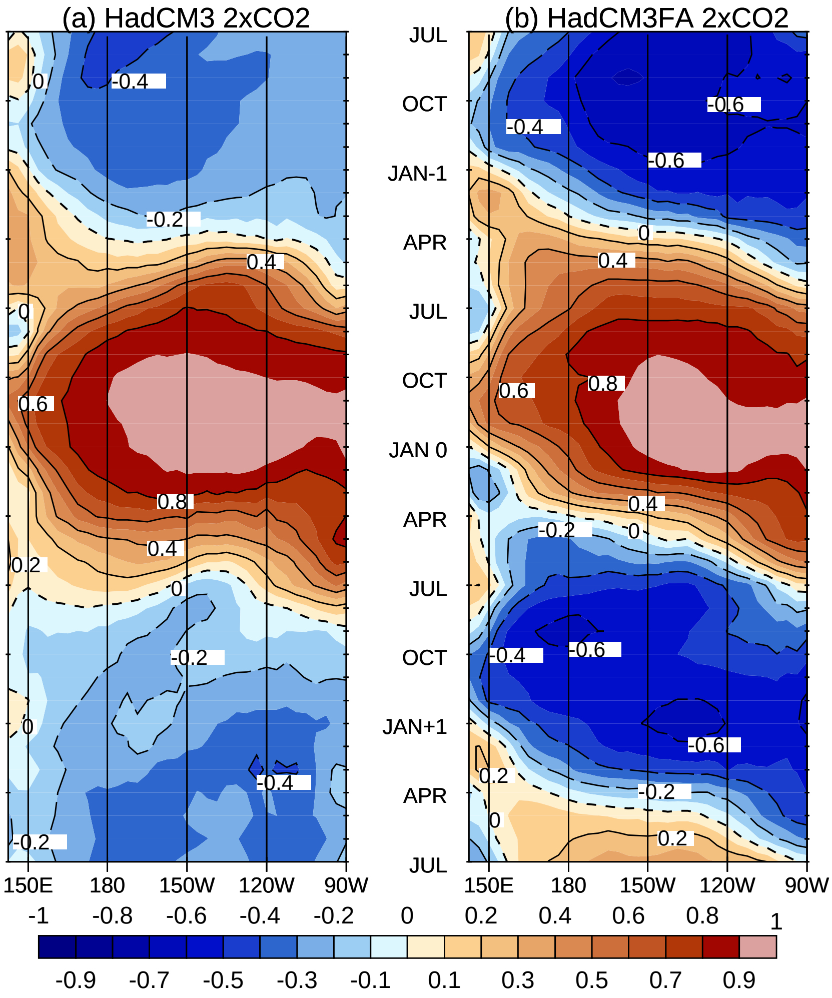

Figure 4.18: Lag correlations between winter season (DJF) Niño-3 SSTs and monthly equatorial Pacific (2.5°N–2.5°S) in (a) HadCM3 $2 \times CO_2$ and (b) HadCM3FA $2 \times CO_2$. Negative correlation contours are dashed. Correlations are significant in all but 5% of cases outside ± 0.2.

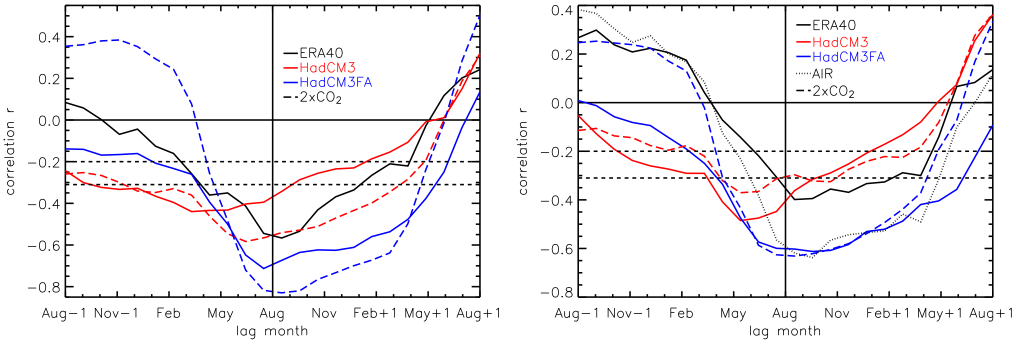

Niño-3 SST vs. DMI

Niño-3 SST vs. Indian rainfall

Figure 4.19: Correlation between Niño-3 SST and summer (JJAS) (a) DMI or (b) Indian rainfall plotted against lag time. In (b), AIR refers to the All-India Rainfall precipitation data being correlated with ERA-40 SSTs. Correlations significant in all but 5% of cases are indicated outside the dashed lines: $|r| > 0.31$ for the ERA-40, $|r| > 0.2$ for the model integrations.

supportive evidence of pre-El Niño warm pool extension, and now obvious regions of cooling can be seen in the west Pacific warm pool whilst the peak of El Niño is in the east. The shape change to the teleconnection pattern mentioned above for HadCM3 $2 \times \mathrm{CO}_2$ (Fig. 4.18a) is now much more obvious (Fig. 4.18b), showing a strong tendency for surface eastward propagation during El Niño events, more uniformly than in the uncorrected model. This suggests that the evolution of El Niño events has changed in the flux corrected future climate scenario, and this will be looked at in more detail in chapter 5.

4.6 Climate change and monsoon-ENSO teleconnections

It is now pertinent to consider the monsoon-ENSO teleconnection in these future climate scenarios. Figure 4.19 shows the lag-correlations between Niño-3 SST anomalies and the DMI or All-India Rainfall. Dashed curves show the correlations for the HadCM3 (red) and HadCM3FA (blue) versions of the model at $2 \times \mathrm{CO}_2$. Looking first at the dynamics (Fig. 4.19a), the teleconnection is strengthened under climate change in both versions of the model. In HadCM3, the timing of the teleconnection is later and compares to present day observations. The relationship between low-level winds

CO_2	HadCM3	HadCM3FA	ERA-40/AIR
observed	-	-	0.55
$1 \times CO_2$	0.25	0.47	-
$2 \times CO_2$	0.40	0.58	-

Table 4.4: Correlation between the summer (JJAS) dynamical monsoon index (DMI) and the All-India Rainfall (AIR) for the two models under $1 \times CO_2$ and $2 \times CO_2$ conditions, and the reanalysis/observations.

and east Pacific SSTs thus suggests that the Asian summer monsoon may become more predictable under $2 \times CO_2$ conditions. Looking at the rainfall relation in Fig. 4.19b, however, it appears that the effect on the teleconnection is not quite as robust. The HadCM3 teleconnection seems to weaken, whereas in HadCM3FA it stays at broadly the same strength during the summer and autumn. Using the broader rainfall region defined by Meehl and Arblaster (2003) which covers parts of the Indian Ocean as well as Bangladesh and the Himalaya, the rainfall teleconnection is a little more robust in the HadCM3 $2 \times CO_2$ integration (not shown), being slightly stronger than under $1 \times CO_2$ conditions. However there are no observations for this region of comparable record length. Ashrit *et al.* (2003) found no systematic change to the monsoon-ENSO teleconnection in their transient climate change study, indeed they noted the Niño-3 relation with the DMI to be quite robust, while other indices based on meridional wind shear in the Indian sector were less stable. In their study of the observed east Pacific SST and Indian rainfall records, Torrence and Webster (1999) found high coherence between the two regions during periods of high ENSO and high monsoon variability. This seems to be confirmed by our strengthened *dynamical* teleconnections during $2 \times CO_2$ forcing, concurrent with enhanced variability in both sections. It is less clear that this applies over our modelled Indian region, however.

We can now take another look at the summer correlation between the two measures of monsoon strength. Table 4.4 shows that increasing greenhouse gas concentration results in increased coupling between the modelled monsoon wind strength and precipitation output. This suggests that in future scenarios the DMI is increasingly useful as a descriptor for monsoon behaviour on the ground. The warming Pacific with increased El Niño behaviour impacts on the zonal Walker circulation, which goes on to impact on the DMI (a zonal measure). The increased moisture availability due to the warmer waters surrounding the monsoon regions allows for increased variability there. The Indian sector thus becomes more strongly driven by the Pacific in the future climate.

One can also verify the effect of flux adjustments on the teleconnection, as under $1 \times \mathrm{CO_2}$ conditions. Figure 4.20 shows the composite evolution of equatorial Pacific SSTs in 10 El Niño events from each of the future climate scenarios, through their development, maturity and decay. The same argument holds as in the $1 \times \mathrm{CO_2}$ integrations. The warmest waters are shifted further east, projecting the basic state changes due to flux adjustment onto the ENSO system. This helps HadCM3FA to have a stronger teleconnection than in HadCM3. The warmest absolute SSTs seem to occur slightly earlier, consistent with the precession of the annual cycle shown in Fig. 4.14, and the increased autumnal variability evident in the dashed curves of Fig. 4.16.

One consistency between the dynamical and precipitation lag-correlations shown in Fig. 4.19 lies in the strong positive correlations seen at lead times of 12 to 5 months for the HadCM3FA $2 \times \mathrm{CO_2}$ integration. This reaches $+0.4$ for the DMI and $+0.25$ for Indian rainfall, suggesting that eastern Pacific warmings (El Niño) during one summer are followed by strong Asian monsoons the following summer. There is, therefore, a strong biennial influence on the ENSO-monsoon system in the future climate HadCM3FA. This change in ENSO behaviour can be further elucidated by looking at the timeseries of Niño-3 SST anomalies in the future climate scenarios, as in Fig. 4.21. The trace of HadCM3 $2 \times \mathrm{CO_2}$ shows a pattern of El Niño onset and decay not unlike that in the $1 \times \mathrm{CO_2}$ scenarios. Now looking at the HadCM3FA $2 \times \mathrm{CO_2}$ integration, it is immediately clear that ENSO is behaving in a different way. A period of a rather irregular ENSO oscillation for the first 30 years or so is followed by more than 40 years of an oscillation that is clearly biennial. Hence an El Niño warming is followed by a La Niña cooling during the following year, followed by another El Niño. The irregular regime returns in the last couple of decades. The two different ENSO regimes, their event evolution, the transition between them and implications for monsoon prediction

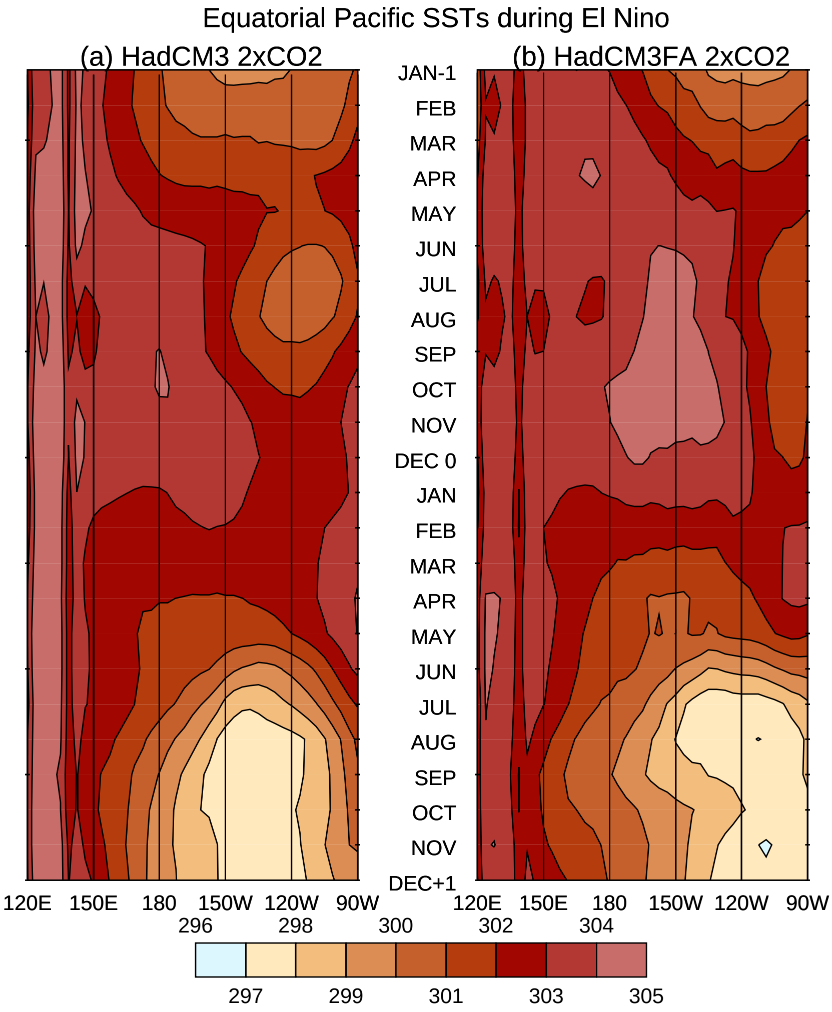

Figure 4.20: Evolution of mean equatorial Pacific SSTs ($2.5°$N–$2.5°$S) in a composite of 10 El Niño events in (a) HadCM3 $2 \times CO_2$ and (b) HadCM3FA $2 \times CO_2$.

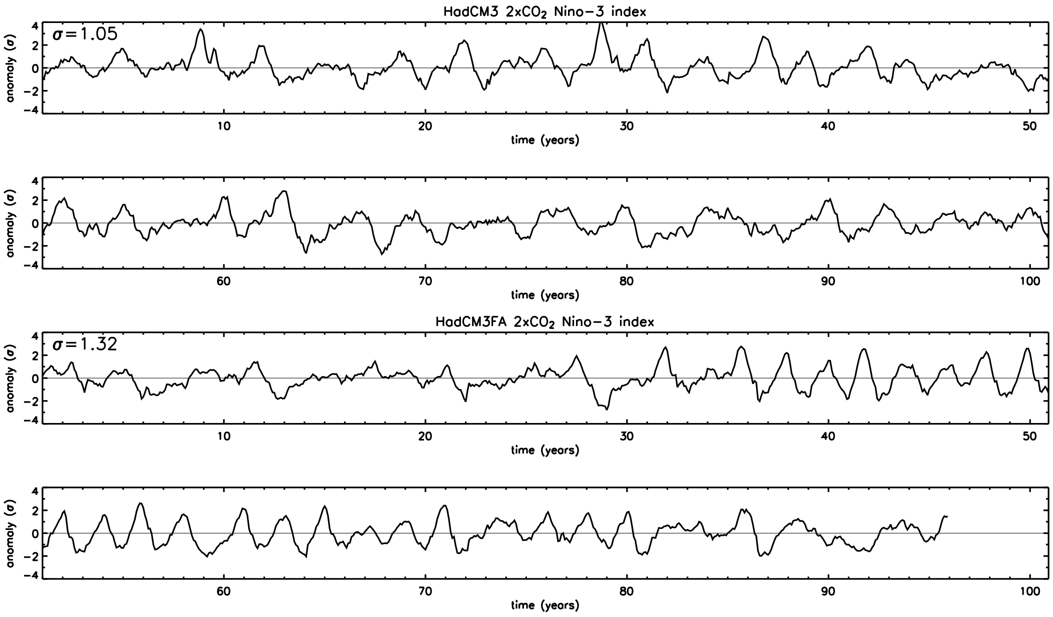

Figure 4.21: Timeseries of seasonally-adjusted Niño-3 SST anomalies in $2 \times CO_2$ scenarios of HadCM3 and HadCM3FA. Standard deviations of the anomalies are also shown.

will be described in more detail in chapter 5.

4.7 Summary

Climate change achieved by doubling carbon dioxide concentration in the HadCM3 GCM had several impacts on the mean climate of the coupled Indo-Pacific system. A slight northward shift in the Somali Jet, accompanied with significant increases in seasonal precipitation in the Asian summer monsoon region amounts to an increase in mean monsoon strength. The increased monsoon precipitation is due to increased moisture availability over a warmer Indian Ocean, and despite El Niño-like warming in the tropical Pacific Ocean. The thermocline response to CO_2 doubling bears a signature of the El Niño-like surface change, being warmed most in the upper east regions, different to the flux correction response. There are also significant increases in precipitation in the ITCZ. The system of limited-area flux adjustments affect the mean climate in the same way as under $1 \times CO_2$ conditions, although the response to greenhouse gas increase in HadCM3FA is stronger in all mean fields, with an increase of nearly 13% in monsoon precipitation.

Whilst the flux adjustment method goes some way to improving the modelled air-sea interaction by reducing erroneous drizzle at low temperatures, the precipitation-SST response is much more dramatically affected by increased $\mathrm{CO_2}$. A higher threshold temperature is required for organized precipitation in the warmer climate.

An increase in monsoon variability is seen at $2 \times \mathrm{CO_2}$, further increased using HadCM3FA. The dynamical monsoon index is noticeably biennial in parts, which is related to behavioural changes in the equatorial Pacific. In the Niño-3 region, the annual cycle is warmed, and variability is increased preferentially in the boreal autumn and winter seasons. Hence the phase locking of ENSO to the annual cycle has increased. Both models feature a stronger ENSO relative to the annual cycle, especially in HadCM3FA where the predominant ENSO oscillation is biennial. The nature of ENSO also seems to have changed, indeed pre-El Niño warm pool extension is more in evidence at $2 \times \mathrm{CO_2}$ in both model versions. HadCM3FA $2 \times \mathrm{CO_2}$ particularly seems to feature an eastward propagating ENSO mechanism, which will be discussed in the next chapter.

Predictability of monsoon dynamics using ENSO predictors is increased with climate change, as is the rainfall over the broad Indian sector. This is less obvious over India itself. The flux adjusted model sees a stronger monsoon-ENSO teleconnection using both measures, as under $1 \times \mathrm{CO_2}$. There is more of a pre-season biennial character to the teleconnections in HadCM3FA, which indicates the crucial link between the biennial monsoon variability and biennial ENSO in HadCM3FA $2 \times \mathrm{CO_2}$. A stronger relationship is observed between Indian monsoon dynamics and precipitation at $2 \times \mathrm{CO_2}$, which is strengthened further with flux adjustments, perhaps due to the increase in biennial behaviour. Flux adjustments increase the teleconnection strength at $2 \times \mathrm{CO_2}$ for the same reason as under $1 \times \mathrm{CO_2}$ conditions, $i.e.$, the warmest waters during El Niño are further east, which shifts the ascending branch of the anomalous Walker circulation.

Finally, the Niño-3 timeseries in the HadCM3FA $2 \times \mathrm{CO_2}$ integration reveals that the biennial character is due to the dominance of a biennial regime lasting some 40 years. Whether the irregular and biennial regimes evident in these data are due to distinct conditions with some shift between them, or whether the biennial part is more likely in the flux corrected model will be examined in chapter 5. Both explanations could have interesting implications for monsoon prediction.

Of course, attention must be drawn to the limitations of the current study. Firstly, a series of integrations at $4 \times \mathrm{CO_2}$ have not been carried out and would provide useful information. May (2004) found that $4 \times \mathrm{CO_2}$ had a much larger, non-linear effect on the monsoon and ENSO system. Comparing $4 \times \mathrm{CO_2}$ and $2 \times \mathrm{CO_2}$, Meehl and Arblaster (2003) noticed a much greater monsoon precipitation response at the higher $\mathrm{CO_2}$ level. Secondly, no consideration has been made here of the effect of sulphate aerosol forcing. This may act to counter some of the impact of increased greenhouse gases such as carbon dioxide, as noted by Ashrit *et al.* (2003). Johns *et al.* (2003) noted a weaker precipitation response in the South Asian monsoon region during an SRES B2 realization of HadCM3 with sulphate forcing.

Chapter 5

Different climatic regimes in a future climate scenario

5.1 Introduction

The previous chapter, whilst providing useful information about the effects of climate change on the monsoon-ENSO system and monsoon predictability in HadCM3 and HadCM3FA, has left further details for examination. That the coupled Indo-Pacific system in HadCM3FA under $2 \times \mathrm{CO_2}$ conditions tends towards a biennially oscillating system raises important questions:

1 Does some event force the regime change from irregular to biennial behaviour, or is the change to biennial behaviour some sort of model adjustment to flux-correction at $2 \times \mathrm{CO_2}$?

2 Why does the flux adjusted model have more features associated with the tropospheric biennial oscillation (TBO) than the un-corrected model?

3 Does different ENSO behaviour impact on the predictability of the Asian summer monsoon?

Figure 4.21b showed that an initial irregular period is followed by several decades of biennial ENSO behaviour, after which irregularity returns. This rules out the idea that the Unified Model ocean may be making some decadal timescale adjustment to the imposition of flux adjustment and leaves open the possibility that two distinct ENSO regimes may be present, the change between which is initiated by some large-scale occurrence. Alternatively, the increasingly biennial behaviour may be just part of a tendency which the model oscillation sometimes falls in to. A combination of both theories may also be possible.

§5.2 details the data selection process used to determine the different regimes, whilst §5.3 looks at the mean climate differences between the two regimes. §5.4 and §5.5 consider the regimes in terms of theoretical and observed ENSO modes respectively. The intraseasonal behaviour is considered in §5.6. The evolution of the tropospheric biennial oscillation in HadCM3FA $2 \times \mathrm{CO}_2$ is detailed in §5.7 whilst §5.8 considers the reasons for the biennial tendency. The impact of the different regimes on monsoon prediction is covered in §5.9. Finally §5.10 details the study of a second realisation of the model integration, before conclusions are drawn in §5.11.

5.2 Regime selection in HadCM3FA $2 \times \mathrm{CO}_2$

The Niño-3 SST timeseries from the HadCM3FA $2 \times \mathrm{CO}_2$ integration in the previous chapter is shown again in Fig. 5.1. A 35-year period of predominantly irregular ENSO behaviour is selected (years 1–35 inclusive), as well as a period during which the biennial oscillation dominates (years 46–80 inclusive). These regimes have been selected to be of equal length, and are highlighted in the figure. That the behaviour in these periods seems reasonably constant allows the usual monsoon and ENSO statistics to be considered for each in turn. Consideration will be given to any obvious trigger factors initiating regime change.

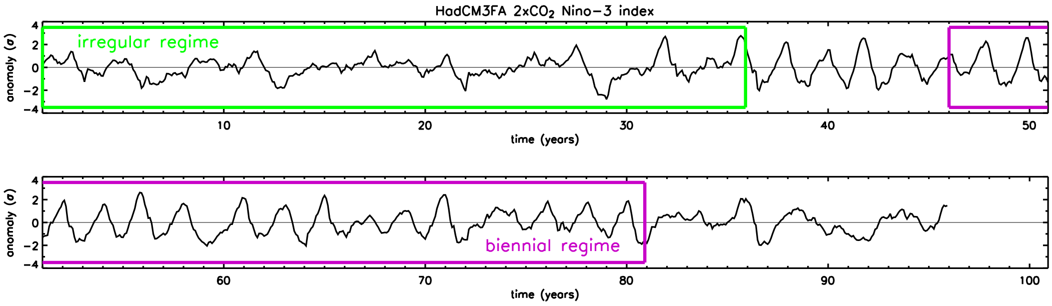

Figure 5.1: Timeseries of seasonally-adjusted Niño-3 SST anomalies in the HadCM3FA $2 \times \mathrm{CO_2}$ integration. The regimes chosen for analysis are indicated: irregular (green) years 1–35 (2560–2594) inclusive and biennial (purple) years 46–80 (2605–2639) inclusive.

5.3 Differences in mean climate and ENSO characteristics

Firstly, let us consider the different mean climate conditions present during the biennial and irregular regimes. Figure 5.2 shows the difference in surface temperature, $850\mathrm{hPa}$ winds and daily precipitation of annual means in the two regimes. A student t-test is used to select significant differences at the 95% level. The central equatorial Pacific of the biennial regime appears cooler, almost in a La Niña-like structure with bands of slight warming to the north and south. The Indian Ocean north of the equator and Indian land surface are slightly cooler, whilst the Maritime Continent is warmer, although not significantly so. The lower tropospheric wind differences in Fig. 5.2b show a significant Gill-type response to the warming of the Maritime Continent waters (Gill, 1980), $i.e.$, both westerly and easterly inflow into the region along the equator. This inflow originates from further across the Pacific Ocean than Indian Ocean. The Maritime Continent warming and increased low-level convergence there combine to give significant increases in precipitation (Fig. 5.2c), of up to $2\mathrm{mm.day}^{-1}$. Although the Indian subcontinent features little precipitation change in the annual mean, summer (JJAS) rainfall over the north west Bay of Bengal and far north of India also see significant increases (up to $2\mathrm{mm.day}^{-1}$, not shown). The mean climate difference of the two regimes, particularly in the surface temperature field, has important repurcussions which will be returned to in §5.6.

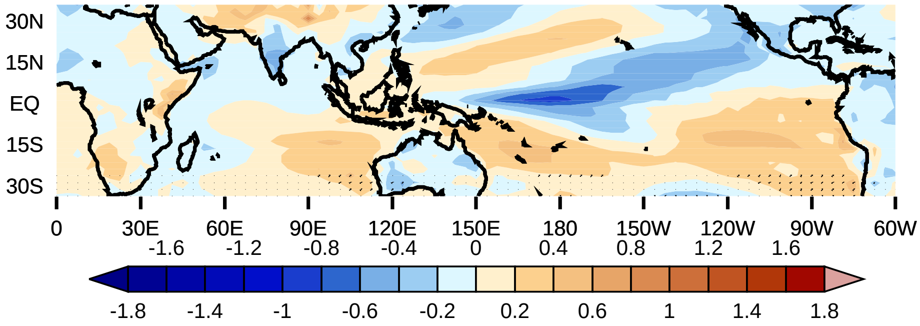
30N
15N
EQ
15S
30S
0
30E
60E
90E
120E
150E
180
150W
120W
90W
60W
-1.6
-1.2
-0.8
-0.4
0
0.4
0.8
1.2
1.6
-1.8
-1.4
-1
-0.6
-0.2
0.2
0.6
1
1.4
1.8

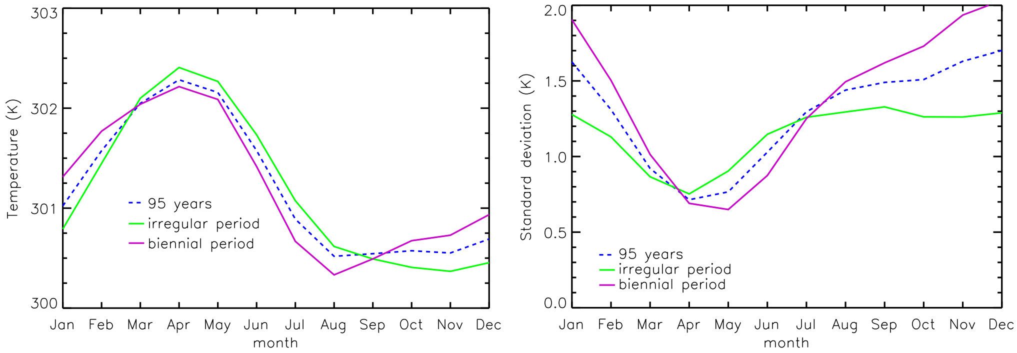

SST seasonal cycle

Cycle of interannual SST standard deviation

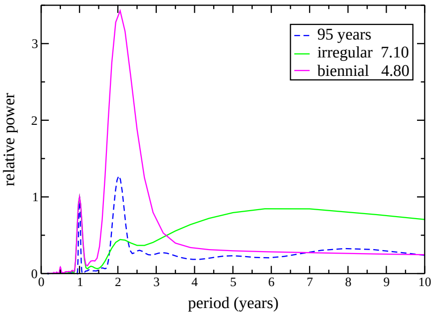

SST power spectra relative to the annual cycle

Figure 5.3: Niño-3 region SST behaviour for the irregular and biennial regimes of HadCM3FA $2 \times \mathrm{CO}_2$. Data for the full integration are also shown. (a) SST seasonal cycle, (b) seasonal cycle of interannual standard deviations, (c) power spectra of SST normalised to the annual cycle, with normalising factors for each regime show in the legend.

Now looking at the east Pacific, Fig. 5.3 shows statistics of the Niño-3 region. Figure 5.3a indicates that the biennial regime seems to undergo a smaller annual cycle in the region than the irregular regime. The month-by-month interannual variability is considered in Fig. 5.3b, where the biennial ENSO oscillation is clearly much more strongly phase locked to the seasonal cycle. The northern winter standard deviation is $1.2°\mathrm{C}$ higher in the biennial regime than during the irregular oscillation. Variability at the spring minima is also slightly lower in the biennial regime, hence there is a greater propensity for El Niño to occur. SPL values (defined in Table 4.3) are $0.49°\mathrm{C}$ for the biennial regime whilst only $0.20°\mathrm{C}$ during the irregular period. These findings are confirmed in Fig. 5.3c where the (biennial) ENSO oscillation is seen to be stronger than the annual cycle for the biennial case, whilst the irregular period features low power across a broad range of ENSO frequencies. Looking at the normalising factors shown in the same figure confirms that the annual cycle is indeed weaker during the biennial, rather than in the irregular regime, consistent with the arguments of Guilyardi (2006) as used in §4.5.

Comparing ENSO correlation statistics for each regime and the whole period (Figs. 5.4 and 4.18b respectively) it is clear that ENSO correlation statistics for the whole period (Fig. 4.18b) are dominated by the large amplitude regular events of the biennial regime (Fig. 5.4b). Surface west-to-east SST propagation is much more obvious during the biennial regime, whilst the irregular period shows more evidence of the warm waters returning to the west after an El Niño. This apparent mode change in ENSO behaviour will be discussed later in this chapter. Given the amplitude of the ENSO during the biennial regime, negative correlations either side of the event peak (October-1 and October$+1$) are very strong, more negative than -0.8. That the strong positive correlations just before an event peak seem to extend further back into the autumn of the biennial data reflects the increased variability at these times of year already noted in Fig. 5.3.

Now looking specifically at El Niño event evolution, the 10 events looked at in Fig. 4.20 are split such that Fig. 5.5 shows 5 El Niño events from each regime. Two facts emerge when comparing the regimes in this way. Firstly, as evident in the timeseries of

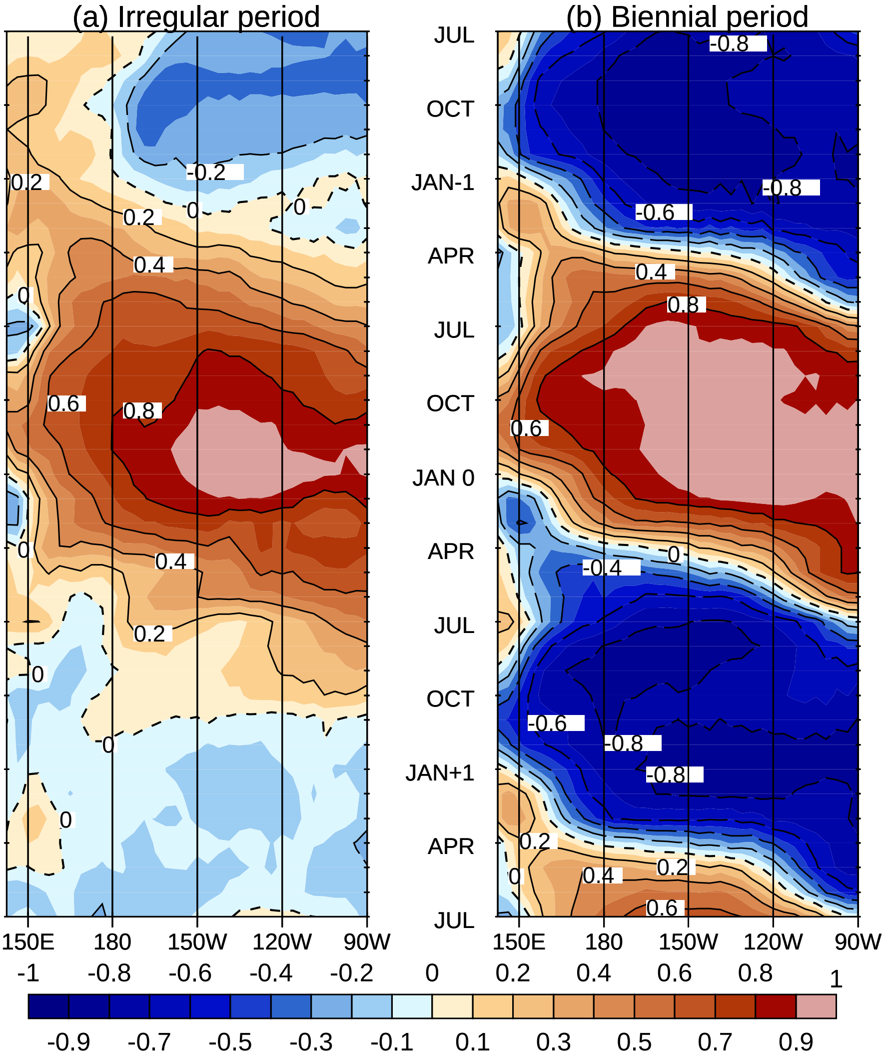

Figure 5.4: Lag correlations between winter season (DJF) Niño-3 SSTs and monthly equatorial Pacific (2.5°N–2.5°S) SSTs in the different regimes found in the HadCM3FA $2 \times CO_2$ integration: (a) irregular, (b) biennial. Negative correlation contours are dashed. Correlations are significant in all but 5% of cases outside of ± 0.34.

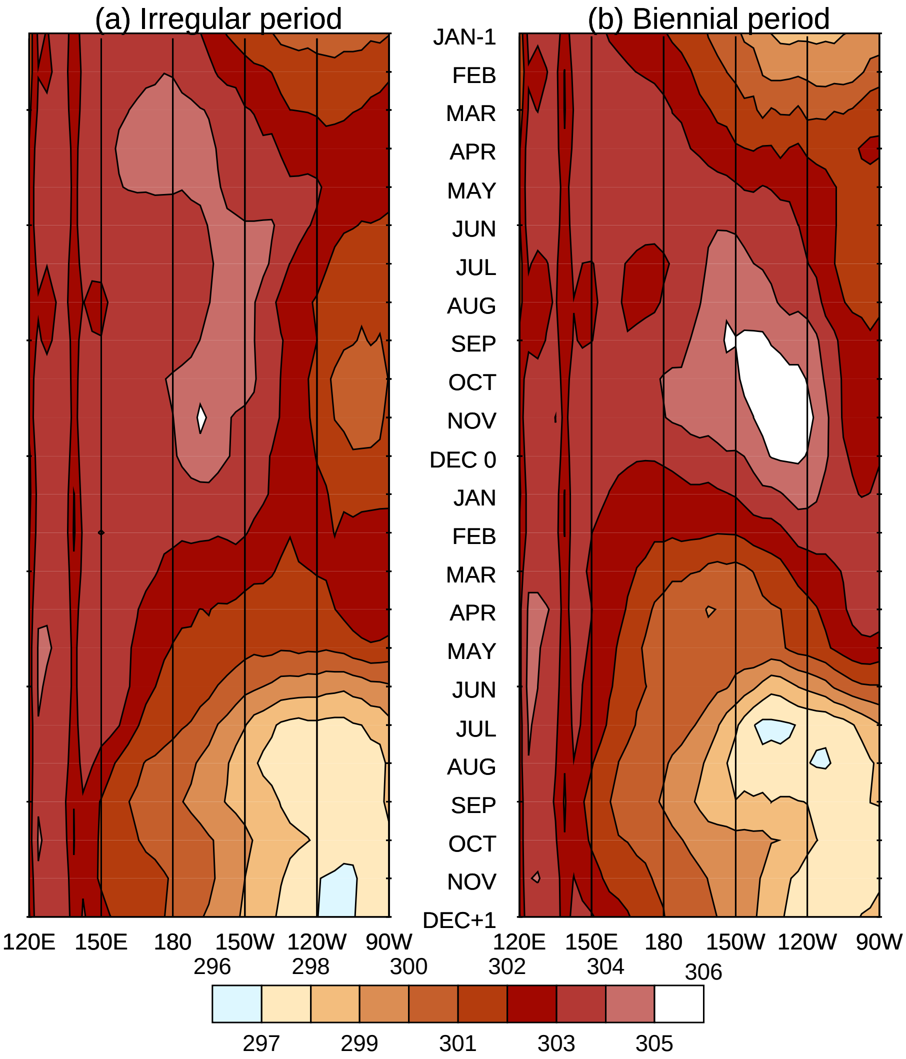

Figure 5.5: Evolution of mean equatorial Pacific SSTs (2.5°N–2.5°S) in a composite of 5 El Niño events in the (a) irregular and (b) biennial regimes.

Niño-3 region anomalies (Fig. 5.1), the biennial El Niño has a much higher magnitude in the mean, exceeding $305\mathrm{K}$ at its peak. Secondly, the peak of El Niño seems to occur further east during the biennial regime than the irregular period. This is not unlike the behavioural difference between the normal and flux adjusted versions of the model seen in Figs. 3.18 and 4.20 for $1 \times \mathrm{CO}_2$ and $2 \times \mathrm{CO}_2$ conditions respectively. That the mechanism of El Niño seems different between the two regimes will obviously impact on the seasonal and climatic predictability of the monsoon, a factor which will be considered later in this chapter.

5.4 The different regimes in terms of simple model ENSO

Jin (1997) uses a simple coupled basin-wide oscillator of the tropical (Pacific) ocean-atmosphere system to explain the low frequency nature of ENSO. The recharge oscillator described incorporates delayed oscillator theory (Suarez and Schopf, 1988; Battisti, 1988) without an explicit time delay. Hence the phase change of the oscillation is governed by recharging and discharging of the thermocline (Zebiak and Cane, 1987), where the equatorial heat content (zonal mean thermocline depth) increases prior to El Niño, and falls (discharges) afterwards. The usual positive (Bjerknes) feedback is included as the growth mechanism. Jin highlights the difficulty in classifying ENSO as a simple oscillator, questioning whether it is a limit cycle perturbed by noise, or a decaying oscillator sustained by noise. These two mechanisms seem to describe the biennial and irregular regimes respectively (Fig. 5.1). The regularity of the biennial regime in HadCM3FA seems to suggest it is analagous to the self-excited limit cycle as in Jin (1997), when the coupling strength is just above the *bifurcation* point. When the coupling strength is not quite as strong, however, the linear solution decays, leaving the recharge oscillator to be excited by short stochastic events exerting wind stresses and heat fluxes on the system.

In Jin's system, coupling strength is specified as a constant of proportionality (b) between zonal wind stress ($\hat{\tau}$) and SST anomaly (T_{E}). Thus $\hat{\tau} = bT_{\mathrm{E}}$. This response can be measured as the best-fit gradient of scatter plots showing the response of zonal surface winds anomalies in the Niño-4 region to Niño-3 SST anomalies, similar to those in §3.5. The gradients for all HadCM3 model integrations and the two regimes are summarized in Table 5.1. Not only do the values indicate increased coupling when the model undergoes flux adjustment, but also when CO_2 doubling is introduced. According to Jin (1997), both these influences would provide a tendency for a limit-cycle type regime. Also note that in the biennial regime, the coupling strength is much larger than during the irregular period. That flux adjustments at a given greenhouse gas concentration or CO_2 doubling in the flux-adjusted model have only limited influence on the coupling strength suggest that the GCM is reaching some intrinsic limit. This level

model	$1 \times \mathrm{CO}_2$	$2 \times \mathrm{CO}_2$
HadCM3	0.74	0.85
HadCM3FA	0.88	0.89
irregular	-	0.80
biennial	-	0.92

Table 5.1: Gradient of Niño-4 surface zonal wind anomalies vs. Niño-3 SST anomalies ($\Delta u'_{10}/\Delta SST'$) for all model integrations and the irregular and biennial regimes. $1 \times \mathrm{CO}_2$ values taken from Fig. 3.13.

is still not as large as that seen in ERA-40 (1.08 from Fig. 3.13). Given that the period shortening seen in the HadCM3FA $2 \times \mathrm{CO}_2$ integration seems to contradict the increase one would expect as atmosphere-ocean coupling strength is increased (Zebiak and Cane, 1987) it is clear that there are competing influences acting on the system in this configuration of the Unified Model, and this point will be further addressed in later sections.

Wang *et al.* (1999) seems to share similar definitions, identifying a stable basic state regime, wherein the coupled dynamics are unable to sustain an oscillation, which is instead triggered by stochastic forcing (much like the irregular regime in HadCM3FA $2 \times \mathrm{CO}_2$). When unstable, an unforced limit cycle is also found, where the dynamics sustain a nonlinear oscillation. In this case the coupled system tends to populate around two extremes, rather like the biennial regime. Again, the air-sea coupling parameter is used to force the coupled system to move from stable behaviour to unstable, limit-cycle oscillations. A critical *bifurcation* value of the coefficient marks the switch between the two regimes. The authors further explain factors which may support the biennial behaviour, and these will be explained in §5.8.

This section has detailed two simple modes which share characteristics with the irregular and biennial regimes of HadCM3FA $2 \times \mathrm{CO}_2$, one which is stable and features irregular ENSO oscillations, the other a limit cycle mode strongly phase-locked to the annual cycle. Jin (1997) further compares these with those observed (*SST* and *basinwide ocean adjustment* modes respectively) and these will be explained in the next section.

5.5 ENSO modes in observations and GCM integrations

Now that the theoretical modes of ENSO have been considered it is useful to look at changes to ENSO behaviour in observations and contrast those with the model integrations.

Neelin *et al.* (1998) summarizes theoretical modes of El Niño. These are found on a spectrum of behaviour, ranging from the delayed oscillator mechanism (Suarez and Schopf, 1988; Battisti, 1988), where the timescale is governed by basinwide oceanic adjustment, to SST modes more closely related to advection and upwelling across the thermocline. A hybrid of these modes forms the basis for observed ENSO behaviour, note Neelin *et al.* (1998), and Federov and Philander (2001) suggest that the composition of the observed mode may vary, being mostly delayed oscillator during some periods and SST mode at other times. The naming conventions for these modes are unified by Guilyardi (2006) in his study of El Niño-mean state interaction in the IPCC AR4 models. The *S-mode* (or SST mode, local mode), is generated by local SST-wind interactions in the central and east Pacific and features surface east-to-west propagation of SST anomalies. Secondly, the *T-mode* (or thermocline mode, delayed oscillator mode, remote mode), develops through a feedback between remote winds and the equatorial thermocline. This encompasses the west Pacific and features subsurface eastward propagation. The modes may also be referred to the fast-wave and fast-SST limits of Neelin *et al.* (1998) respectively.

Trenberth and Stepaniak (2001) introduce a useful tool for considering El Niño mode evolution in timeseries. Their *trans-Niño index*, (TNI) puts a value on the SST gradient across the equatorial Pacific basin. This is defined as the difference between the normalised SSTs in the far east and west Pacific, using the Niño-1+2 (0–$10^\circ\mathrm{S}$, 90–$80^\circ\mathrm{W}$) and Niño-4 ($5^\circ\mathrm{N}$–$5^\circ\mathrm{S}$, $160^\circ\mathrm{E}$–$150^\circ\mathrm{W}$) regions respectively. Thus

$$\mathrm{TNI} = \mathrm{SST}_{\mathrm{N1+2}} - \mathrm{SST}_{\mathrm{N4}}. \tag{5.1}$$

Trenberth and Stepaniak (2001) then use the Niño-3.4 series to represent the average equatorial SST in the Pacific, but here we use Niño-3, in common with the rest of this study. (Being only slightly further east, the choice of Niño-3 makes no qualitative difference to the results.) Both indices are normalized, and then the TNI is lag-correlated with Niño-3. As one is effectively the sum of SSTs along the equator and the other the gradient, at zero lag they will be orthogonal. Repeating the observational analysis of Trenberth and Stepaniak (2001), Fig. 5.6 shows the lag-correlation of the TNI with Niño-3 in HadISST, through a 12 year (145 month) moving window. Zero-lag correlations are indeed very close to zero. The complicated nature of this figure requires some explanation, and so consideration will be given to hypothetical eastward and westward propagation of SST anomalies. In both cases, we assume that Niño-3 peaks at the calendar year end, as in observations.

Eastward A few months before the Niño-3 peak (negative lag) positive SST anomalies lie in the central Pacific, whilst the far east has not yet started to warm. Thus TNI is negative in Eq. (5.1), but with a positive tendency as time progresses. Niño-3 however is peaking, and thus will have a negative tendency. So at negative lags (when TNI leads Niño-3), a negative correlation indicates eastward propagation, or T-mode behaviour. The sign of correlation is reversed for positive lags.

Westward By a similar argument, TNI is positive with a negative tendency at negative lags, whereas the warm Niño-3 peak also has a negative tendency. This yields positive correlations and indicates westward phase propagation.

We are now in a position to analyse Fig. 5.6. Prior to the late-1970s, the correlation suggests westward propagation, which Guilyardi (2006) relate to the S-mode. After the late-1970s, Niño-3 leads the TNI and the T-mode is prevalent. The figure offers further clues to properties of these El Niño mode, those in the early period being of low amplitude (see also the Niño-3 timeseries of ERA-40 in chapter 3, Fig. 3.11), whereas the T-mode events encompass large El Niños such as 1982–83 and 1997–98, predominantly confined to the east Pacific. A change in El Niño period is very evident, being 2– 3 years in the early period and 4–5 years after the late-1970s. (This can be measured as the time in lag-months between two bands of postive correlation at a given year.) Timmermann (2001) also explains this change in ENSO behaviour as due to a change in ocean dynamics. Trenberth and Stepaniak (2001) cite evidence for an abrupt

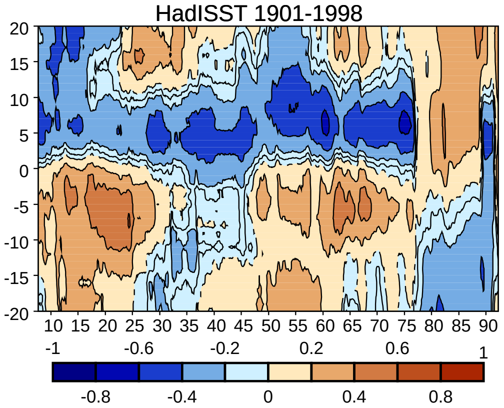

Figure 5.6: Lag-correlation of the trans-Niño index (TNI) with Niño-3 SST anomalies in the HadISST observational dataset from 1901–1998. See text for index definitions. A 12 year (145 month) moving window is applied to smooth the data. Negative lags refer to TNI leading Niño-3.

change in the circulation climate over the tropical Pacific coinciding with the shift from mainly westward to mainly eastward propagating El Niño events in the late-1970s.

Now to put these modes in the context of climate change, flux adjustments and our different regimes, Fig. 5.7 shows the same lag-correlation for each of the model integrations. Whilst there may be some concern about evaluating the Niño-1+2 index (coastal waters) in coarse resolution GCMs such as HadCM3, its choice makes no qualitative difference to the results. Remember that unlike HadISST, each model integration features fixed $\mathrm{CO_2}$ concentrations. El Niño behaviour seems to become more T-modal when $\mathrm{CO_2}$ is doubled, concurring with Guilyardi (2006) who noticed the finding over several models in the IPCC AR4 simulations. This behaviour is noted here irrespective of flux-correction: Figs. 5.7c,d show more positive correlations at positive lag-times than their $1 \times \mathrm{CO_2}$ counterparts (Figs. 5.7a,b). The introduction of flux adjustments also seems to promote T-modal El Niño behaviour, although to a lesser degree than climate change. Unlike observations, however, the T-mode in the HadCM3 future climates tends toward a 2 year period, a fact which is immediately obvious in Fig. 5.7d, dominated as it is by a long regime of large, biennial El Niño-La Niña events. The ENSO mode change was seen previously in Fig. 5.4, where the biennial regime shows clear evidence of eastward propagation, a key characteristic of the T-mode. The behaviour beneath the ocean surface (not shown) indicates that eastward propagation of

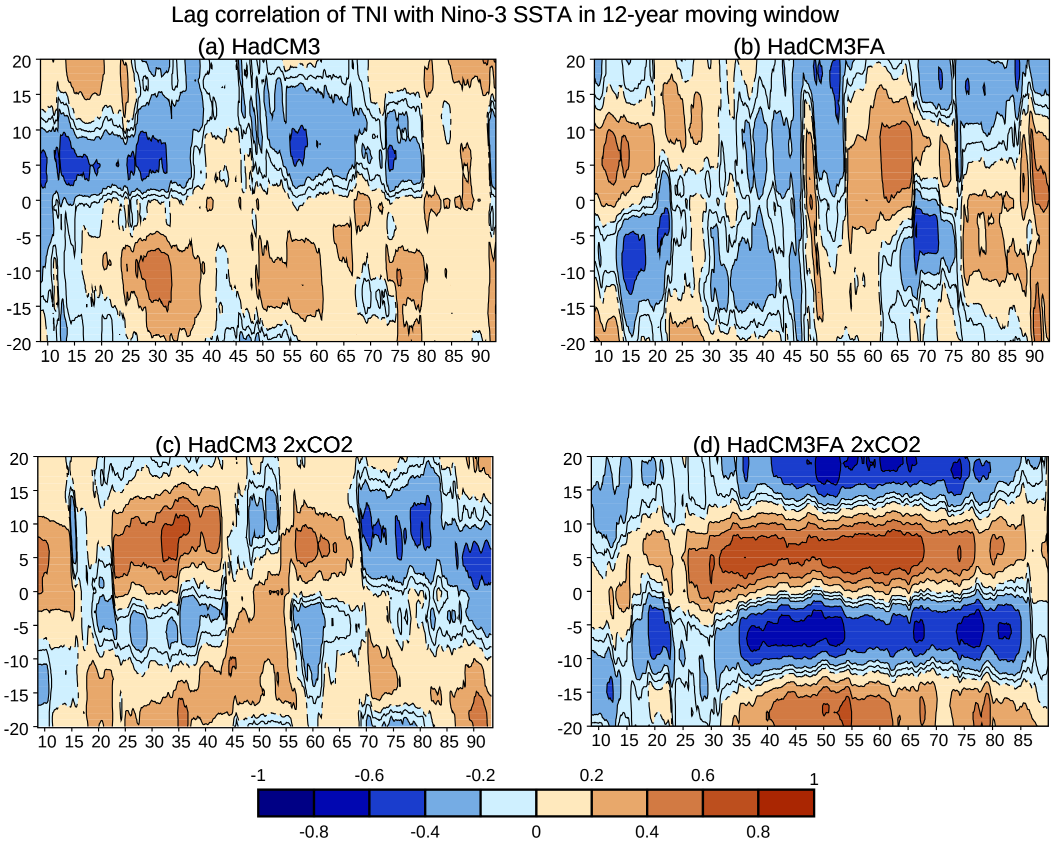

Figure 5.7: As Fig. 5.6 but for the HadCM3 and HadCM3FA model integrations at $1 \times CO_2$ and $2 \times CO_2$. Note the different x-axis scale for the HadCM3FA $2 \times CO_2$ data.

depth anomalies along the thermocline (represented by the $20°C$ depth) is much more uniform and organized during the biennial regime of HadCM3FA $2 \times CO_2$. The tendency for T-mode behaviour is accompanied by an increase in amplitude, concuring with observed mode behaviour. That GCMs such as HadCM3 can exhibit evidence of the hybrid mode at all is a good sign that it can represent some of the mechanistic changes that occur as greenhouse gas concentration increases, says Guilyardi (2006).

In a theoretical study based on the Zebiak-Cane model amongst others, and using real measurable quantities as variable parameters, Federov and Philander (2001) show that for a given mean thermocline depth, weakening of the climatological trade winds can lead to a preference for T-mode behaviour. If the thermocline depth is relatively moderate, a weakening of the mean wind (over decadal, not El Niño timescales) deepens the thermocline in the east, and leads to the dominance of vertical movements of the interface over zonal advection and entrainment terms in their SST equation. Hence the T-mode makes up more of the hybrid of ENSO modes, lengthening the period of oscillation. We already know from §4.5 that mean trade wind response of HadCM3 to both $\mathrm{CO_2}$ doubling and equatorial flux correction is a weakening, given similar mean thermocline depths (Figs. 3.4 and 4.11). This serves both to increase El Niño amplitude (Guilyardi, 2006), and favour the delayed oscillator (Federov and Philander, 2001), which explains the increased likelihood of T-mode El Niño seen in Fig. 5.7.

Looking specifically at Fig. 5.7d, the HadCM3FA model at $2 \times \mathrm{CO_2}$, with its short period, clearly represents the T-mode in a different way to observations. The early part of the integration also features some overlap of positive correlations at both lag and lead times. This could relate to the highly irregular nature of ENSO during this irregular regime. The difference in trade wind strength between the irregular and biennial regimes shown in Fig. 5.2b is possibly consistent with more T-mode behaviour during the biennial regime, the weaker trades in the east Pacific serving to decrease the thermocline tilt there. This signal is not uniform across the basin however. A look at the interannual standard deviation of equatorial Pacific Ocean SST (not shown) in each of the regimes indicates there to be no movement in the variance maxima, both heavily concentrated in the central Pacific. The absolute maximum SSTs do reach further east in the T-mode El Niño events, however, as shown in Fig. 5.5b.

The arguments presented here and in §5.4 highlight the inconsistencies between observed and modelled behaviour, given the competing tendencies of a limit cycle and a T-mode with its longer period, and a biennial oscillation at the same time. One would not expect basin-wide modes such as the thermocline mode to be correctly represented in GCMs such as HadCM3 however. The relatively coarse resolution at the equator (1.25° in the ocean component) would lead to poorly resolved ocean wave dynamics, seriously impeding accurate transmission of heat and depth anomalies along the equator in the form of downwelling Kelvin waves. This failure of wave propagation would impact on the T-mode period, controlled by wave reflection at the western boundary and subsequent adjustment of the thermocline.

Different simple and GCM-simulated modes of El Niño evolution have been considered here, and reasons for tendency of HadCM3(FA) towards them have been hypothesized. The next section will consider intraseasonal behaviour in the two regimes and its application to simple and observed modes.

5.6 Intraseasonal character of the two regimes

Now that the ENSO properties of each of the two regimes have been considered, some of their intraseasonal characteristics will be analysed, and contrasted with what would be expected in the idealised modes.

An indication of the synoptic-timescale activity is given by westerly wind events (WWEs), as in chapter 3. The wind events are defined as separate occurrences over a given threshold speed lasting for at least 5 days. Here the number of events is shown per decade in each of the regimes and the total integration in Fig. 5.8. The integration features more WWEs during the irregular regime, partially consistent with the idea of a stable basic state with un-sustained oscillations triggered by stochastic forcing (Jin, 1997; Wang *et al.*, 1999). The biennial regime, on the other hand, features far fewer WWEs, even at relatively high threshold speeds of $> 5\mathrm{ms}^{-1}$. The ideas of a self-excited or unforced limit cycle during the biennial period would suggest that WWEs are not neccesary for El Niño development during this period. Jin (1997) however does not suggest there should be fewer WWEs during the limit cycle, rather that they are not required for El Niño devlopment.

In observed events, such as the largest El Niño of the twentieth century (1997–98), Lengaigne *et al.* (2002) show WWEs in March 1997 to be instrumental in the development of the phenomenon. Their study uses the OPA8 ocean model forced by observed wind stress over the recent period. The relatively high resolution (up to 0.5° meridionally at the equator) allows good representation of the wave dynamics involved in the development of this event, which is classified as T-modal. Hence whilst the simple limit cycle and T-mode theories of El Niño behaviour have some similarities, they are not identical, and this difficulty is further compounded by coarse resolution in

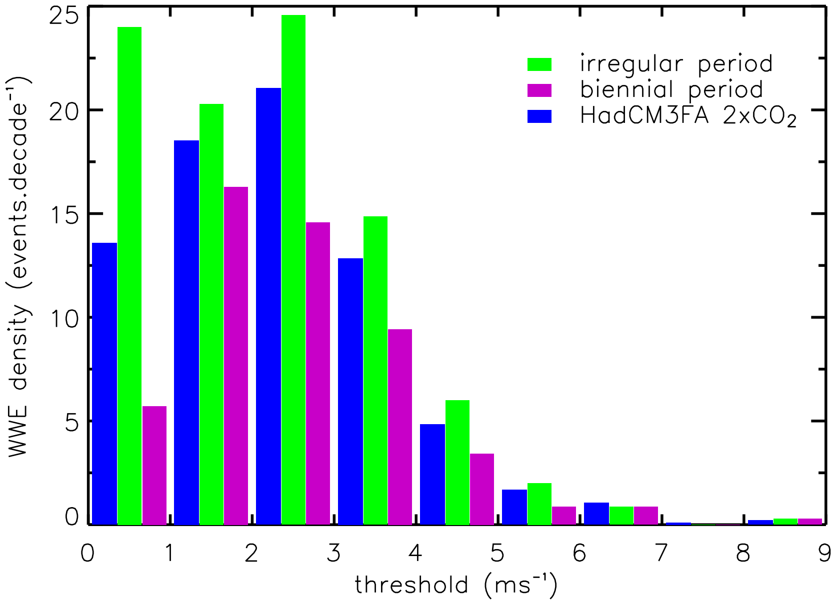

Figure 5.8: Number of westerly wind events exceeding the given threshold in the (148.175–178.175°E, ±1.25°N region of the west Pacific. Results are shown for the whole integration, as well as each regime. Counts per decade are given.

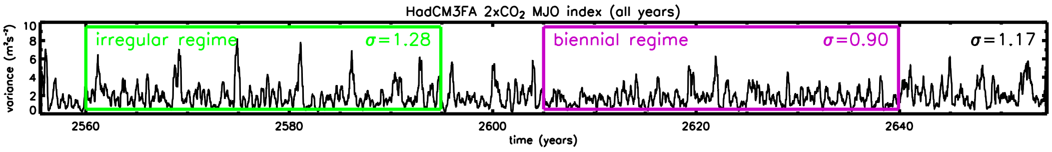

Figure 5.9: Time variance from the zonal mean zonal wind in the equatorial band (±11.25°N) at 200hPa for the HadCM3FA $2 \times CO_2$ timeseries. The daily data is bandpass filtered between 20–100 days and a 101-day moving average is applied. The standard deviation is also marked for the total series and each regime.

HadCM3.

Moving on to intraseasonal behaviour on a slightly longer timescale, we will now consider the prevalence of the MJO during the different regimes. Figure 5.9 shows a timeseries of the MJO index for the HadCM3FA $2 \times CO_2$ integration. The index was devised by Slingo *et al.* (1996) to show the modulation of upper tropospheric zonal-mean wind at the equator, as a measure of MJO activity. The index is the square of the upper tropospheric (200hPa) zonal wind anomaly. The zonal wind time anomaly is meaned zonally and in the latitudinal band ±11.25°N, before being passed through a 20–100 day bandpass filter. A 101-day moving window is then used to smooth the data. As Fig.

5.9 shows, MJO activity seems supressed during the biennial regime of HadCM3FA $2 \times \mathrm{CO_2}$. This is reflected in the standard deviation of the two regimes, being 1.28 and $0.90\mathrm{m^2s^{-2}}$ for the irregular and biennial periods respectively. The irregular regime seems to contain periods of MJO activity of comparable magnitude to those found in observations of the last few decades (Slingo *et al.*, 1999; Inness *et al.*, 2003). We can look at observational evidence of MJO activity and the climatic differences between the two regimes to help explain the fall in MJO activity between the two. Earlier in Fig. 5.2a, a tendency for a cooler equatorial Pacific climate, and a warmer, confined warm pool was observed during the biennial regime. These are conditions not conducive to strong MJO activity as found by Inness *et al.* (2003). Indeed when errors qualitatively similar to these differences (although larger in magnitude) were corrected by equatorial flux-adjustment (Inness *et al.*, 2003), MJO activity increased. Recent analysis in the ERA-40 Atlas (Kållberg *et al.*, 2005, and reproduced in Fig. 5.10) shows MJO activity to be consistently lower during the period 1958–1978 than during 1979–2002. This was also noted by Slingo *et al.* (1999) using NCEP reanalysis, possibly due to decadal timescale warming of SSTs in the tropical Indian and Pacific Oceans. Although there are some concerns regarding the limited data available in the early period, notably the absence of satellite products, this supports the case that T-mode El Niño events after the late-1970s involve the west Pacific in their development. The lack of MJO activity during the T-mode (biennial) period in the HadCM3FA $2 \times \mathrm{CO_2}$ integration reiterates that the modelled system is not properly representing the T-mode.

5.7 The TBO at $2 \times \mathrm{CO_2}$

The tendency for biennial behaviour in the HadCM3FA model, often conflicting with other influences such as the increase in coupling strength and prevalence of delayed oscillator modes of El Niño, is clearly important. A more detailed description of the biennial nature of this integration will be considered here, whilst possible reasons for the tendency will be outlined in §5.8.

We have seen evidence for modelled biennial oscillations in both the east Pacific

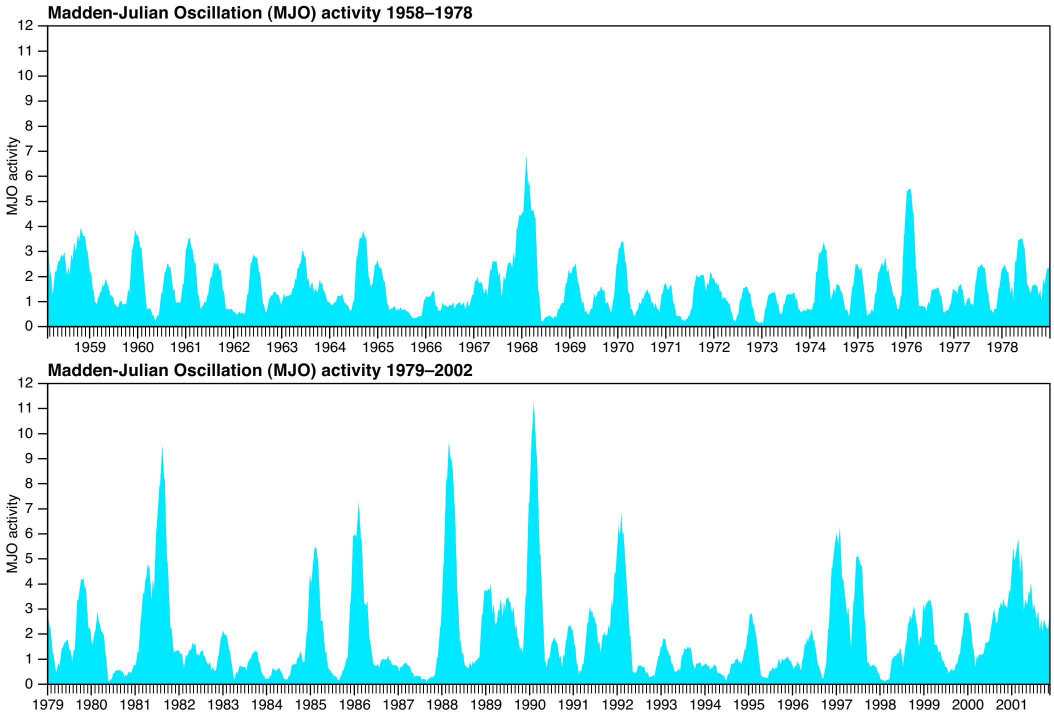

Figure 5.10: MJO index using 6-hourly ERA-40 data. Method similar to Fig. 5.9, although latitude band is ±10°N, and bandpass filter is 30–90 days with a 90-day moving window. Reproduced from the ERA-40 Atlas (Kålberg *et al.*, 2005).

(Fig. 4.21b) and the Asian summer monsoon (Fig. 4.7b) using the HadCM3FA $2 \times \mathrm{CO_2}$ simulation. These can be unified by the tropospheric biennial oscillation (TBO), defined as the tendency for the Asian summer monsoon to alternate between relatively strong and weak years, as described in §2.5. Given the evidence of strong biennial behaviour in both the Indian and Pacific sectors using the HadCM3FA $2 \times \mathrm{CO_2}$ data, it is useful to consider the evolution of the TBO in this case.

As the TBO is defined as the flip-flop between strong and weak Asian summer monsoons, there is a subtle difference in the way we can define strong and weak years. Here we are simply interested in a given Asian summer monsoon being strong (or weak) relative to the preceding and following summer monsoon, and so use the method of Meehl and Arblaster (2002b), Loschnigg *et al.* (2003), Meehl *et al.* (2003) and others. Rather than precipitation which other studies predominantly use, the dynamical monsoon index shall be considered here. This should have little bearing on the results given the strong coupling between monsoon dynamics and precipitation in the

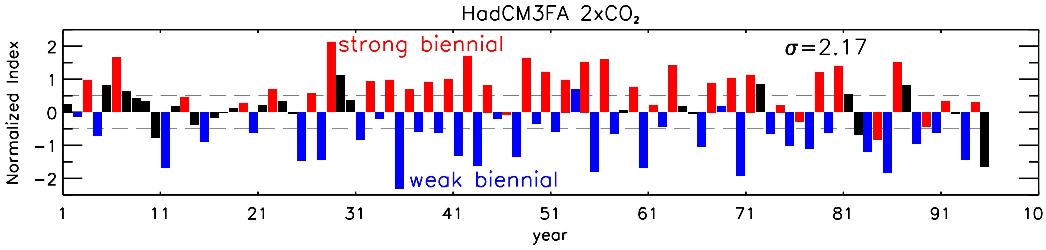

Figure 5.11: The summer (JJAS) dynamical monsoon index for HadCM3FA $2 \times \text{CO}_2$. Here strong (red) and weak (blue) TBO monsoon years are indicated, as defined in Eqs. (5.2, 5.3). The $\pm 0.5\sigma$ lines are dashed.

HadCM3FA $2 \times \text{CO}_2$ simulation. So a relatively strong monsoon year is defined as

$$\text{DMI}_{n-1} < \text{DMI}_n > \text{DMI}_{n+1}, \tag{5.2}$$

and a weak year:

$$\text{DMI}_{n-1} > \text{DMI}_n < \text{DMI}_{n+1}, \tag{5.3}$$

where DMI_n is the summer (JJAS) dynamical monsoon index for year n.

The DMI timeseries of Fig. 4.7 is reproduced in Fig. 5.11, showing those Asian monsoon summers satisfying Eqs. (5.2,5.3). This selection tool has the advantage of filtering out those monsoons which do not participate in the TBO (black bars in Fig. 5.11). It is clear that the biennial nature of the monsoon system is not confined to those summers previously identified in the biennial regime (years 46–80). The possibility exists, however, for a strong (weak) TBO year to be below (above) the mean. Due to the high variability present in this flux adjusted future climate, this happens only rarely, $e.g.$ year 53.

From Fig. 5.11, we designate a strong (or weak) Asian summer monsoon as year 0. The year surrounding the summer is split into seasonal intervals, from MAM(0); the season before the summer monsoon, through JJA(0), SON(0), DJF(+1), MAM(+1), to JJA(+1), the summer season one year after the original monsoon. Strong and weak 18 month cycles are meaned from the data, and their difference found. This compositing technique is the same as used by Loschnigg *et al.* (2003), and should generate a biennial cycle that incorporates the autumn persistence and spring transition. Figure 5.12 shows the strong minus weak differences of surface temperature, lower tropospheric wind and daily precipitation for the six seasons, and is summarized below. The aim is not to derive quantitative detail from the diagram but collate physical quantities together as the evolution proceeds.

Evolution of the TBO

MAM(0) The Indian Ocean features warming left over from a decaying El Niño in the far east Pacific (orange fill). The central equatorial Pacific is begining to cool (blue fill). There is anomalous rainfall over China (blue contour lines). Anomalously westerlies start to build up in the equatorial Indian Ocean, together with the emergence of strong trade winds in the Pacific. A strong band of precipitation is observed over the Indian Ocean just south of the equator.

JJA(0) By definition, this shows strong minus weak Asian summer monsoon conditions. An anomalously strong south-westerly monsoon flow is observed over India, together with wetter conditions over the peninsula and Bay of Bengal. The strong monsoon leaves its well-known signature in the form of anomalously strong Pacific trades. A developing La Niña, over which there is a large dry anomaly (red lines), lies in the central Pacific, illustrating the strong impact which the Asian summer monsoon has on the Pacific region. The strong monsoon wind forces coastal upwelling off Somalia, cooling the sea surface whilst downwelling allows the waters off Sumatra to warm. This forms an anomalous west-to-east SST gradient; the beginning of a *negative* dipole.

SON(0) The La Niña continues to strengthen in the east Pacific whilst the Indian Ocean mainly cools, allowing for a peak in the Indian Ocean dipole (Saji *et al.*, 1999). A large precipitation anomaly moves south over the warm region near Sumatra, illustrating the persistence of the strong annual cycle through boreal autumn (Wu and Kirtman, 2004). The monsoon jet has moved south again, and the Mascarene high off Madagascar is anomalously strong.

DJF(+1) The persistence continues and is clearly illustrated by the strong Australian mon-

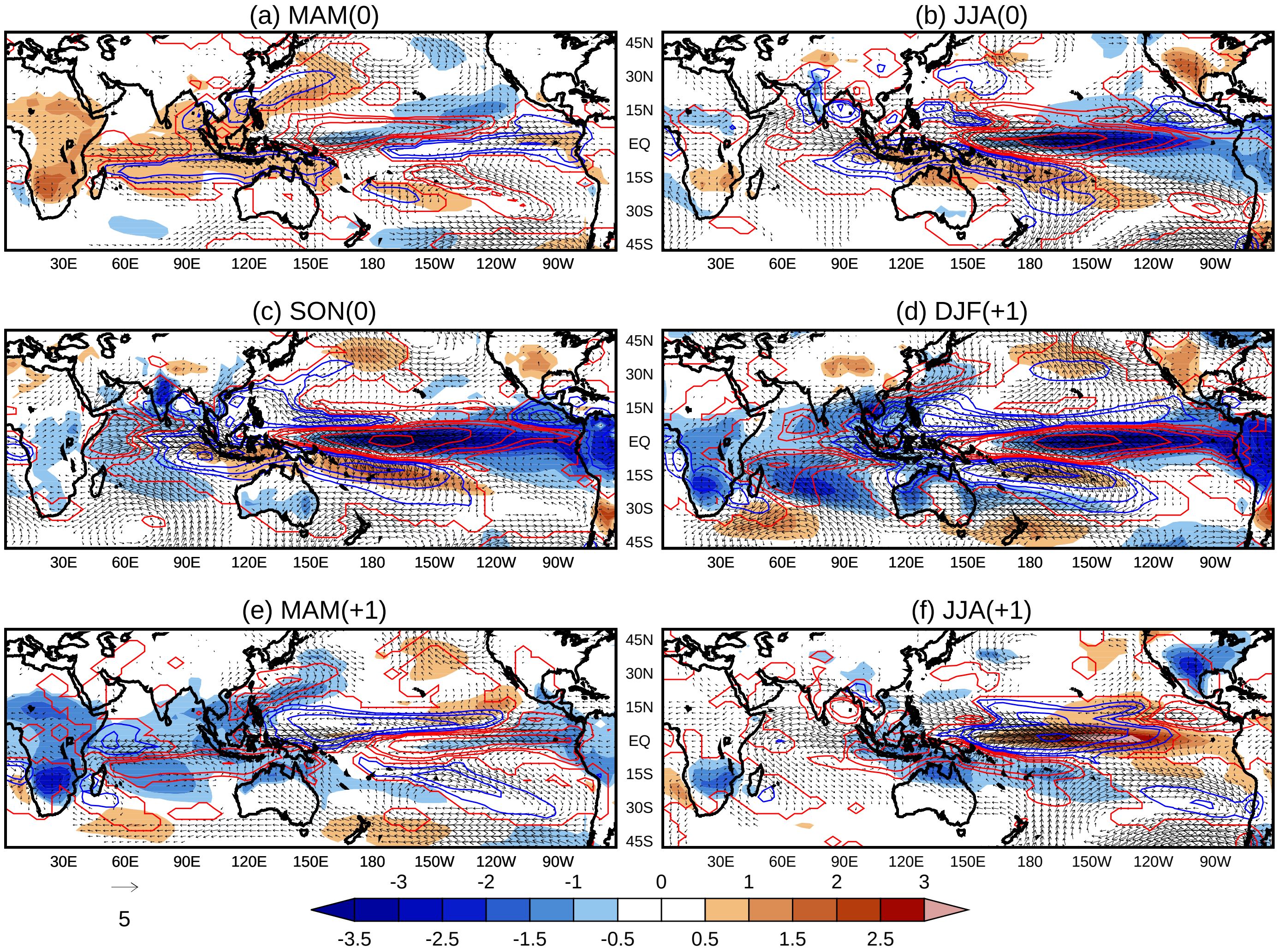

Figure 5.12: Compostite evolution of strong minus weak anomalies in seasons around the Asian summer monsoon (year 0) as selected in Fig. 5.11. Shading indicates surface temperature, values within $\pm 0.5\mathrm{K}$ blanked out for clarity. Winds are at $850\mathrm{hPa}$, unit vector $5\mathrm{ms}^{-1}$. Precipitation shown by blue (wet) and red (dry) contours, levels are 1 2 4 6 8 $16\mathrm{mm.day}^{-1}$. Values above the 95% significance level are plotted.

soon, featuring strong westerlies across the Australian north together with large rainfall anomalies. The boreal winter reversal of the Indian monsoon is clearly evident, easterly flow now crossing the peninsula from over South Asia. A La Niña peaks in the Pacific whilst the Indian Ocean dipole decays.

MAM(+1) In this season of transition (Yasunari, 1991; Meehl and Arblaster, 2001), the Pacific trade winds are seen to weaken in preparation for the forthcoming El Niño. The La Niña still persists, however, in the east. Opposite to the previous MAM season, the developing Indian monsoon winds are anomalously weak. As noted in the composite by Wu and Kirtman (2004), a transition also occurs in the sign of the large precipitation anomaly over the south Indian Ocean. Having been wet (blue) for the previous year, the contours (red) now indicate drying.

JJA(+1) By definition, this shows weak minus strong Asian summer monsoon conditions. The jet pushing over the Indian Peninsula is anomalously weak, and together with the anomalous anticyclone over the Bay of Bengal, leads to dry conditions in those regions. Weak trades couple with an emerging El Niño in the central Pacific.

The coupling of the monsoon and ENSO systems with the Indian Ocean dipole is evident if we look at its timeseries. Saji *et al.* (1999) defines this as the anomaly to the annual cycle of the zonal SST gradient in the Indian Ocean. This is the west ($50°$–$70°\mathrm{E}$, $10°\mathrm{S}$–$10°\mathrm{N}$) minus the east ($90°$–$110°\mathrm{E}$, $10°\mathrm{S}$–EQ), and is shown in Fig. 5.13 for the HadCM3FA $2 \times \mathrm{CO}_2$ integration. The dipole peaks are seen to occur during the boreal autumn, as in observations. There is clear indication of biennial behaviour in the dipole mode, particularly during the part of the integration where ENSO is also biennial. This suggests there is coupling between the monsoon system, the Indian Ocean dipole and ENSO. Saji *et al.* (1999) first thought that the Indian Ocean dipole was independent of ENSO but other studies such as Loschnigg *et al.* (2003) have found this not always to be the case. Indeed glancing at Fig. 5.13 one may make the assumption that as the monsoon-ENSO system becomes more biennial, then the Indian Ocean Zonal Mode becomes more strongly coupled to both the monsoon and ENSO on interannual

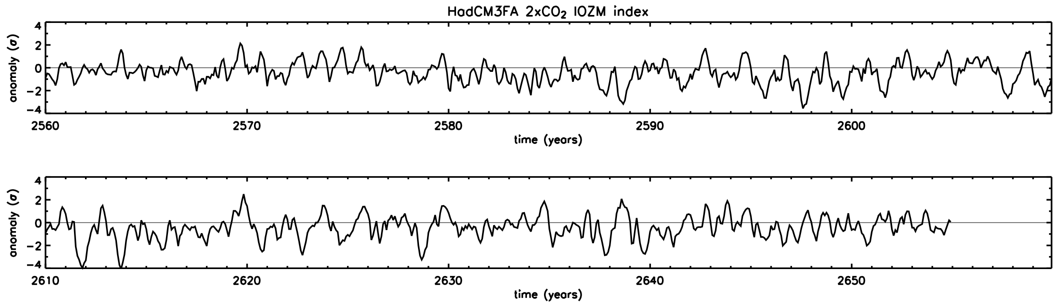

Figure 5.13: Timeseries of seasonally-adjusted Indian Ocean zonal mode (IOZM) anomalies in HadCM3FA $2 \times \mathrm{CO}_2$.

model	IOZM vs DMI	IOZM vs Niño-3	Niño-3 vs DMI
HadCM3 $1 \times \mathrm{CO}_2$	-0.58	0.51	-0.36
HadCM3FA $1 \times \mathrm{CO}_2$	-0.72	0.61	-0.69
HadCM3 $2 \times \mathrm{CO}_2$	-0.60	0.58	-0.57
HadCM3FA $2 \times \mathrm{CO}_2$	-0.69	0.66	-0.82
irregular	-0.58	0.45	-0.79
biennial	-0.74	0.74	-0.85

Table 5.2: Correlation values for (a) IOZM vs. DMI, (b) IOZM vs. Niño-3 SST, and (c) Niño-3 SST vs. DMI. Indices of DMI and Niño-3 SST are JJAS values whilst IOZM is meaned over SON.

timescales. To test this theory, correlations are performed between indices governing the strength of ENSO, the monsoon, and the Indian Ocean dipole. The monsoon and ENSO are most strongly correlated during the summer months and for this reason the DMI during JJAS will be considered, alongside JJAS averages of the Niño-3 index. The dipole mode peaks during boreal autumn and so its SON mean will be correlated with the JJAS values of the other indices. Correlation values for all model integrations as well as the irregular and biennial regimes of HadCM3FA $2 \times \mathrm{CO}_2$ are shown in Table 5.2.

Firstly, looking at the Niño-3 vs. DMI correlations, we note what has already been discussed, $i.e.$, the teleconnection between the monsoon dynamics and east Pacific SSTs is increased both by flux correction and climate change, and preferentially so during periods of biennial behaviour. Now comparing the IOZM vs. DMI correlations, we see that doubling $\mathrm{CO_2}$ concentrations has a limited impact on the relationship, but that equatorial flux correction strengthens the relationship between the monsoon and Indian Ocean dipole. Hence a strong Indian summer monsoon in the flux corrected model is more likely to initiate a strongly negative dipole during the autumn. In some of the doubled $\mathrm{CO_2}$ simulations of IPCC AR4 models, Annamalai *et al.* (2005) notice an increase in the correlation between SSTs west of Sumatra and Indian rainfall, suggesting an increased connection between the Indian Ocean dipole and monsoon. The same models are shown to have no significant bias toward biennial periods in Niño-3 SSTs however (Guilyardi, 2006).

Finally, looking at the relationship between the IOZM and El Niño-La Niña, it is clear that both flux correction and increased $\mathrm{CO_2}$ forcing increase the positive correlation between them. The effect of biennial ENSO behaviour on this correlation is particularly noticeable. Therefore, rather than being independent of ENSO, the Indian Ocean dipole is shown to be reasonably correlated with both aspects of the monsoon-ENSO system, confirming studies by Loschnigg *et al.* (2003) using the NCAR CSM. What is more, as the monsoon-ENSO system takes on more TBO behaviour, the Indian Ocean seesaw becomes more strongly coupled to both the monsoon and to ENSO in the Pacific.

5.8 Reasons for the biennial tendency in HadCM3FA

Now that the biennial tendency of the whole HadCM3FA $2 \times \mathrm{CO_2}$ integration has been considered, possible reasons will be suggested. The literature points to two hypotheses.

5.8.1 Monsoonal forcing

There is some evidence that strong monsoon forcing can cause ENSO to tend to a biennial period. In a study using a stochastically forced nonlinear dynamics ENSO model, Wang *et al.* (1999) found that the monsoon may affect ENSO via a modulation of intraseasonal stochastic forcing, enhancing the biennial component. We have already seen in §5.4 that in an unstable system, the coupled dynamics can sustain a limit cycle. Wang *et al.* (1999) find that intraseasonal noise can reduce the oscillation period, forcing the system to become biennial. They find this intraseasonal forcing to be especially useful when it is modified by the annual cycle in the form of strong monsoon forcing. Further, the noise is better at shortening ENSO period when it is at intraseasonal, rather than synoptic timescales. As stochastic forcing shortens ENSO period, the degree of phase locking to the annual cycle increases, as has already been noted for HadCM3FA $2 \times \mathrm{CO}_2$ in Fig. 5.3b. Studies already introduced in chapter 3 (Li *et al.*, 2001; Kim and Lau, 2001) have also linked monsoon forcing to biennial behaviour. Li *et al.* (2001) find that air-sea interactions over the Indo-Pacific regions need to be quite strong to achieve biennial behaviour, whilst Kim and Lau (2001) found that the key mechanism to the biennial tendency of El Niño evolution was the strong coupling between ENSO and monsoon wind forcing in the west Pacific. In simple model studies they found that introducing strong summer monsoon wind forcing helped initiate ENSO phase change. Thus the imposed monsoon caused the coupled monsoon-ENSO system to become more biennial. Indeed they found that the model ENSO could get locked into a limit cycle with a 2 year period, behaving like a seesaw across the Pacific, with the monsoon acting as a pacemaker. We have already shown in Fig. 4.19 that one of the effects of climate change is to increase the influence of monsoon wind forcing on the ENSO system (the stronger teleconnection), and that flux adjustment only compounds this increase. The stronger ocean-atmosphere coupling described in §5.4 and stronger monsoon forcing of ENSO combine to push the system towards a limit cycle.

5.8.2 Meridional confinement

Several studies cite the importance of the meridional confinement of wind stress in the tropical Pacific to El Niño-La Niña period. Li (1997) notes that positive basin-wide zonal wind stress ($\langle \tau_x \rangle$) on the equator and negative $\langle \tau_x \rangle$ off the equator will lead to a negative tendency in the zonal mean thermocline depth, $\langle h \rangle$. Given that the rate of recharge and discharge of the mean thermocline depth governs the rate of ENSO (Jin, 1997), this implies that increasing the magnitudes of the mean zonal wind stress, or

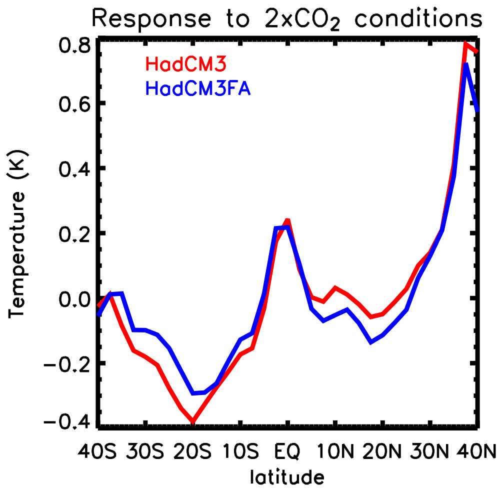

Figure 5.14: The response in zonally averaged (from 120°E to the east coast) SST in HadCM3 and HadCM3FA to increased greenhouse gas concentrations ($2 \times CO_2 - 1 \times CO_2$). The meridional mean (over the domain shown) has been removed for clarity. After Collins (2000b).

confining them, will shorten the period of ENSO. Li (1997) also links stronger upper ocean stratification with a greater growth rate and shorter period. This is possible in this case given the stronger stratification in the flux adjusted model already shown in chapter 3. In his study using HadCM2, Collins (2000a) finds that an increase in the meridional gradient of the tropical Pacific SSTs at $4 \times CO_2$ shortens the period of ENSO, by increasing the rate of recharge and discharge of the thermocline. The same analysis applied here (at $2 \times CO_2$) shows no appreciable difference using this measure. Figure 5.14 shows the zonal average response to CO_2 doubling in both HadCM3 and HadCM3FA. The meridional mean has been removed across the domain. Collins (2000b) confirms that the preferential northern midlatitude warming in HadCM3 (and seen in Fig. 5.14), should not affect ENSO.

Guilyardi *et al.* (2004) states that weak intraseasonal activity and basic state errors can limit stochastic forcing of El Niño, making it more regular. However we have already shown in Turner *et al.* (2005) that the limited area flux correction improve both the basic state errors and the stochastic forcing, so these cannot be the reasons for bienniality in this case. Another reason is suggested, through a series of coupled model tests using atmospheric components of different horizontal resolutions. The width of the wind response is found to relate to ENSO period. Increasing the atmospheric resolution, say Guilyardi *et al.* (2004), increases the meridional extent of the wind response, causing ENSO to oscillate at a more realistic frequency (a longer period). Zelle *et al.* (2005) develops this argument further, finding that the insensitivity of ENSO to greenhouse forcing in the NCAR CCSM model is due to a deficiency in the zonal wind stress response to SST anomalies. The dominant period of Niño-3.4 in their model is 2–4 years, compared to 3–8 in observations, and undergoes no appreciable change during the SRES A1 emissions scenario. They blame the enhanced stability of the Pacific climate and the short ENSO period on the confinement of zonal wind stress. In intermediate coupled model tests of their theory, they show clearly that ENSO period decreases with decreased extent of zonal wind response to SST anomalies. It could therefore be that in HadCM3FA the same conditions prevail. To test this, after Zelle *et al.* (2005), a regression of zonal wind stress versus SST in the Niño regions in both $2\times\mathrm{CO}_2$ integrations is carried out. These are shown in Figs. 5.15 and 5.16 for HadCM3 and HadCM3FA respectively. Increased response is most noted for the Niño-4 region (comparing Figs. 5.15a and 5.16a), indicating not a change in the meridional confinement of the zonal wind stress, but an increased gradient. This response difference is less noticeable for the other Niño regions. A possible mechanism for the influence of a confined wind stress response to SST anomalies back onto ENSO period was suggested by Kirtman (1997). He found that (meridionally) broad wind stress structures led to long oscillation periods. The crucial components were found to be off-equatorial Rossby waves (outside $\pm 7^\circ$ latitude), whose absence in sensitivity tests of a statistical atmosphere coupled to the Zebiak-Cane ocean caused biennial ENSO. Kirtman (1997) describes a mechanism whereby the amplitude of eastward Kelvin waves (which act to cause the change in phase of ENSO) is due to the sum of all Rossby waves at the western boundary.

Changing zonal wind stress is only part of the picture however. Applying flux adjustments in a limited zonal band will impact the total wind stress curl, where the curl is defined as:

$$\boldsymbol{\nabla} \times \boldsymbol{\tau} = \frac{\partial \tau_y}{\partial x} - \frac{\partial \tau_x}{\partial y}. \tag{5.4}$$

Any change in the wind stress curl near the equator should impact on the rate of

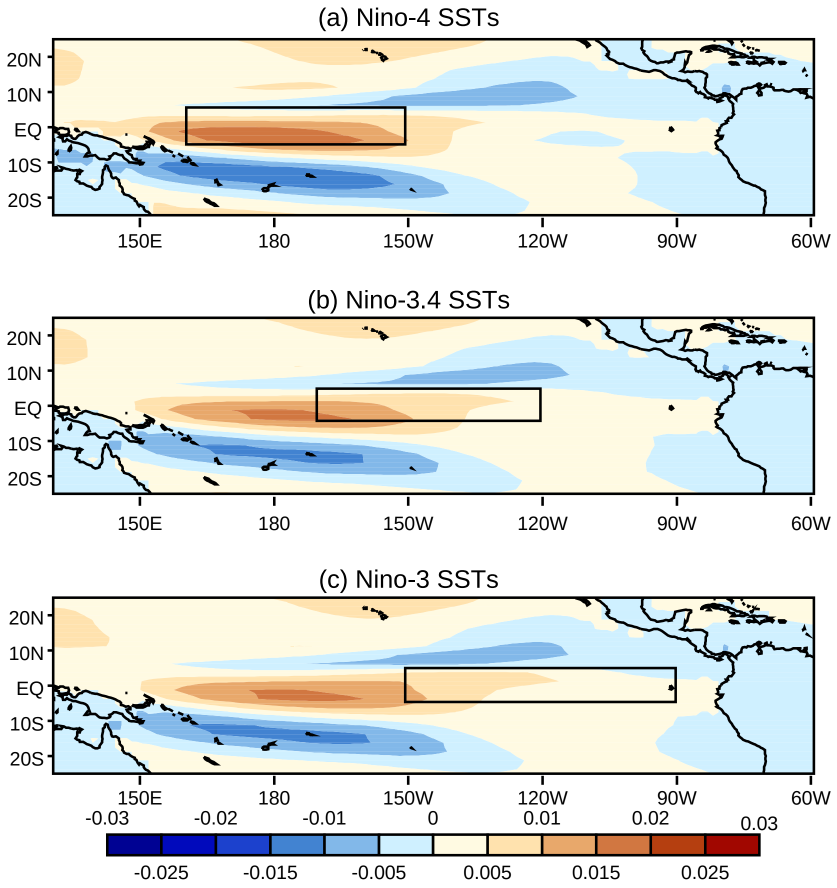

Figure 5.15: Zonal wind stress regressed against SSTs in the Niño-regions for all months in the HadCM3 $2 \times \text{CO}_2$ integration. The boxes indicate the Niño-region used for regression. After Zelle *et al.* (2005).

recharge/discharge of ENSO due to the connection between this curl and Ekman upwelling. Schneider *et al.* (1994) elegantly explain that in the fast-wave limit, the period of ENSO oscillation is in direct proportion to the meridional gradient of the zonal mean wind stress curl at the equator, $i.e.$,

$$\frac{\partial}{\partial t}\langle h\rangle \propto \frac{\partial}{\partial y}\langle \boldsymbol{\nabla} \times \boldsymbol{\tau}\rangle \text{ at } y = 0, \tag{5.5}$$

where $\langle h\rangle$ is the zonal mean thermocline depth (representing heat content of the upper ocean). While the fast-wave limit lies toward the S-mode end of the ENSO spectrum, and the integrations here are increasingly T-modal, a look at this quantity will still prove useful. Figure 5.17 shows the zonal mean wind stress curl in the tropical Pacific basin for both model versions at $2 \times \text{CO}_2$. The meridional variation near the equator is clearly much larger for the flux adjusted model. Thus by the arithmetic of Schneider

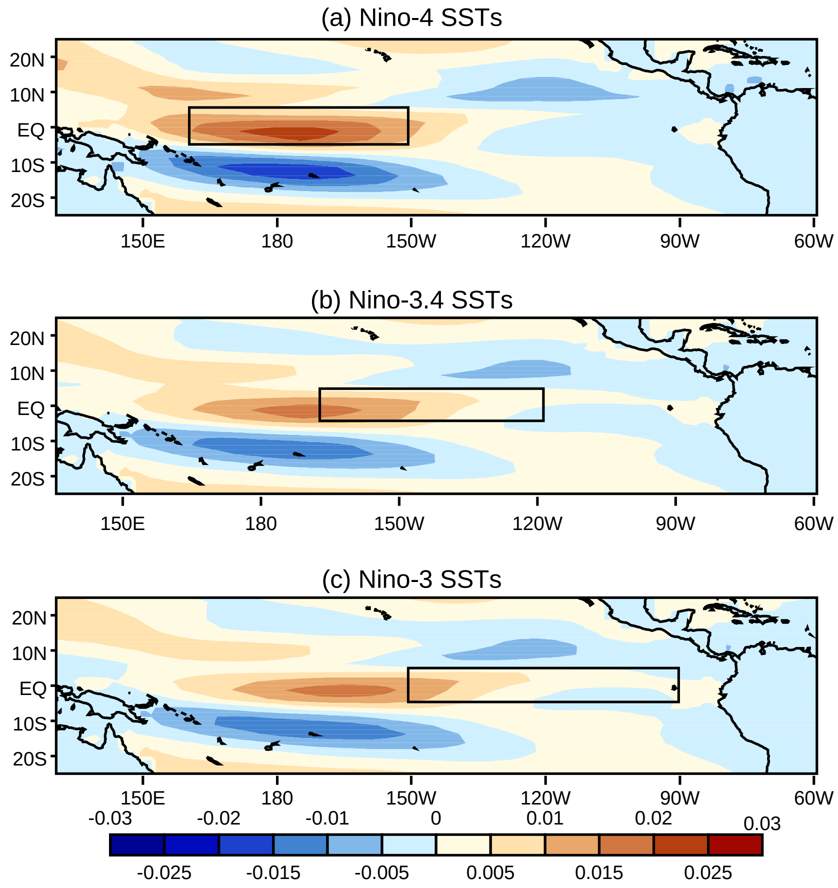

Figure 5.16: As Fig. 5.15 but for the HadCM3FA 2 × CO_2 integration.

et al. (1994), and in agreement with other studies (Li, 1997; Guilyardi *et al.*, 2004; Zelle *et al.*, 2005), the meridional confinement of the wind stress to a narrow band in the Pacific is helping to shorten the ENSO period.

In their study, Wu and Kirtman (2004) found that the COLA coupled GCM exhibited a strong biennial ENSO, possibly due to the strong impact of the Indian monsoon on ENSO in the model (Wu and Kirtman, 2003) or the small meridional scale (Kirtman, 1997). This combination of factors seems the likely contibutor to increased bienniality of ENSO in the HadCM3FA 2 × CO_2 scenario. The flux correction strengthens the monsoon-ENSO teleconnection (as explained in Turner *et al.*, 2005), and climate change further increases this coupling. In addition, the flux adjustment applied in combination with the El Niño-like warming due to climate change preferentially increase the zonal wind stress response on the equator. Hence the wind stress response to ENSO

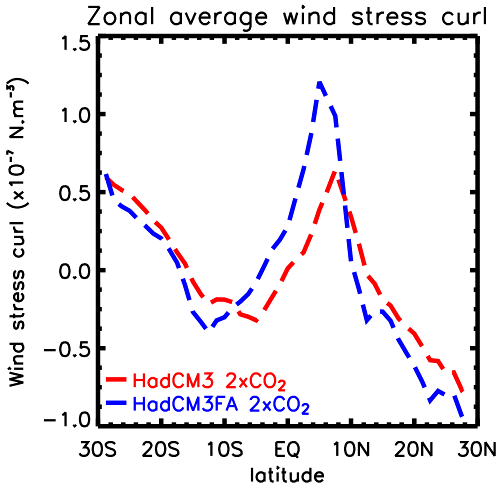

Figure 5.17: Zonal mean wind stress curl in both model versions at $2 \times CO_2$. Zonal mean performed over approximate Pacific region, $120° - 285°$E.

events appear more meridionally confined.

5.9 Implications for monsoon predictability

The most important issue which may arise from the presence of different regimes and the biennial behaviour of ENSO is the impact that these different regimes may have on monsoon predictability. The effect of the two ENSO regimes is shown in Fig. 5.18 for the DMI and Indian rainfall lag-correlated with Niño-3 SST. There is clear indication of a strengthened teleconnection during the biennial regime, although this is not so noticeable in the case of the dynamical index (Fig. 5.18a). The relation between Indian rainfall and east Pacific SST is very weak in the irregular case (Fig. 5.18b), being barely significant. The biennial parts of the integration clearly dominate the curve for the whole integration (blue dashes). This suggests two important points. Firstly, monsoons occuring during a biennially oscillating monsoon-ENSO system are much more predictable. We have already noted in §5.8.1 that strong monsoon forcing pushes the system toward biennial behaviour. Secondly, it is clear from Figs. 5.18a,b that the water cycle of the Asian monsoon region is much more strongly coupled to the monsoon dynamics during a period of biennial oscillation. This is very important because not only does the monsoon become less predictable during irregular ENSO, but even if

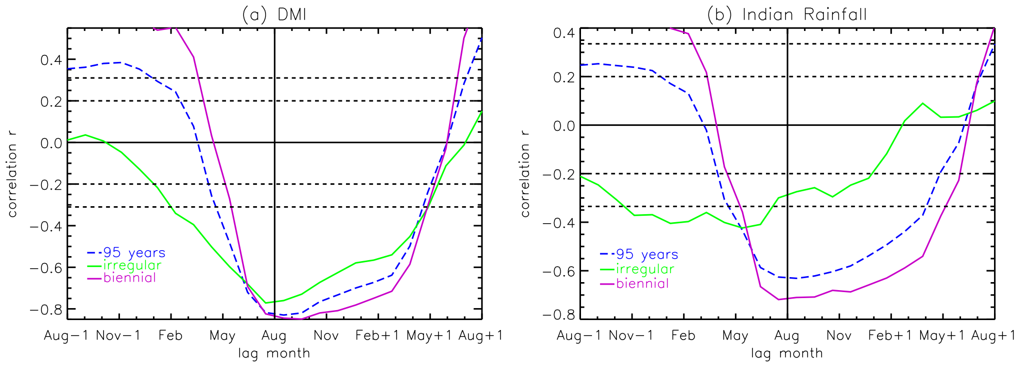

Niño-3 SST vs. DMI Niño-3 SST vs. Indian rainfall

Figure 5.18: Lag-correlation between summer (a) DMI or (b) Indian rainfall against Niño-3 SST. A curve is shown for the full HadCM3FA $2 \times \mathrm{CO}_2$ integration as well as the irregular and biennial regimes. Correlations significant in all but 5% of cases are indicated outside the dashed lines: $|r| > 0.33$ for the regimes and $|r| > 0.2$ for the full dataset.

skilful predictions of monsoon dynamics can be made, they will not necessarily yield consistent precipitation over India. The uncertain relationship between monsoon dynamics and precipitation is illustrated further in the zero-lag correlation between the JJAS dynamic and rainfall indices: 0.31 for the irregular regime and 0.71 for the biennial regime, the former not significant above the 5% level. The whole period was shown as 0.58 in Table 4.4, so again, the biennial part is dominating the statistics.

That the strength of the monsoon teleconnection to the Pacific Ocean varies with changing ENSO regimes links nicely to interdecadal changes in the monsoon-ENSO teleconnection seen in the observed record. Figure 2.10 showed a lag-zero correlation between summer (JJAS) Niño-3 region SSTs from the HadISST dataset and All-India Rainfall gauge dataset. The correlations are performed in a 21-year moving window, to smooth out the effects of large events on interannual timescales. There is clear evidence of decadal timescale changes in the relationship, with a weakening around 1920. Immediately obvious is the decline in the correlation strength between the two systems over the last few decades. Indeed the 1997–98 El Niño was the largest on record yet a normal monsoon prevailed over India, the country receiving 102% of the seasonal average rainfall (Slingo and Annamalai, 2000). Whilst there is some evidence to suggest the recent weakening is associated with anthropogenic influences ($e.g.$, Krishna Ku-

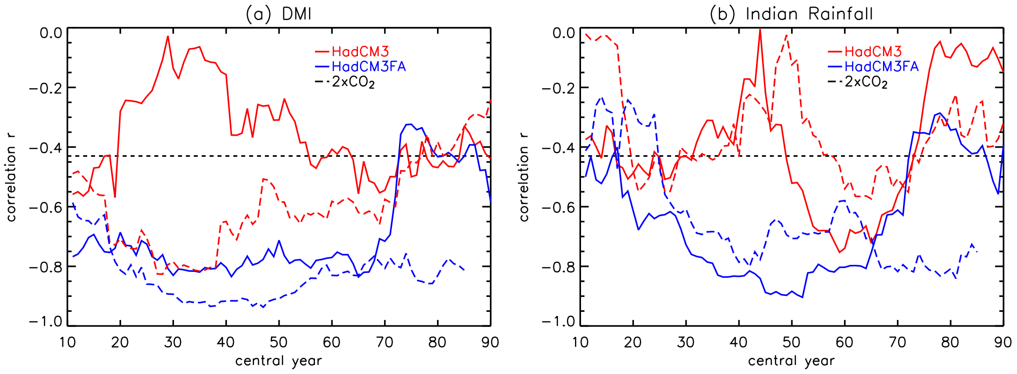

Nino-3 SST vs. DMI

Nino-3 SST vs. Indian Rainfall

Figure 5.19: 21-year moving instantaneous correlation between summer (JJAS) Niño-3 region SSTs and (a) DMI or (b) Indian rainfall in HadCM3 and HadCM3FA integrations at $1 \times \mathrm{CO}_2$ and $2 \times \mathrm{CO}_2$. Correlations are significant in all but 5% of cases when $r < -0.43$.

mar *et al.*, 1999), this is by no means certain and does not explain earlier changes in the record. The change in teleconnection strength may also relate to the change in observed ENSO modal behaviour occuring over the same period. Indeed Slingo and Annamalai (2000) suggest that very strong El Niños such as 1997 may lead to different wind regimes acting on the monsoon system, modulating the local Hadley circulation in such a way as to favour strong monsoon conditions. While some recent studies note that S- and T-mode El Niño events before and after 1976 have quite a different impact on the monsoon (Annamalai and Liu, 2005), others such as Annamalai *et al.* (2005), which includes more recent observations, suggest that the relationship between El Niño and the monsoon may be strengthening again. The authors cite the deficient monsoons of 2002 (-19%) and 2004 (-13%) during moderate Pacific warmings. Either way, the change in ENSO regimes during the HadCM3FA $2 \times \mathrm{CO}_2$ integration impacts on monsoon predictability.

Moving correlations for summer monsoon statistics (JJAS) versus Niño-3 time-series are shown for all model integrations in Fig. 5.19. Most noticeable is the large variation in teleconnection strength through each integration, despite fixed CO_2 concentrations. Correlations are rarely significant using either monsoon measure in the HadCM3 $1 \times \mathrm{CO}_2$ integration due to the poor basic state (Turner *et al.*, 2005). In the flux adjusted models (at $1 \times \mathrm{CO}_2$ and $2 \times \mathrm{CO}_2$) there is also much greater correspondence between the strengths of dynamic and rainfall correlations as noted earlier in this section. Looking specifically at the HadCM3FA $2 \times \mathrm{CO}_2$ curves, noticeable increases in the correlation occur as the biennial regime enters the moving window. A sizable strengthening occurs around year 18 in Fig. 5.19a, and one which is more dramatic around year 25 in Fig. 5.19b, the difference in timing again highlighting the complex relationship between dynamics and monsoon precipitation. As the biennial regime progresses, the teleconnections remain consistently strong.

The other integrations exhibit variations in the monsoon-ENSO relationship that are just as dramatic as in the HadCM3FA $2 \times \mathrm{CO}_2$, without any obvious shift in mean monsoon behaviour or ENSO regimes. It seems that once the monsoon-ENSO system begins oscillating as part of the TBO, the teleconnection becomes much more stable (both Fig. 5.19a,b). The stability of teleconnections over the entirety of model integrations has also been studied by Annamalai *et al.* (2005). These authors used twentieth century CO_2 forcing (transient) simulations and found the GFDL_ CM_ 2.0, GFDL_ CM_ 2.1 and MRI models to have a range of correlation variation similar to that observed. However they noted the moving teleconnections did not match the phase changes in observations (Fig. 2.10), with no noticeable weakening trend.

Whilst recent observed monsoon-ENSO teleconnections seem to have declined, the modelled climate change response has been one of a generally strengthened relationship. The modelled teleconnection is especially strong during the biennial TBO regime, yet ENSO may also be described as T-modal, as in the recent observed record. Hence the conflicting influences apparent in this study of the HadCM3FA $2 \times \mathrm{CO}_2$ integration are likely influencing the monsoon system in different ways. Firstly, although recent observed changes in the teleconnection could be related to changes in the behaviour of El Niño, with the tendency to basin-wide delayed oscillator modes seeming to have less likelihood of causing Indian drought, such modes are poorly represented in the GCM. The coarse resolution in the equatorial ocean will act as a poor wave guide for trapped Kelvin and Rossby waves essential for western boundary reflection and phase change in this mode. Secondly, the tendency to biennial oscillation of the monsoon-ENSO system (TBO) strongly strengthens the teleconnection, and it is clear that this influence is

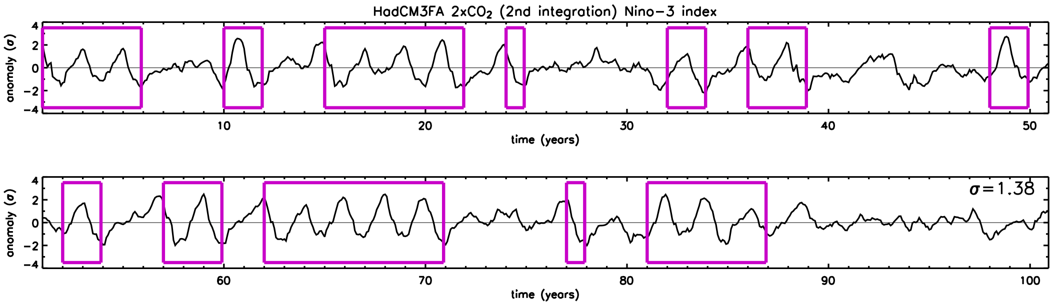

Figure 5.20: Timeseries of seasonally-adjusted Niño-3 SST anomalies in the HadCM3FA $2 \times \mathrm{CO}_2$ [2] integration. Years exhibiting biennial behaviour are boxed.

most dominant in this case in its forcing of the coupled system.

5.10 A second integration of HadCM3FA $2 \times \mathrm{CO}_2$

A further integration of HadCM3FA $2 \times \mathrm{CO}_2$ has been carried out to determine whether the pattern of biennial behaviour is replicated. This integration was generated using an offset in the ocean and atmosphere start dumps, in the same way as the original HadCM3FA $2 \times \mathrm{CO}_2$ run (and described in §4.2). On this occasion the offset was 3 years, (atmosphere starts at 1/1/2552, ocean starts at 1/1/2555). Thus the ocean is initialized from the same point as the previous integration, and the chosen atmosphere gives a different realization of the conditions, rather like an alternative ensemble member in numerical weather prediction, where the initial conditions are perturbed. This second integration will be referred to as HadCM3FA $2 \times \mathrm{CO}_2$ [2].

The Niño-3 timeseries for HadCM3FA $2 \times \mathrm{CO}_2$ [2] is shown in Fig. 5.20. The figure illustrates a system with biennial behaviour, in a slightly different way to the first (Fig. 5.1). Evident are short periods of biennial fluctuations (boxed in purple), separated by irregular oscillations. This further reinforces the suggestions made in §5.4, that HadCM3FA is near some bifurcation point, and tending towards a (biennial) limit cycle. The biennial tendency can be further analysed by comparing power spectra of the two model integrations. A wavelet analysis[1] was performed on the Niño-3 SST

---

[1] Wavelet software was provided at `http://paos.colorado.edu/research/wavelets/` and devised by Torrence and Compo (1999).

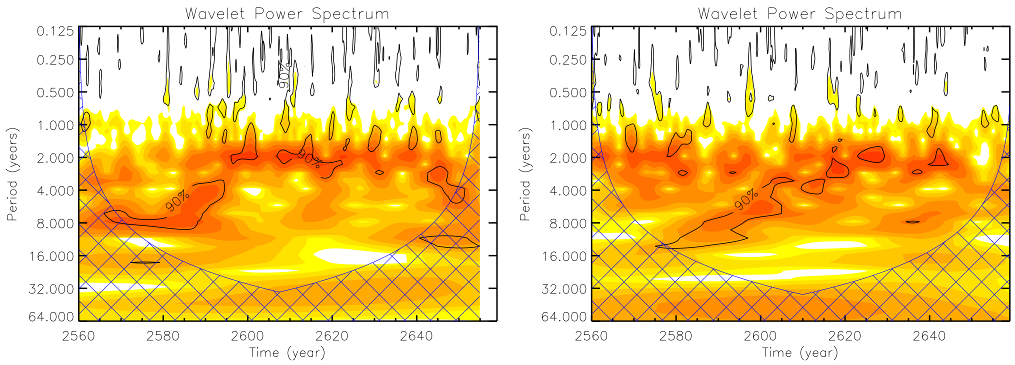

HadCM3FA 2 × CO$_2$ [1]

HadCM3FA 2 × CO$_2$ [2]

Figure 5.21: Wavelet power spectra of the first (95 year) and second (100 year) HadCM3FA 2 × CO$_2$ integrations. Contours displayed are 0.5, 1, 2, 4, 8, 16, $32(°C)^2$. The 90% significant contour is also marked. Hatched regions represent data which should be disregarded due to edge effects at the given period.

timeseries in each dataset, shown in Fig. 5.21. In the early part of the first integration (Fig. 5.21a) there is clear indication of irregular ENSO timescales, peaking between 4–8 years. The biennial regime is then evident, with significant power at 2-year periods, stretching for the rest of the integration. Some longer period oscillation is apparent near the end (around 2645). In the second HadCM3FA 2 × CO$_2$ dataset (Fig. 5.21b), the character is slightly different (as seen in Fig. 5.20), with periods of strong power at 2-year periods interspersed with longer period oscillation.

Now to complete the TBO using information from the Indian sector, the timeseries of the summer DMI for the HadCM3FA 2 × CO$_2$ [2] integration is shown in Fig. 5.22. The monsoons classed as biennial using Eqs. (5.2,5.3) are highlighted in the same way as in Fig. 5.11. Much of the integration features TBO behaviour in the monsoon. As in the first integration, these flip-flop monsoon events are concurrent with but not exclusive to the biennial periods of ENSO. Hence we can infer that the monsoon is the more active partner in the monsoon-ENSO relationship. The brief study of this second integration here seems to reinforce the findings earlier in this chapter, $i.e.$, that the HadCM3FA 2 × CO$_2$ integration has a tendency for biennial oscillation across the coupled monsoon-ENSO system. Both the flux adjustments and CO$_2$ increase contribute to this tendency as described in §5.8.

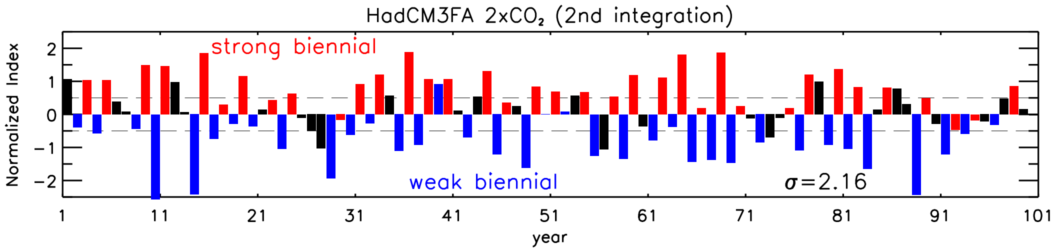

Figure 5.22: The summer (JJAS) dynamical monsoon index for the HadCM3FA $2 \times \mathrm{CO}_2$ [2] integration. Red bars indicate relatively strong monsoons whilst blue bars indicate relatively weak monsoons.

5.11 Discussion

Viewing statistics of the irregular and biennial ENSO regimes found in HadCM3FA under $2 \times \mathrm{CO}_2$ conditions has revealed some marked differences. A smaller annual cycle during the biennial regime, together with stronger phase locking of ENSO to the annual cycle leads to a greater propensity for El Niño events to occur. Eastward propagation is much more obvious during this period, and events are higher in magnitude and peak further to the east, similar to the climate change or flux adjustment responses. The statistics for the biennial ENSO period seem to dominate the whole integration due to their large amplitude.

The two ENSO modes seen in the model seem to fit with those predicted in theory and seen in observations in some sense. Consistent with the recharge oscillator of Jin (1997), a stable irregular mode where ENSO is sustained by stochastic forcing gives way to self-excited limit cycle as the strength of air-sea coupling increases above a bifurcation point. This coupling strength is found to increase with both the application of flux adjustment and doubling of CO_2 concentrations, and is noticeably stronger during the biennial regime. The stable and limit cycle regimes seem applicable to the observed spectrum of ENSO modes, representing SST modes and basin-wide thermocline (T) modes respectively. Tendency to these T-modes is also seen in the model, under both $2 \times \mathrm{CO}_2$ conditions and equatorial flux adjustment. This tendency is explained by a decrease in the strength of mean trade winds across the Pacific Ocean basin, allowing vertical motion of the thermocline to dominate over zonal advection of SST anomalies. In the biennial regime, a mean reduction in the east Pacific trade winds is consistent with this theory. Whilst the favoured direction of anomaly propagation is now eastward and events are of higher amplitude than in the irregular regime, the obvious 2 year period of oscillation conflicts with the longer periods seen in observed cases of delayed oscillator modes reliant on the response of the entire Pacific basin to wave dynamics.

At intraseasonal timescales, westerly wind event and MJO activity is strong during the irregular period, consistent with the stochastic forcing needed to sustain the irregular theoretical mode. However their reduced occurence during the biennial period seems contradictory to observed behaviour such as the implication of WWEs in the onset of recent large events such as the 1997 El Niño. In any case, the colder central Pacific and confined warm pool of the biennial regime are not conducive to intraseasonal phenomena, the very motivation for the original limited area flux adjustment experiments of Inness *et al.* (2003).

The marked biennial tendency of HadCM3FA $2 \times \mathrm{CO_2}$ ENSO is not confined to the Pacific Ocean however, incorporating the Asian-Australian monsoon system as part of the tropospheric biennial oscillation (TBO). Neither is TBO evolution limited to the biennial regime of El Niño-La Niña events, being similar to that observed and in other modelling studies. This includes the (boreal) autumn persistence and spring transition seasons, passing anomalies from the Asian to Australian monsoons and then changing sign the following year. Increased coupling of the monsoon-ENSO system occurs during the biennial regime, incorporating also the Indian Ocean zonal mode (dipole).

The tendency toward biennial oscillation is increased by both $\mathrm{CO_2}$ doubling and flux correction, with two hypotheses put forward for its existence. Strong monsoon wind forcing over the west Pacific has been found in other GCMs to force the ENSO system to favour biennial oscillation. This forcing in the HadCM3FA model, together with meridional confinement of the zonal wind stress response to warming events in the equatorial Pacific (in part related to the applied flux adjustments) are suggested as causes of the tendency to TBO behaviour.

Increased TBO behaviour, with its inherent strong coupling between the Indian and Pacific sectors, leads the HadCM3FA $2 \times \mathrm{CO_2}$ integration to have stronger monsoon-

ENSO teleconnections, especially during the biennial ENSO regime. Also during this period, the relationship between monsoon dynamics and precipitation is more robust, increasing the prospects for greater monsoon predictability during such regimes. All model integrations used throughout the thesis are found to display noticeable inter-decadal changes in correlation between the monsoon and ENSO despite running under fixed greenhouse forcing, suggesting that recent observed weakening in the monsoon-ENSO relationship may not be related to anthropogenic climate change, but a natural internal mode of decadal variability.

The clearest limitation of the study in the chapter is the ability to correctly represent modes of El Niño observed in nature, particularly the delayed oscillator type modes which are reliant on ocean wave propagation and reflection. Poor ($1.25°$) resolution of the ocean model, whilst not prohibiting the transmission of wave-like structures completely, is likely to severely impede their correct temporal and spatial characteristics. This relates to ENSO period both in terms of the propagation time for Rossby and Kelvin waves across the basin, and the proper meridional extent of such waves about the equator.

It now remains to briefly answer the questions posed at the beginning of this chapter.

1 Biennial behaviour is not a spin-up adjustment to the imposition of flux corrections, given that a period of irregular oscillation returns after the biennial regime

2 The HadCM3FA $2 \times \mathrm{CO}_2$ integration displays more features associated with the TBO than other integrations because of a combination of stronger monsoon forcing on the Pacific (related to both the imposition of flux adjustments and increased greenhouse forcing), and increased meridional confinement of the wind stress response associated with warm or cold event in the Pacific Ocean.

3 Biennial oscillation in ENSO as part of the TBO strongly increases the prospects for skilful monsoon prediction.

Chapter 6

Conclusions

This chapter presents the main conclusions drawn from the work involved in producing this thesis. Detailed conclusions have been made at the end of each chapter and so they will only be summarized briefly here. §6.1 will outline these conclusions and address the specific aims and questions raised in the introduction, chapter 1. Limitations of the work will be discussed in §6.2, covering experimental drawbacks and model improvements which could be made. In §6.3, possible experiments will be suggested which could address some of the issues still unresolved by this thesis, and extend the work done within.

6.1 Summary of major results

The coupled GCM studies presented in this thesis have focused on two major aspects of the simulated monsoon-ENSO system. Firstly, the role of systematic errors in the tropical Indo-Pacific oceans on the monsoon system has been considered. Partially removing such errors from the control climate has been found to significantly improve the strength and timing of teleconnections between the equatorial Pacific and Indian monsoon region. This increases the predictability of the monsoon.

Secondly, the important question of future changes to the monsoon system has been studied. Whilst the Pacific Ocean undergoes El Niño-like warming in the doubled CO_2 simulations, the GCM used here presents statistically significant increases in monsoon precipitation. Teleconnections are not found to weaken as in some other studies.

Further work has married the two main foci, giving some estimate of the way in which the systematic errors present in the control climate could affect future estimates. Removing the same systematic errors as in the control integration yields a greater response to climate change for most parameters. Some interesting monsoon-ENSO changes are observed in GCM integrations of the future climate with errors removed, which suggests a tendency towards biennial (TBO) behaviour.

What is the effect of systematic errors in a coupled model on representation of the monsoon system and its predictability?
Systematic errors have been found in the mean climate of the HadCM3 coupled GCM, in common with many other coupled models. These are particularly large in the tropical Pacific Ocean and constitute a coupled mechanism of biases in SST, low-level winds and precipitation (Inness *et al.*, 2003). Given that accurate monsoon prediction depends on the consideration of low-frequency variations in lower boundary forcing (Charney and Shukla, 1981), and that those mean climates which are better simulated result in more realistic interannual precipitation anomalies (Sperber and Palmer, 1996), the flux adjustment method of Inness *et al.* (2003) was used to relax SSTs in the equatorial Indo-Pacific regions back to climatology. These were of high enough magnitude to constrain the mean climate but small enough to allow the system to undergo natural variations.

The flux adjustments reduced the cold bias in the central Pacific and confinement and overheating of the west Pacific warm pool. Associated with this are reductions in the strength of the mean trade winds and south-westerly monsoon flow. The summer precipitation climate looks much more realistic, especially over the Maritime Continent and equatorial Indian Ocean.

Interannual variability across the Indo-Pacific regions becomes rather stronger than observed, leading to greater extremes of monsoon flood and drought. Increased strength, and improved timing of the monsoon-ENSO teleconnection give the flux corrected model better potential for seasonal prediction. A less confined warm pool allows the warmest SST and thus the rising branch of the Walker circulation during El Niño to be situated further east. Changes to the Pacific Ocean thermocline structure help increase ENSO variability, which feeds back to further strengthen the teleconnection.

Niño-3 SST variability is broadened at its peak periods, possibly related to increase in stochastic forcing at synoptic timescales seen in HadCM3FA. Power at biennial timescales also increases, related to increased coupling of the Asian summer monsoon to the Pacific.

In summary, systematic biases can influence the development of El Niño and consequently impact poorly on the teleconnections used for monsoon prediction. As suggested in a paper discussing this work (Turner *et al.*, 2005), limited flux adjustments could be used to constrain the basic state, while lending increased predictability to the monsoon season. Given that the coupled ocean-atmosphere system is far from linear, anomaly forecasts which are based on erroneous basic states, will themselves be inaccurate due to the systematic bias. These too could be improved by incorporating limited flux adjustments into the coupled system.

What is the effect of climate change on the monsoon system?

A coupled GCM integration was carried out under equilibrium doubled carbon dioxide conditions, to test the impact of climate change on the monsoon and its major influence, ENSO.

In common with other coupled model studies, a northward shift is seen in the low-level monsoon jet of the future climate, together with statistically significant increases in seasonal precipitation over the Indian region. This amounts to an increase in monsoon strength, despite the El Niño-like warming which has occured in the Pacific. The increased moisture convergence over the Indian region dominates over the large scale subsidence response expected with climatological El Niño-like behaviour.

In the east Pacific, interannual variability has increased preferentially during autumn and winter, increasing the phase locking of El Niño-La Niña to the annual cycle and relating to an increased propensity for El Niño to occur. ENSO is also stronger relative to the annual cycle, together with an increase in monsoon variability in the future climate. These effects in combination help strengthen the Pacific teleconnections, particularly when monsoon strength is measured by broad-scale dynamical or rainfall indices. There is greater correspondence between monsoon dynamics and precipitation in the $2 \times \mathrm{CO}_2$ climate in HadCM3, potentially easing the task of seasonal prediction.

In a further study of the monthly-mean precipitation response to underlying SST, the $2 \times \mathrm{CO}_2$ simulation is found to require a higher underlying threshold temperature before organized convection occurs. This counter-intuitive result suggests that GCMs do not respond in the expected (Clausius-Clapeyron) way to climate change, a point which requires further study.

Can we make an assessment of the impact of systematic errors on future monsoon climate?

The thesis proceeds by assuming that errors present in the basic state of control climate simulations will also exist in future climate simulations. Given the uncertainty in predicting systematic biases in the future scenario, we have opted to use the same flux correction to assess their impact.

The equatorial flux adjustments, being of the same magnitude as in Turner *et al.* (2005), influence the mean climate of HadCM3 $2 \times \mathrm{CO}_2$ in the same way as under $1 \times \mathrm{CO}_2$ conditions.

The response to climate change in the flux adjusted model (HadCM3FA) is more pronounced than in HadCM3. Most signals, such as El Niño-like warming of the Pacific, monsoon strength, and monsoon-ENSO variability are of the same sign as HadCM3 but greater in magnitude.

ENSO becomes even more strongly phase-locked to the annual cycle in HadCM3FA $2 \times \mathrm{CO}_2$, and stronger in relation to it. The monsoon-ENSO teleconnection is found to strengthen for the same reasons as at $1 \times \mathrm{CO}_2$ outlined in Turner *et al.* (2005). The teleconnection also features a strong biennial character, with significant positive correlations between summer monsoon rainfall and east Pacific SSTs in the previous year. This relates to a noticeable biennial character in the interannual variation of the monsoon and Niño-3 SSTs. El Niño in the HadCM3FA simulations at $2 \times \mathrm{CO}_2$ now particularly seems to favour eastward propagation.

The obvious biennial character to SSTs in the eastern equatorial Pacific of the flux corrected integration at $2 \times \mathrm{CO}_2$ led to further studies into the character of the simulated climate, presented in chapter 5. Characterizing the regimes as *irregular* and *biennial* has led to the discovery of several parallels and discrepancies with the observed system.

The biennial regime features a much smaller annual cycle, and a strongly phase-locked 2-year ENSO oscillation with a large amplitude when compared to ENSO events during the irregular period.

The two regimes can be characterized as theoretical modes, the first being a stable basic state wherein stochastic forcing excites ENSO on irregular timescales. The second mode features an unstable basic state with a self excited limit cycle, which would explain the regular, strongly phase-locked biennial regime. The transition between these two states is seen as an increase in air-sea coupling strength beyond a bifurcation point. This strengthening is noted also in the model integrations when either flux adjustments or increased CO_2 concentrations are applied to the model. Parallels can also be drawn between the two theoretical modes and SST and basin-wide modes which exist to varying degrees in observations.

The HadCM3FA $2 \times \mathrm{CO}_2$ integration features a tendency towards basin-wide, delayed-oscillator type modes (T-modes), with their inherent eastward propagation. This tendency is particularly clear during the biennial regime, together with maximum SSTs occuring further east. The tendency is likely related to increased atmosphere-ocean interaction, via a decrease in the strength of mean trade winds in the Pacific basin during the biennial period. Weakening of the trades is also seen as flux adjustments are implemented or greenhouse gas concentrations are increased. The biennial tendency however is in conflict with the push towards thermocline modes, which in nature typically have periods of 4–5 years.

Intraseasonal behaviour shows clear differences between the time periods. Stronger activity during the irregular period may relate to the stochastic forcing required to excite this mode in the Jin model, but more repressed behaviour in the biennial regime is inconsistent with strong activity during observed T-mode El Niños such as 1997.

The move to biennial oscillations is not just limited to the Pacific basin however, the Indian sector undergoing oscillations as part of the tropospheric biennial oscillation (TBO). The Indian Ocean dipole is thus found to have fundamental involvement, responding to anomalous Indian monsoon seasons.

The biennial tendency in the model (and to a lesser extent after flux adjustments or doubled $\mathrm{CO_2}$ are used individually) is found to relate to strong monsoon wind forcing over the west Pacific, and meridional confinement of the wind-stress response to warm or cold events. The wind-stress response is confined in part due to model deficiency and also the equatorial nature of applied flux corrections. The TBO behaviour aids the dramatic strengthening of the monsoon-ENSO teleconnection during the biennial regime, indicating much stronger coupling across the Indo-Pacific sectors.

The stronger teleconnection is in contrast with recent waning of the observed relation associated with the trend for T-mode El Niño. In all model integrations, interdecadal changes in the monsoon-ENSO teleconnection are observed. These changes are of similar magnitude to those seen in the observed record, despite constant $\mathrm{CO_2}$ forcing. This suggests there is much to understand about the importance of longer timescale oscillations in the coupled climate system.

6.2 Limitations

A number of limitations to the study in chapters 3–5 could be improved upon by incorporating model extensions or increasing the resolution.

Whilst projected increases in carbon dioxide have been considered in chapters 4–5, the absence of sulphate aerosol forcing may give an unduly large climate change result. Sulphate emissions, either natural (large volcanic eruptions) or industrial, are likely to counter some of the effects of climate change ($e.g.$, Ashrit *et al.*, 2003; Johns *et al.*, 2003). A more complete study would incorporate some physical parametrization of these effects, as is possible in the Unified Model.

Inclusion of vegetation or coupled carbon cycle model components into the land-ocean-atmosphere system would introduce feedbacks not considered in this study. Drying of large regions such as the Amazon basin is found to be increased in a positive feedback when a vegetation cycle is incorporated into HadCM3 by Betts *et al.* (2004), a study which sees the rainforest dying away. Cox *et al.* (2004) see an acceleration in climate change when a coupled carbon model stores less carbon in the land surface as the planet warms. It is clear then that some of the missing physical processes contribute opposing errors. Inclusion of a vegetation cycle over India would prove interesting in climate change scenarios, given the significant increases in surface temperature and precipitation over the subcontinent.

While the vertical resolution of the atmosphere has been addressed and led to some improvements (Inness *et al.*, 2001), the horizontal grid, especially in the ocean component, is rather coarse ($1.25° \times 1.25°$). This particularly limits the prospect for realistic simulation of El Niño modes involving basin-wide adjustment to ocean wave dynamics. Some studies, such as Lengaigne *et al.* (2002), have shown that the ocean can respond in a realistic way to observed wind stress forcing when meridional resolution near the equator is increased ($0.5°$ in the OPA model). Other studies ($e.g.$, Timmermann *et al.*, 1999, with the same resolution at the equator) have shown however that ENSO does not always behave well on finer grids.

6.3 Future work

There is much scope for further experimentation to explain some of the findings of this thesis in further detail. Consideration of $4 \times \mathrm{CO_2}$ forcing would further illustrate the potential for future climate change. The nonlinear nature of the coupled ocean-atmosphere system mean that changes of this magnitude on the monsoon-ENSO system would be much larger than $2 \times \mathrm{CO_2}$, note May (2004). In comparing $2 \times \mathrm{CO_2}$ and $4 \times \mathrm{CO_2}$ simulations, Meehl and Arblaster (2003) find a much greater response in seasonal monsoon precipitation. Transient climate change integrations (where the $\mathrm{CO_2}$ concentrations follow observed twentieth century changes or are ramped up at, $e.g.$, $1\%\ \mathrm{year}^{-1}$) would allow the monsoon-ENSO teleconnection to be studied in a different light. More consideration could then be given to the variation in its strength, as in studies such as Annamalai *et al.* (2005).

No mechanism has been suggested which forces the threshold for tropical convection to increase in climate change simulations. Greater availability of long observational datasets would allow the repsonses of precipitation to underlying SST forcing to be studied during different background states. Thus we could test if GCMs were simulating realistic behaviour in this sense.

The effect of ocean-atmosphere coupling on monsoon-ENSO system has not been explicitly considered in this thesis. Brief analysis of the atmosphere-only model HadAM3 have revealed a very poor teleconnection when forced with observed SSTs. This makes sense considering the presence of information exchange in only one direction, ocean to atmosphere, in the system.

Despite being the main external influence on the Asian summer monsoon system, ENSO is the only factor that has been studied in detail in this thesis. Further work could take more account of changes in the Indian Ocean, for example studying extreme monsoons which are found to be unrelated to El Niño-La Niña. Alternatively, those non-event years could also be studied for their response to Eurasian snow cover anomalies. This work may best be suited to integrations of several ensemble members.

Within the framework of the GCM integrations already carried out, further study could be made of the intraseasonal monsoon behaviour. A more detailed look at the onset date, or the prevalence of active and break periods in the existing models would be useful, particularly when considered in the context of climate change.

A more detailed look at the relationship between monsoon wind forcing on the west Pacific and meridional confinement of the zonal wind stress response to warm events, and the mechanism by which they alter ENSO period will be carried out.

References

Annamalai, H. and Liu, P. (2005). Response of the Asian summer monsoon to changes in El Niño properties. *Quarterly Journal of the Royal Meteorological Society*, **131**, 805–831.

Annamalai, H., Hamilton, K., and Sperber, K. R. (2005). South Asian Summer Monsoon and its Relationship with ENSO in the IPCC AR4 simulations. *Submitted to Journal of Climate*.

Ashrit, R., Douville, H., and Kumar, K. (2003). Response of the Indian Monsoon and ENSO-Monsoon Teleconnection to Enhanced Greenhouse Effect in the CNRM Coupled Model. *Journal of the Meteorological Society of Japan*, **81**, 779–803.

Ashrit, R. G., Kumar, K. R., and Krishna, K. K. (2001). ENSO-monsoon relationships in a greenhouse warming scenario. *Geophysical Research Letters*, **28**, 1727–1730.

Battisti, D. S. (1988). Dynamics and Thermodynamics of a Warming Event in a Coupled Tropical Atmosphere-Ocean Model. *Journal of the Atmospheric Sciences*, **45**, 2889–2919.

Battisti, D. S. and Hirst, A. C. (1989). Interannual Variability in a Tropical Atmosphere-Ocean Model: Influence of the Basic State, Ocean Geometry and Nonlinearity. *Journal of the Atmospheric Sciences*, **46**, 1687–1712.

Betts, R. A., Cox, P. M., Collins, M., Harris, P. P., Huntingford, C., and Jones, C. D. (2004). The role of ecosystem-atmosphere interactions in simulated Amazonian precipitation decrease and forest dieback under global climate warming. *Theoretical and Applied Climatology*, **78**, 157–175.

Bhalme, H. and Jadhav, S. (1984). The Southern Oscillation and its Relation to Monsoon Rainfall. *Journal of Climatology*, **4**, 509–520.

Bhaskaran, B., Mitchell, J. F. B., Lavery, J. R., and Lal, M. (1995). Climatic response of the Indian subcontinent to doubled CO_2 concentrations. *International Journal of Climatology*, **15**, 873–892.

Bjerknes, J. (1966). A possible response of the atmospheric Hadley circulation to equatorial anomalies of ocean temperature. *Tellus*, **XVIII**, 820–828.

Bjerknes, J. (1969). Atmospheric teleconnections from the equatorial Pacific. *Monthly Weather Review*, **97**(3), 163–172.

Bony, S., Lau, K.-M., and Sud, Y. C. (1997). Sea Surface Temperature and Large-Scale Circulation Influences on Tropical Greenhouse Effect and Cloud Radiative Forcing. *Journal of Climate*, **10**, 2055–2077.

Chang, C.-P. and Li, T. (2000). A Theory for the Tropical Tropospheric Biennial Oscillation. *Journal of the Atmospheric Sciences*, **57**, 2209–2224.

Charney, J. G. and Shukla, J. (1981). *Monsoon Dynamics: Predictability of Monsoons*. Cambridge University Press. Edited by Lighthill, J. and Pearce, R.

Codron, F., Vintileos, A., and Sadourny, R. (2001). Influence of Mean State Changes on the Structure of ENSO in a Tropical Coupled GCM. *Journal of Climate*, **14**, 730–742.

Collins, M. (2000a). The El Niño-Southern Oscillation in the Second Hadley Centre Coupled Model and its response to Greenhouse warming. *Journal of Climate*, **13**, 1299–1312.

Collins, M. (2000b). Understanding uncertainties in the response of ENSO to greenhouse warming. *Geophysical Research Letters*, **27**, 3509–3512.

Collins, M. and The CMIP Modelling Groups (2005). El Niño- or La Niña-like climate change? *Climate Dynamics*, **25**, 89–104.

Cox, P. M., Betts, R. A., Jones, C. D., Spall, S. A., and Totterdall, I. J. (2000). Acceleration of global warming due to carbon-cycle feedbacks in a coupled climate model. *Nature*, **408**, 184–187.

Cox, P. M., Betts, R. A., Collins, M., Harris, P. P., Huntingford, C., and Jones, C. D. (2004). Amazonian forest dieback under climate-carbon cycle projections for the 21st century. *Theoretical and Applied Climatology*, **78**, 137–156.

Douville, H., Royer, J.-F., Polcher, J., Cox, P., Gedney, N., Stephenson, D. B., and Valdes, P. J. (2000). Impact of $\mathrm{CO_2}$ doubling on the Asian summer monsoon: robust versus model-dependent responses. *Journal of the Meteorological Society of Japan*, **78**, 421–439.

Federov, A. V. and Philander, S. G. (2000). Is El Niño changing? *Science*, **288**, 1997–2002.

Federov, A. V. and Philander, S. G. (2001). A Stability Analysis of Tropical Ocean-Atmosphere Interactions: Bridging Measurements and Theory for El Niño. *Journal of Climate*, **14**, 3086–3101.

Gadgil, S. and Sajani, S. (1998). Monsoon precipitation in the AMIP runs. *Climate Dynamics*, **14**, 659–689.

Gill, A. E. (1980). Some simple solutions for heat-induced tropical circulation. *Quarterly Journal of the Royal Meteorological Society*, **106**, 447–462.

Gordon, C., Cooper, C., Senior, C. A., Banks, H., Gregory, J. M., Johns, T. C., Mitchell, J. F. B., and Wood, R. A. (2000). The simulation of SST, sea ice extents and ocean heat transports in a version of the Hadley Centre coupled model without flux adjustments. *Climate Dynamics*, **16**, 147–168.

Guilyardi, E. (2006). El Niño- mean state - seasonal cycle interactions in a multi-model ensemble. *Climate Dynamics*, **26**, 329–348.

Guilyardi, E., Gualdi, S., Slingo, J., Navarra, A., Delecluse, P., Cole, J., Madec, G., Roberts, M., Latif, M., and Terray, L. (2004). Representing El Niño in Coupled Ocean-Atmosphere GCMs: The Dominant Role of the Atmospheric Component. *Journal of Climate*, **17**, 4623–4629.

Hu, Z.-Z., Latif, M., Roeckner, E., and Bengtsson, L. (2000). Intensified Asian summer monsoon and its variability in a coupled model forced by increasing greenhouse gas concentrations. *Geophysical Research Letters*, **27**, 2618–2684.

Inness, P., Slingo, J., Woolnough, S., Neale, R., and Pope, V. (2001). Organization of tropical convection in a GCM with varying vertical resolution: implications for the simulation of the Madden-Julian Oscillation. *Climate Dynamics*, **17**, 777–793.

Inness, P., Slingo, J., Guilyardi, E., and Cole, J. (2003). Simulation of the Madden-Julian Oscillation in a Coupled General Circulation Model. Part II: The Role of the Basic State. *Journal of Climate*, **16**, 365–382.

Intergovernmental Panel on Climate Change (2001). *Climate Change 2001: The Scientific Basis. Contribution of Working Group I to the Third Assessment Report*. Cambridge University Press, UK. (Eds. J. T. Houghton, Y. Ding, D. J. Griggs, M. Noguer, P. J. van der Linden, X. Dai, K. Maskell and C. A. Johnson).

Jin, F.-F. (1997). An equatorial ocean recharge paradigm for ENSO. Part I: conceptual model. *Journal of the Atmospheric Sciences*, **54**, 811–829.

Johns, T. C., Carnell, R. E., Crossley, J. F., Gregory, J. M., Mitchell, J. F. B., Senior, C. A., Tett, S. F. B., and Wood, R. A. (1997). The second Hadley Centre coupled ocean-atmosphere GCM: model description, spinup and validation. *Climate Dynamics*, **13**, 103–134.

Johns, T. C., Gregory, J. M., Ingram, W. J., Johnson, C. E., Jones, A., Lowe, J. A., Mitchell, J. F. B., Roberts, D. L., Sexton, D. M. H., Stevenson, D. S., Tett, S. F. B., and Woodage, M. J. (2003). Anthropogenic climate change for 1860 to 2100 simulated with the HadCM3 model under updated emissions scenarios. *Climate Dynamics*, **20**, 583–612.

Ju, J. and Slingo, J. M. (1995). The Asian Summer Monsoon and ENSO. *Quarterly Journal of the Royal Meteorological Society*, **121**, 1133–1168.

Kållberg, P., Berrisford, P., Hoskins, B., Simmons, A., Uppala, S., Lamy-Thépaut, S., and Hine, R. (2005). *19: ERA-40 Atlas*. ECMWF Re-Analysis Project Report Series.

Kim, K.-M. and Lau, K.-M. (2001). Dynamics of monsoon-induced biennial variability in ENSO. *Geophysical Research Letters*, **28**, 315–318.

Kirtman, B. P. (1997). Oceanic Rossby Wave Dynamics and the ENSO Period in a Coupled Model. *Journal of Climate*, **10**, 1690–1704.

Kitoh, A., Yukimoto, S., Noda, A., and Motoi, T. (1997). Simulated Changes in the Asian Summer Monsoon at Times of Increased Atmospheric CO_2. *Journal of the Meteorological Society of Japan*, **75**, 1019–1031.

Krishna Kumar, K., Soman, M. K., and Rupa Kumar, K. (1995). Seasonal forecasting of Indian summer monsoon rainfall: A review. *Weather*, **50**, 449–467.

Krishna Kumar, K., Rajagopalan, B., and Cane, M. (1999). On the Weakening Relationship Between the Indian Monsoon and ENSO. *Science*, **284**, 2156–2159.

Krishnamurthy, V. and Goswami, B. (2000). Indian Monsoon-ENSO Relationship on Interdecadal Timescale. *Journal of Climate*, **13**, 579–595.

Krishnamurthy, V. and Shukla, J. (2000). Intraseasonal and Interannual Variability of Rainfall over India. *Journal of Climate*, **13**, 4366–4377.

Latif, M., Sperber, K., Arblaster, J., Braconnot, P., Chen, D., Colman, A., Cubasch, U., Cooper, C., Delecluse, P., DeWitt, D., Fairhead, L., Flato, G., Hogan, T., Ji, M., Kimoto, M., Kitoh, A., Knutson, T., Le Treut, H., Li, T., Manabe, S., Marti, O., Mechoso, C., Meehl, G., Power, S., Roeckner, E., Sirven, J., Terray, L., Vintzileos, A., Voss, R., Wang, B., Washington, W., Yoshikawa, I., Yu, J., and Zebiak, S. (2001).

ENSIP: the El Niño simulation intercomparison project. *Climate Dynamics*, **18**, 255–276.

Lau, K.-M. and Wu, H. T. (2001). Principal Modes of Rainfall-SST Variability of the Asian Summer Monsoon: A reassessment of the Monsoon-ENSO Relationship. *Journal of Climate*, **14**, 2880–2895.

Lengaigne, M., Boulanger, J.-P., Menkes, C., Masson, S., Madec, G., and Delecluse, P. (2002). Ocean response to the March 1997 Westerly Wind Event. *Journal of Geophysical Research*, **107(C12)**.

Lengaigne, M., Guilyardi, E., Boulanger, J.-P., Menkes, C., Delecluse, P., Inness, P., Cole, J., and Slingo, J. M. (2004). Triggering of El Niño by westerly wind events in a coupled general circulation model. *Climate Dynamics*, **23**, 601–620.

Levitus, S. and Boyer, T. P. (1994). *World Ocean Atlas 1994, Volume 4: Temperature*. US Department of Commerse, Washington, DC.

Li, C. and Yanai, M. (1996). The Onset and Interannual Variability of the Asian Summer Monsoon in Relation to Land-Sea Thermal Contrast. *Journal of Climate*, **9**, 358–375.

Li, T. (1997). Phase transition of the El Niño-Southern Oscillation: a stationary SST mode. *Journal of the Atmospheric Sciences*, **54**, 2872–2887.

Li, T., Tham, C.-W., and Chang, C.-P. (2001). A Coupled Air-Sea-Monsoon Oscillator for the Tropospheric Biennial Oscillation. *Journal of Climate*, **14**, 752–764.

Loschnigg, J., Meehl, G. A., Webster, P. J. Arblaster, J., and Compo, G. P. (2003). The Asian Monsoon, the Tropospheric Biennial Oscillation, and the Indian Ocean Zonal Mode in the NCAR CSM. *Journal of Climate*, **16**, 1617–1642.

Marshall, J. and Molteni, F. (1993). Toward a dynamical understanding of planetary-scale flow regimes. *Journal of the Atmospheric Sciences*, **50**, 1792–1818.

May, W. (2002). Simulated changes of the Indian summer monsoon under enhanced greenhouse gas conditions in a global time-slice experiment. *Geophysical Research Letters*, **29**, 1118–1121.

May, W. (2004). Potential future changes in the Indian summer monsoon due to greenhouse warming: analysis of mechanisms in a global time-slice experiment. *Climate Dynamics*, **22**, 389–414.

McPhaden, M. J. and Yu, X. (1999). Equatorial waves and the 1997-98 El Niño. *Geophysical Research Letters*, **26**, 2961–2964.

Meehl, G. A. (1987). The Annual Cycle and Interannual Variability in the Tropical Pacific and Indian Ocean Regions. *Monthly Weather Review*, **115**, 27–50.

Meehl, G. A. (1993). A Coupled Air-Sea Biennial Mechanism in the Tropical Indian and Pacific Regions: Role of the Ocean. *Journal of Climate*, **6**, 31–41.

Meehl, G. A. (1994). Coupled Land-Ocean Atmosphere Processes and South Asian Monsoon Variability. *Science*, **266**, 263–267.

Meehl, G. A. (1997). The South Asian Monsoon and the Tropospheric Biennial Oscillation. *Journal of Climate*, **10**, 1921–1943.

Meehl, G. A. and Arblaster, J. M. (2001). The Tropospheric Biennial Oscillation and Indian Monsoon Rainfall. *Geophysical Research Letters*, **28**, 1731–1734.

Meehl, G. A. and Arblaster, J. M. (2002a). Indian Monsoon GCM Sensitivity Experiments Testing Tropospheric Biennial Oscillation Transition Conditions. *Journal of Climate*, **15**, 923–944.

Meehl, G. A. and Arblaster, J. M. (2002b). The Tropospheric Biennial Oscillation and Asian-Australian Monsoon Rainfall. *Journal of Climate*, **15**, 722–744.

Meehl, G. A. and Arblaster, J. M. (2003). Mechanisms for projected future changes in south Asian monsoon precipitation. *Climate Dynamics*, **21**, 659–675.

Meehl, G. A. and Washington, W. M. (1996). El Niño-like climate change in a model with increased atmospheric $\mathrm{CO_2}$ concentrations. *Nature*, **382**, 56–60.

Meehl, G. A., Collins, W. D., Boville, B. A., Kiehl, J. T., Wigley, T. M. L., and Arblaster, J. M. (2000). Response of the NCAR climate system model to increased $\mathrm{CO_2}$ and the role of physical processes. *Journal of Climate*, **13**, 1879–1898.

Meehl, G. A., Gent, P. R., Arblaster, J., Otto-Bliesner, B. L., Brady, E. C., and Craig, A. (2001). Factors that effect the amplitude of El Niño in global coupled climate models. *Climate Dynamics*, **17**, 515–526.

Meehl, G. A., Arblaster, J., and Loschnigg, J. (2003). Coupled Ocean-Atmosphere Dynamical Processes in the Tropical Indian and Pacific Oceans and the TBO. *Journal of Climate*, **16**, 2138–2158.

Monsoon On-Line (2005). `http://www.tropmet.res.in/~kolli/MOL`.

Mooley, D. A. and Parthasarathy, B. (1984). Fluctuations in All-India summer monsoon rainfall during 1871-1978. *Climatic Change*, **6**, 287–301.

Neale, R. and Slingo, J. (2003). The Maritime Continent and its role in the global climate: a GCM study. *Journal of Climate*, **16**, 834–848.

Neelin, J. D., Battisti, D. S., Hirst, A. C., Jin, F.-F., Wakata, Y., Yamagata, T., and Zebiak, S. E. (1998). ENSO theory. *Journal of Geophysical Research*, **103**, 14261–14290.

Normand, C. (1953). Monsoon seasonal forecasting. *Quarterly Journal of the Royal Meteorological Society*, **79**, 463–473.

Palmer, T. N. (1994). Chaos and Predictability in forecasting the Monsoons. *Proc. Indian natn. Sci. Acad.*, **60**, 57–66.

Parker, D. E., Folland, C. K., and Jackson, M. (1995). Marine surface temperature: Observed variations and data requirements. *Climatic Change*, **31**, 559–600.

Parthasarathy, B., Munot, A. A., and Kothawale, D. R. (1994). All-India Monthly and Seasonal Rainfall Series: 1871–1993. *Theoretical and Applied Climatology*, **49**, 217–224.

Pope, V. D., Gallani, M. L., Rowntree, P. R., and Stratton, R. A. (2000). The impact of new physical parametrizations in the Hadley Centre climate model: HadAM3. *Climate Dynamics*, **16**, 123–146.

Rajeevan, M., Pai, D. S., Dikshit, S. K., and Kelkar, R. R. (2004). Imd's new operational models for long-range forecast of southwest monsoon rainfall over india and their verification for 2003. *Current Science*, **86**, 422–431.

Rajendran, K., Kitoh, A., and Yukimoto, S. (2004). South and East Asian summer Monsoon Climate and Variation in the MRI Coupled Model (MRI-CGCM2). *Journal of Climate*, **17**, 763–782.

Rasmusson, E. M., Wang, X., and Ropelewski, C. F. (1990). The biennial component of ENSO variability. *Journal of Marine Systems*, **1**, 71–96.

Rayner, N. A., Parker, D. E., Horton, E. B., Folland, C. K., Alexander, L. V., Rowell, D. P., Kent, E. C., and Kaplan, A. (2003). Global analyses of sea surface temperature, sea ice, and night marine air temperature since the late nineteenth century. *Journal of Geophysical Research*, **108**, 4407.

Rodwell, M. J. and Hoskins, B. J. (1995). A Model of the Asian Summer Monsoon. Part II: Cross-Equatorial Flow and PV Behavior. *Journal of the Atmospheric Sciences*, **52**, 1341–1356.

Saji, N. H., Goswami, B. N., Vinayachandran, P. N., and Yamagata, T. (1999). A dipole mode in the tropical Indian Ocean. *Nature*, **401**, 360–363.

Schen, S. and Lau, K.-M. (1995). Biennial Oscillation Associated with the East Asian Summer Monsoon and Tropical Sea Surface Temperatures. *Journal of the Meteorological Society of Japan*, **73**, 105–124.

Schneider, E. K., Huang, B., and Shukla, J. (1994). Ocean wave dynamics and El Niño. Technical Report 1, Center for Ocean-Land-Atmosphere Studies.

Shukla, J. and Paolino, D. (1983). The Southern Oscillation and Long-Range Forecasting of the Summer Monsoon Rainfall over India. *Monthly Weather Review*, **111**, 1830–1837.

Slingo, J. and Annamalai, H. (2000). 1997: The El Niño of the Century and the Response of the Indian Summer Monsoon. *Monthly Weather Review*, **128**, 1778–1797.

Slingo, J., Sperber, K., Boyle, J. S., Ceron, J.-P., Dix, M., Dugas, B., Ebisuzaki, W., Fyfe, J., Gregory, D., Gueremy, J.-F., Hack, J., Harzallah, A., Inness, . P., Kitoh, A., Lau, W.-M., McAvaney, B., Madden, R., Matthews, A., Palemer, T., Park, C.-K., Randall, D., and Renno, N. (1996). Intraseasonal oscillations in 15 atmospheric general circulation models: results from an AMIP diagnostic subproject. *Climate Dynamics*, **12**, 325–357.

Slingo, J., Rowell, D. P., Sperber, K., and Nortley, F. (1999). On the predictability of the interannual behaviour of the Madden-Julian Oscillation and its relationship with El Niño. *Quarterly Journal of the Royal Meteorological Society*, **125**, 583–609.

Spencer, H. (2002). *The predictability of ENSO teleconnections*. Ph.D. thesis, University of Reading, UK.

Spencer, H. and Slingo, J. M. (2003). The simulation of peak and delayed ENSO teleconnections. *Journal of Climate*, **16**, 1757–1774.

Spencer, H., Sutton, R., Slingo, J. M., Roberts, M., and Black, E. (2005). Indian Ocean Climate and Dipole Variability in Hadley Centre Coupled GCMs. *Journal of Climate*, **18**, 2286–2307.

Sperber, K. R. and Palmer, T. N. (1996). Interannual tropical Rainfall Variability in General Circulation Model Simulations Associated with the Atmospheric Model Intercomparison Project. *Journal of Climate*, **9**, 2727–2750.

Sperber, K. R., Slingo, J. M., and Annamalai, H. (2000). Predictability and the relationship between subseasonal and interannual variability during the asian summer monsoon. *Quarterly Journal of the Royal Meteorological Society*, **126**, 2545–2574.

Suarez, M. J. and Schopf, P. S. (1988). A Delayed Action Oscillator for ENSO. *Journal of the Atmospheric Sciences*, **45**, 3283–3287.

Timmermann, A. (2001). Changes of ENSO stability due to greenhouse warming. *Geophysical Research Letters*, **28**, 2061–2064.

Timmermann, A., Oberhuber, J., Bacher, A., Esch, M., Latif, M., and Roeckner, E. (1999). Increased El Niño frequency in a climate model forced by future greenhouse warming. *Nature*, **398**, 694–697.

Timmermann, A., Jin, F.-F., and Collins, M. (2004). Intensification of the annual cycle in the tropical pacific due to greenhouse warming. *Geophysical Research Letters*, **31**, 2727–2750.

Torrence, C. and Compo, G. P. (1999). A Practical Guide to Wavelet Analysis. *Bulletin of the American Meteorological Society*, **79**, 61–78.

Torrence, C. and Webster, P. J. (1999). Interdecadal Changes in the ENSO-Monsoon System. *Journal of Climate*, **12**, 2679–2690.

Trenberth, K. E. and Stepaniak, D. P. (2001). Indices of El Niño evolution. *Journal of Climate*, **14**, 1697–1701.

Turner, A. G., Inness, P. M., and Slingo, J. M. (2005). The role of the basic state in the ENSO-monsoon relationship and implications for predictability. *Q. J . R. Meteorol. Soc.*, **131**, 781–804.

Uppala, S., Kallberg, P., Simmons, A., Andrae, U., da Costa Bechtold, V., Fiorino, M., Gibson, J., Haseler, J., Hernandez, A., Kelly, G., Li, X., Onogi, K., Saarinen, S., Sokka, N., Allan, R., Andersson, E., Arpe, K., Balmaseda, M., Beljaars, A., van de Berg, L., Bidlot, J., Bormann, N., Caires, S., Chevallier, F., Dethof, A., Dragosavac, M., Fisher, M., Fuentes, M., Hagemann, S., Holm, E., Hoskins, B., Isaksen, L., Janssen, P., Jenne, R., McNally, A., Mahfouf, J.-F., Morcrette, J.-J., Rayner, N., Saunders, R., Simon, P., Sterl, A., Trenberth, K., Untch, A., Vasiljevic, D., Viterbo, P., and Woollen, J. (2005). The ERA-40 re-analysis. *Quarterly Journal of the Royal Meteorological Society*, **131**, 2961–3012.

Wang, B. and Fan, Z. (1999). Choice of South Asian Summer Monsoon Indices. *Bulletin of the American Meteorological Society*, **80**, 629–638.

Wang, B., Barcilon, A., and Fang, Z. (1999). Stochastic Dynamics of El Niño-Southern Oscillation. *Journal of the Atmospheric Sciences*, **56**, 5–23.

Webster, P. J. and Yang, S. (1992). Monsoon and ENSO: Selectively interactive systems. *Quarterly Journal of the Royal Meteorological Society*, **118**, 877–926.

Webster, P. J., Magana, V. O., Palmer, T. M., Shukla, J., Tomas, R. A., Yanai, M., and Yasunari, T. (1998). Monsoons: Processes, predictability, and prospects for predcition. *Journal of Geophysical Research*, **103**, 14451–14510.

Wu, R. and Kirtman, B. P. (2003). On the impacts of the Indian summer monsoon on ENSO in a coupled GCM. *Quarterly Journal of the Royal Meteorological Society*, **129**, 3439–3468.

Wu, R. and Kirtman, B. P. (2004). The Tropospheric Biennial Oscillation of the Monsoon-ENSO System in an Interactive Ensemble Coupled GCM. *Journal of Climate*, **17**, 1623–1640.

Wu, R. and Wang, B. (2002). A contrast of the East Asian summer monsoon-ENSO relationship between 1962–77 and 1978–1993. *Journal of Climate*, **15**, 3266–3278.

Xie, P. and Arkin, P. A. (1997). Global Precipitation: A 17-Year Monthly Analysis Based on Gauge Observations, Satellite Estimates, and Numerical Model Outputs. *Bulletin of the American Meteorological Society*, **78**, 2539–2559.

Yasunari, T. (1990). Impact of Indian Monsoon on the Coupled Atmosphere/Ocean System in the Tropical Pacific. *Meteorology and Atmospheric Physics*, **44**, 29–41.

Yasunari, T. (1991). The Monsoon Year- A New Concept of the Climatic Year in the Tropics. *Bulletin of the American Meteorological Society*, **72**, 1331–1338.

Zebiak, S. E. and Cane, M. A. (1987). A Model El Niño-Southern Oscillation. *Monthly Weather Review*, **115**, 2262–2278.

Zelle, H., Van Oldenborgh, G. J., and Dijkstra, H. (2005). El Niño and Greenhouse Warming: Results from Ensemble Simulations with the NCAR CCSM. *Journal of Climate*, **18**, 4669–4683.